

TEHNIČKI GLASNIK

TEHNIČKI GLASNIK / TECHNICAL JOURNAL – GODIŠTE / VOLUME 12 – BROJ / NUMBER 3

RUJAN 2018 / SEPTEMBER 2018 – STRANICA / PAGES 124-195



SVEUČILIŠTE SJEVER / UNIVERSITY NORTH – CROATIA – EUROPE

ISSN 1846-6168 (PRINT) / ISSN 1848-5588 (ONLINE)

TECHNICAL JOURNAL

TEHNIČKI GLASNIK - TECHNICAL JOURNAL

Scientific-professional journal of University North

Volume 12

Varaždin, September 2018

Number 3

Pages 124–195

Editorial Office:

Sveučilište Sjever – Tehnički glasnik
Sveučilišni centar Varaždin
104. brigade 3, 42000 Varaždin, Hrvatska
Tel. ++385 42 493 328, Fax. ++385 42 493 333
E-mail: tehnickiglasnik@unin.hr
<https://tehnickiglasnik.unin.hr>
<https://www.unin.hr/djelatnost/izdavastvo/tehnicki-glasnik/>
<https://hrcak.srce.hr/tehnickiglasnik>

Founder and Publisher:

Sveučilište Sjever / University North

Council of Journal:

Marin MILKOVIĆ, Chairman; Anica HUNJET, Member; Goran KOZINA, Member; Mario TOMIŠA, Member;
Vlado TROPŠA, Member; Damir VUSIĆ, Member; Milan KLJAJIN, Member; Anatolii KOVROV, Member

Editorial Board:

Chairman Damir VUSIĆ (1), Milan KLJAJIN (2)/(1), Marin MILKOVIĆ (1), Krešimir BUNTAK (1), Anica HUNJET (1), Živko KONDIĆ (1), Goran KOZINA (1), Ljudevit KRPAN (1), Marko STOJIĆ (1), Božo SOLDIĆ (1), Mario TOMIŠA (1), Vlado TROPŠA (1), Vinko VIŠNJIĆ (1), Duško PAVLETIĆ (5), Branimir PAVKOVIĆ (5), Mile MATIJEVIĆ (3), Damir MODRIĆ (3), Nikola MRVAC (3), Klaudio PAP (3), Ivana ŽILJAK STANIMIROVIĆ (3), Krešimir GRILEC (6), Biserka RUNJE (6), Predrag ČOSIĆ (6), Sara HAVRLIŠAN (2), Dražan KOZAK (2), Roberto LUJIĆ (2), Leon MAGLIĆ (2), Ivan SAMARDŽIĆ (2), Antun STOIĆ (2), Katica ŠIMUNOVIĆ (2), Goran ŠIMUNOVIĆ (2), Ladislav LAZIĆ (7), Ante ČIKIĆ (8)/(1)/(2), Darko DUKIĆ (9), Gordana DUKIĆ (10), Srdan MEDIĆ (11), Sanja KALAMBURA (12), Marko DUNĐER (13), Zlata DOLAČEK-ALDUK (4), Dina STOBBER (4)

International Editorial Council:

Boris TOVORNIK (14), Milan KUHTA (15), Nenad INJAC (16), Džafer KUDUMOVIĆ (17), Marin PETROVIĆ (18), Salim IBRAHIMEFENDIĆ (19), Zoran LOVREKOVIĆ (20), Igor BUDAK (21), Darko BAJIĆ (22), Tomáš HANÁK (23), Nikolaj SURIANINOV (24), Evgenij KLIMENKO (24), Oleg POPOV (24), Ivo ČOLAK (25), Katarina MONKOVA (26)

Editor-in-Chief:

Milan KLJAJIN

Technical Editor:

Goran KOZINA

Graphics Editor:

Snježana IVANČIĆ VALENKO, Anja ZORKO

Linguistic Advisers for English language:

Ivana GRABAR, Iva GRUBJEŠIĆ

IT support:

Tomislav HORVAT

Print:

Centar za digitalno nakladništvo, Sveučilište Sjever

All manuscripts published in journal have been reviewed.**Manuscripts are not returned.****The journal is free of charge and four issues per year are published.****Circulation:** 100 copies**Journal is indexed and abstracted in:**

Web of Science Core Collection (Emerging Sources Citation Index - ESCI), EBSCOhost Academic Search Complete, EBSCOhost – One Belt, One Road Reference Source Product, ERIH PLUS, CITEFACTOR – Academic Scientific Journals, Hrcak - Portal znanstvenih časopisa RH

Registration of journal:

The journal "Tehnički glasnik" is listed in the HGK Register on the issuance and distribution of printed editions on the 18th October 2007 under number 825.

Preparation ended:

September 2018

Legend:

(1) University Nord, (2) Mechanical Engineering Faculty in Slavonski Brod, (3) Faculty of Graphic Arts Zagreb, (4) Faculty of Civil Engineering Osijek, (5) Faculty of Engineering Rijeka, (6) Faculty of Mechanical Engineering and Naval Architecture Zagreb, (7) Faculty of Metallurgy Sisak, (8) Bjelovar University of Applied Sciences, (9) Department of Physics of the University of Josip Juraj Strossmayer in Osijek, (10) Faculty of Humanities and Social Sciences Osijek, (11) Karlovac University of Applied Sciences, (12) University of Applied Sciences Velika Gorica, (13) Department of Polytechnics - Faculty of Humanities and Social Sciences Rijeka, (14) Faculty of Electrical Engineering and Computer Science - University of Maribor, (15) Faculty of Civil Engineering - University of Maribor, (16) University College of Teacher Education of Christian Churches Vienna/Krems, (17) Mechanical Engineering Faculty Tuzla, (18) Mechanical Engineering Faculty Sarajevo, (19) University of Travnik - Faculty of Technical Studies, (20) Higher Education Technical School of Professional Studies in Novi Sad, (21) University of Novi Sad - Faculty of Technical Sciences, (22) Faculty of Mechanical Engineering - University of Montenegro, (23) Brno University of Technology, (24) Odessa State Academy of Civil Engineering and Architecture, (25) Faculty of Civil Engineering - University of Mostar, (26) Faculty of Manufacturing Technologies with the seat in Prešov - Technical University in Košice

CONTENT	I
NOTE FROM THE NEW MEMBER OF INTERNATIONAL EDITORIAL COUNCIL	II
Erol CAN THE MODELING AND ANALYSIS OF A POWER TRANSMISSION LINE SUPPLIED BY A SOLAR POWER PLANT	124
Paolo BLECICH, Tomislav SENČIĆ, Igor WOLF, Igor BONEFAČIĆ NUMERICAL INVESTIGATION OF HEAT AND MASS TRANSFER INSIDE A WET COOLING TOWER	131
Mehmet ÖKSÜZ, Mehmet Burak ÖNAL, Recep HALICIOĞLU, Lale Canan DÜLGER ALTERNATIVE CONTROLLER DESIGN FOR ROTARY INVERTED PENDULUM	139
Saim KURAL, Safiye İPEK AYVAZ THE EFFECT OF BIOMATERIAL SELECTION ON THE STATIC STRENGTH OF FEMUR PROSTHESIS	146
Ivan ŠUMIGA, Dunja SRPAK, Živko KONDIĆ APPLICATION OF THERMOELECTRIC MODULES AS RENEWABLE ENERGY SOURCES	151
Krunoslav HAJDEK, Petra BRADIĆ, Martina HAJDEK, Mile MATIJEVIĆ COLOR PERCEPTION OF THE OBSERVER WITH THE MANIFESTATION OF THE CHROMATIC EFFECT OF CRISPENING	159
Robert ŽUPAN, Katarina ŽUPAN, Stanislav FRANGEŠ, Adam VINKOVIĆ AUTOMATIC PROCEDURAL 3D MODELLING OF BUILDINGS	166
Vedran MRZLJAK LOW POWER STEAM TURBINE ENERGY EFFICIENCY AND LOSSES DURING THE DEVELOPED POWER VARIATION	174
M. Erkan KÜTÜK, Murat ARTAN, L. Canan DÜLGER HYBRID SEVEN-BAR PRESS MECHANISM: LINK OPTIMIZATION AND KINETOSTATIC ANALYSIS	181
Davor PETROVIĆ, Mladen JURISIĆ, Vjekoslav TADIĆ, Ivan PLAŠČAK, Željko BARAČ DIFFERENT SENSOR SYSTEMS FOR THE APPLICATION OF VARIABLE RATE TECHNOLOGY IN PERMANENT CROPS	188
INSTRUCTIONS FOR AUTHORS	IV



Note from the new member of International Editorial Council

Dear readers,

I am delighted and it is an honour for me to write a few words of introduction to this issue; therefore, I would like to thank Editor-in-Chief for this opportunity.

We live in a digital age. Computers, smartphones and other digital devices play a great role not only in our social life but also in professional life. Many devices are controlled by computers and plenty of information is stored in the computer memory. We talk about Metadata, the Internet of Things or Industry 4.0. Nevertheless, it is necessary to consider that digital devices are only tools helping us to perform the work in a simpler and faster way or to do it with less energy. However, if we want to develop new technologies or to make things more sophisticated, it is necessary to understand the essence of the matter, similarly as it was in the past when people did not know computers or calculators. The motivation on how to do things better could be expressed by the words of Albert Einstein, "Look deep into nature, and then you will understand everything better."

Already in ancient times, people drew their ideas from nature. It is almost unbelievable for us how early men were able to build pyramids, Stonehenge, temples, roads, and other amazing things. How were they able to do it? The answer is simple. They were able to do it because they understood the nature of the issue and nature was an inspiration to them. They left a message for us in this way. We can see that this message is being received because during the recent decades, scientists have been trying to find their inspiration in nature again.

Researchers around the world are increasingly looking into nature to solve all sorts of problems. Inspired by it, they have developed the concocting stickier glues, stronger materials, zippier propellers, or colours. People often use dyes or pigments to colour foods, fabrics, and lots of other materials. But many of these colouring agents are toxic, their usage can be messy and dangerous. How we can improve it? Nature has an answer for this. The brilliant blue of certain

butterfly wings, for example, does not come from chemical pigments. Instead, the colour comes from the way light is reflected by scales that cover the butterfly's wings. Such reflections also produce the iridescent colours of a peacock's feathers or the bright blue of a bluebird's plumage. Scientists recently announced, in the Proceedings of the National Academy of Sciences, that the beautiful iridescent colours in butterfly wings are caused by so-called gyroids made of chitin and air. The gyroid has been studied by Alan Schoen, a U. S. National Aeronautics and Space Administration scientist; in 1970, he discovered that it was a super-strong, super-light, triply periodic structure. Triple periodic means that a small piece of the surface may be used to assemble the entire surface by taking a fundamental piece and translating copies in three independent directions in space.

In order to improve the mechanical properties of some materials or to develop a new material, scientists studied the spider network, which seems to be an insignificant thing at a first glance. When we look at a delicate spider web, we might not instantly think of a strength and durability, but in fact, spider silk is one of the toughest natural fibres known to man; it is stronger than steel, yet highly flexible. Its potential is endless, with possible applications in the medical industry, apparel, and even in a defence sphere. Scientists are studying how to turn spider silk into bulletproof vests for soldiers. Spider webs elongate and flex when bugs fly into them in the same way as a bulletproof vest absorbs the energy of a bullet.

Marine scientists have suspected for a long time that humpback whales' incredible agility comes from the bumps on the leading edges of their flippers. The advantage of the humpback-whale flipper seems to be the angle of attack. It is the angle between the flow of water and the face of the flipper. When the angle of attack of a whale flipper – or an airplane wing – becomes too steep, the result is something called stall. In aviation, stall means that there is no enough air flowing over the top surface of the wing. This causes a combination of increased drag and lost lift, a potentially dangerous situation that can result in a sudden loss of

altitude. Now, the Harvard University researchers have come up with a mathematical model that helps explain this hydrodynamic edge. They showed that the bumps on the humpback flipper, known as tubercles, change the distribution of pressure on the flipper so that some parts of it stall before others. Since different parts of the flipper stall at different angles of attack, abrupt stalling is easier to avoid. The work gives theoretical weight to a growing body of empirical evidence that similar bumps could lead to more-stable airplane designs, submarines with greater agility, and turbine blades that can capture more energy from the wind and water.

Nature teaches us a variety of lessons through its various forms. Everyone can look upon one form or the other and discover its various teachings. Another of such examples could also be found with nocturnal animals. It is clear for everybody that nocturnal animals have evolved differently from their day relatives. They are often equipped with accurate hearing, smell, and sight so they can find food in the dark and protect themselves from predators. Swiss researchers are studying the eyes of moths to understand how their structure could be applied to solar technology. The microstructure of the moth's eyes is adapted to collect as much light as possible, which is an ideal quality for solar panels. In order to create the artificial moth eyes, the team is using metal oxide microspheres.

Plenty of examples how to do things better can be found in nature. It is a role of scientists to investigate them and a role of engineers to transfer the knowledge into the real-life usage. As Mr. Yuan-Cheng Fung has already said, "Engineering is quite different from science. Scientists try to understand nature. Engineers try to make things that do not exist in nature."



Full Prof., Eng. MSc. Katarina MONKOVÁ, PhD.
Faculty of Manufacturing Technologies with the seat in
Prešov - Technical University in Košice
Sturova 31, 080 01 Prešov, Slovakia

THE MODELING AND ANALYSIS OF A POWER TRANSMISSION LINE SUPPLIED BY A SOLAR POWER PLANT

Erol CAN

Abstract: This article deals with the energy transmission line system which feeds from solar energy at the MATLAB Simulink. So, direct voltage is considered to be converted as an alternating voltage by a 35-level inverter after the solar power plant which has the power of 110 MW and produce 360 kV of direct voltage. A line which covers 240 km of distance is preferred to transmit electrical power from the A1 point to an A2 point. Due to this, the required mathematical equations are calculated with a circuit analyzing method for the line modeling in the simulation. Experiments on the model are carried out at the MATLAB Simulink after the creation of an energy transmission line. After that, when measurements are made taking into consideration the A2 node; the capacitor voltage, the transformer current, the A2 node current, and the fault current, values are given according to the converted voltage at the frequencies of 100 Hz, 80 Hz, and 50 Hz. The obtained results demonstrate the success of the proposed line system, while power is distributed with eliminated fault at a long distance at different frequencies.

Keywords: mathematical model of the line; simulation model of the transmission line; 35-level inverter

1 INTRODUCTION

Solar power is widely considered and used in many studies [1, 2]. However, solar energy usually needs long-line transmission because most solar centers are far away from the users, i.e. consumers. The processes of series compensation are considered at long distance transmission for improving the situation of the power line [3-5]. In this research, the energy power line to be compensated is fed with a correct voltage of 360kV provided by a solar power plant with the power of 110 MW. This voltage value can be obtained by a serial connection of the voltage generated by a large number of inverters, although this is not necessary in the simulation operation. The operation of the inverter for solar-powered systems is widespread [6-8], but at the usage of the inverter for the power transmission line, it is difficult to achieve good performance because the alternating voltages that an inverter produces can have a high harmonic distortion. Therefore, it is necessary to use an inverter with a much higher level than the multi-level inverters used up to now. For this reason, unlike in other studies [8-10], the 35-level inverter is used to invert the direct voltage of a solar power plant to an alternating voltage for the power line. Additionally, although inverter applications are circuits for energy conversion and control of electrical machines [12-14], the study is different from other studies because of a solar power plant with a 35-level inverter which feeds an energy transmission line. A solar-powered transmission line covering a long distance is difficult and time-consuming and expensive to test and measure when the line transmits energy and has faults. Therefore, the modeling and simulation of the line are important and necessary applications. The mains frequencies can change from country to country at the same time. So, It is important that the energy transmission line operated by producing voltage with different frequencies from a solar center, including the low-level distortion of the voltage. Thus, after the proposed system has been established, the system is simulated on a power line of 240

km that is fed by alternating voltage at the frequency of 80 Hz. When the simulation is performed, the parallel switch in Fig. 2 for the fault generation at the line is activated from time to time and a fault is generated on the line. Then, the fault current, the flux, and the magnetizing current of the transformer are observed with a multimeter block. The capacitor voltage, the MOV current and the flux of the A2 point are measured by a scope1. According to the obtained results for alternating voltage at 80 Hz, parallel resonances correspond to the 10 Hz and 110 Hz modes. The 10 Hz mode is due to a parallel resonance of the series capacitance and the shunt reactance of the line. The 110 Hz mode occurs due to the resonance effect of the shunt line capacitance and the series reactance of the transmission system. By using these two modes, faults can be eliminated. According to the obtained results for alternating voltage at 50 Hz, parallel resonances correspond to the 5 Hz and 85 Hz modes. The 5 Hz mode is due to a parallel resonance of the series capacitance and the shunt reactance of the line. The 85 Hz mode occurs due to the resonance effect of the shunt line capacitance and the series reactance of the transmission system. By using these two modes, faults can be eliminated while the inverter is producing alternating voltage at 50 Hz. Therefore, some contributions were made as a result. The power line has been tried with switching inverters in the frequency range of 50 - 100 Hz since the mains frequency can vary from country to country. Direct voltage obtained from the solar power plant was transferred to alternating voltage at different frequencies. It was seen that different countries could adapt this model to the power lines because the energy at different frequencies has been successfully transmitted while eliminating faults through the power line. Distortion values on generated voltage from DC voltage in this research were quite acceptable, while the distortion of generated voltage from direct voltage was very high and unacceptable in other studies [15, 16]. Additionally, the distortion of alternating voltage feeding the inspected power line in the open loop control is below 5%, which is the

acceptable level, while the distortion in the producing of DC power in some open loop control operations exceeds 5% in the power system studies [17, 18]. Although it is a difficult, expensive and time-consuming process to work on long lines, this simulated model with MATLAB Simulink measured the response of a solar-powered line in a short time and at a low cost.

2 POWER LINE DESIGN

In the design of electric power lines, which is powered by a solar power plant of 110 MW, is compensated at the center of the line by a capacitor representing 30 % of line reactance for raising the transmission capability at the center of the line. The line is also shunt compensated at both ends by a 165 MVAR shunt reactance (55 MVAR/phase). A metal oxide varistor (MOV) protects the series capacitor from the line. The 110 MVA, 360 kV/180 kV transformer is connected as a saturable transformer simulation block for the

other end of the power line. According to the mentioned, an equivalent circuit model of the line in Fig. 1 is created and the required mathematical equations for modeling are formed with a circuit analysis method.

2.1 Equivalent Circuit Model

The power line to be modeled in MATLAB Simulink is similar to the equivalent circuit of the analysis in Fig. 1. A big solar power plant can be created with multiple solar batteries assembling in one roof connected to a common collecting point. In Fig. 1, the electrical voltage generated by this solar energy is represented as V_S on the circuit model. R_S is the resistance of the transmission line; Z_S is the shunt impedance (R_S , L_S , C_S) of the transmission line. The impedance mathematical values are listed as Eq. (1) and Eq. (2). ω is the angular frequency, $\omega = 2\pi f$.

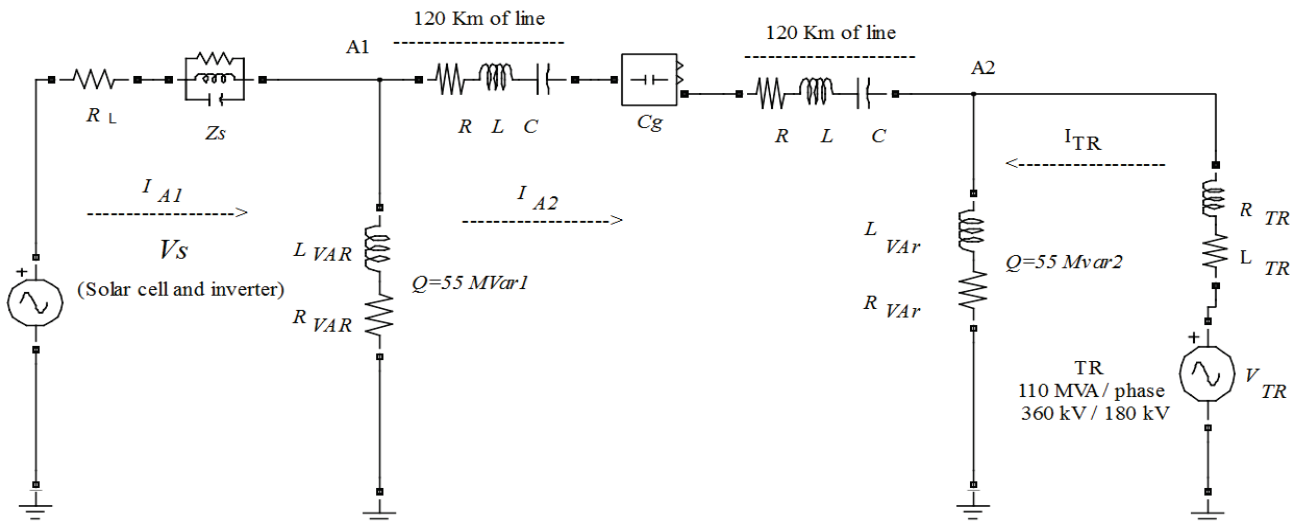


Figure 1 Equivalent circuit of the compensated line for modeling

$$\frac{1}{Z_S} = \frac{1}{R_S} + \frac{1}{j\omega L_S} + \frac{1}{1/j\omega C_S} \quad (1)$$

$$\left[\begin{aligned} \frac{1}{Z_S} &= \frac{j\omega L_S + R_S}{j\omega L_S \cdot R_S} + j\omega C_S \\ \frac{1}{Z_S} &= \frac{1}{\frac{j\omega L_S + R_S}{j\omega L_S \cdot R_S} + j\omega C_S} \\ Z_S &= \frac{j\omega L_S \cdot R_S}{j\omega L_S + R_S - \omega^2 L_S C_S R_S} \end{aligned} \right] \quad (2)$$

V_S represents the voltage obtained by the inverter from the solar power plant, Z_{VAR} represents the parallel impedances forming the reactive power on the line for the line to be modeled. Eq. (3) shows the mathematical equality for Z_{VAR} .

$$Z_{VAR} = j\omega L_{VAR} + R_{VAR} \quad (3)$$

For creating the 240 km of line, two equal RLC series are added to the line. In the simulation model, Z_w is the load impedance representing the 240 km of line. Eq. (4) shows the mathematical equality for Z_w .

$$Z_w = j\omega L + R + \frac{1}{j\omega C} \quad (4)$$

Z_{A1} represents the impedance of the first part of the circuit section with respect to the A1 point. Eq. (5) and Eq. (6) give the mathematical equality of Z_{A1} .

$$Z_{A1} = j\omega L_{VAR} + R_{VAR} + R_L + \frac{j\omega L_S \cdot R_S}{j\omega L_S + R_S - \omega^2 L_S C_S R_S} \quad (5)$$

$$Z_{A1} = Z_S + Z_{VAr} + R_L \quad (6)$$

According to A1 point, the surrounding current equation of the first section can be written as Eq. (7) and Eq. (8). I_{A1} is first section current and I_{A2} is second section current.

$$V_S = I_{A1} \left(j\omega L_{VAr} + R_{VAr} + R_L + \frac{j\omega L_S \cdot R_S}{j\omega L_S + R_S - \omega^2 L_S C_S R_S} \right) - (j\omega L_{VAr} + R_{VAr}) I_{A2} \quad (7)$$

$$V_S = I_{A1} (Z_S + Z_{VAr} + R_L) - (Z_{VAr}) I_{A2} \quad (8)$$

According to A2 point, the surrounding current equations for the line between the A1 and A2 points are found for the simulation model after the first line section of the surrounding current equation is formed. C_g is the series-compensated capacitance for the line. Since there is no source for the second partition, the equation is listed as Eq. (9), Eq. (10) and Eq. (11). I_{TR} is the third section current.

$$0 = I_{A2} \left(2j\omega L_{VAr} + 2R_{VAr} + 2j\omega L + 2R + 2\frac{1}{j\omega C} + \frac{1}{j\omega C_g} \right) - (j\omega L_{VAr} + R_{VAr}) I_{A1} + (j\omega L_{VAr} + R_{VAr}) I_{TR} \quad (9)$$

$$\begin{bmatrix} \left(j\omega L_{VAr} + R_{VAr} + R_L + \frac{j\omega L_S \cdot R_S}{j\omega L_S + R_S - \omega^2 L_S C_S R_S} \right) & (j\omega L_{VAr} + R_{VAr}) & 0 \\ -(j\omega L_{VAr} + R_{VAr}) & \left[2j\omega(L_{VAr} + L) + 2(R_{VAr} + R) + \frac{1}{j\omega} \left(2\frac{1}{C} + \frac{1}{C_g} \right) \right] & (j\omega L_{VAr} + R_{VAr}) \\ 0 & (j\omega L_{TR} + R_{TR}) & (j\omega L_{VAr} + R_{VAr} + j\omega L_{TR} + R_{TR}) \end{bmatrix} \begin{bmatrix} I_{A1} \\ I_{A2} \\ I_{TR} \end{bmatrix} = \begin{bmatrix} V_S \\ 0 \\ V_{TR} \end{bmatrix} \quad (14)$$

$$\begin{bmatrix} (Z_S + Z_{VAr} + R_L) & (Z_{VAr}) & 0 \\ -(Z_{VAr}) & \left(2Z_{VAr} + 2Z_w + \frac{1}{j\omega C_g} \right) & (Z_{VAr}) \\ 0 & (Z_{VAr}) & (Z_{VAr} + Z_{TR}) \end{bmatrix} \begin{bmatrix} I_{A1} \\ I_{A2} \\ I_{TR} \end{bmatrix} = \begin{bmatrix} V_S \\ 0 \\ V_{TR} \end{bmatrix} \quad (15)$$

3 SIMULATION OF THE LINE TO BE COMPENSATED

In Fig. 2, the line fed by the solar energy is created in MATLAB Simulink after the mathematical equations are formed. The simulation of the 240 km line is carried out by using the switching frequencies of 5 microseconds. When a 6-cycle fault is applied with a fault switch at the A2 node, a transient performance of this circuit is tested. Therefore, the fault is simulated by a breaker block. The times of switching can be defined in the breaker block menu.

For a better understanding of the transient behavior of this series-compensating network, a frequency analysis is realized by measuring the impedance at the A2 node. After this measurement is executed by a connecting impedance measurement block, the result is shown in Fig. 3(a). Fig. 3(b)

$$0 = I_{A2} \left[2j\omega(L_{VAr} + L) + 2(R_{VAr} + R) + \frac{1}{j\omega} \left(2\frac{1}{C} + \frac{1}{C_g} \right) \right] - (j\omega L_{VAr} + R_{VAr}) I_{A1} + (j\omega L_{VAr} + R_{VAr}) I_{TR} \quad (10)$$

$$0 = I_{A2} \left(2Z_{VAr} + 2Z_w + \frac{1}{j\omega C_g} \right) - (Z_{VAr}) I_{A1} + (Z_{VAr}) I_{TR} \quad (11)$$

The third part of the line is the part between the A2 point and the transformer, and the third part of the mathematical model is found for the simulation model. The equation is equal to transformer voltage (V_{TR}) because the voltage of the transformer is active in this section.

$$V_{TR} = I_{A2} (j\omega L_{VAr} + R_{VAr}) + I_{TR} (j\omega L_{TR} + R_{TR} + j\omega L_{TR} + R_{TR}) \quad (12)$$

$$V_{TR} = I_{TR} (Z_{VAr} + Z_{TR}) + I_{A2} (Z_{VAr}) \quad (13)$$

For the line to be modeled in MATLAB Simulink, the formed equations are created in matrix form as follows.

shows the shape of alternating voltage and harmonic distortion.

For the simulation model in Fig. 2, R_L is 2 Ω ; Q is 55 VAR for Z_{VAr} . R , L , C values for the impedance of the line (Z_w) are given respectively as 1.331 ohm, 104×10^{-3} H, $C = 1610 \times 10^{-9}$ F on a frequency of 80 Hz. $C_g = 67.6 \times 10^{-6}$ F. $R_S = 180.1 \Omega$, $L_S = 0.026525$ H, $C_S = 117.84 \times 10^{-6}$. The nominal power and frequency are respectively 330. $10^6/3$ VA, 80Hz. The transformer for the winding1 parameters are V_{TR1} , L_{TR1} , $R_{TR1} = 360000/3^{1/3}$, 0.001 Ω , 0.15 H. The transformers for the winding1 parameters are V_{TR2} , L_{TR2} , $R_{TR2} = 180000/3^{1/3}$, 0.001 Ω . For a better understanding of the transient behavior of this series-compensating network, a frequency analysis is realized by measuring the impedance at the A2 node. After this measurement is executed by the connecting impedance measurement block, the result is shown in Fig. 3. Fig. 3 (a)

shows the shape of alternating voltage, while Fig. 3(b) shows harmonic distortion. Since the distortion of the two-cycle alternating voltage is measured, the number of harmonics is larger than that of a single cycle. The harmonic distortion occurring during the conversion of the DC voltage obtained from the solar power plant to the alternating voltage is 2.76%.

This power transmission line is a single-phase transmission line and because the generated alternating voltage is 80 Hz in the inverter output, the main harmonic takes the greatest value at 80 Hz. The renewable direct current voltage from the solar power plant is converted by a 35-level inverter as in Fig. 4.

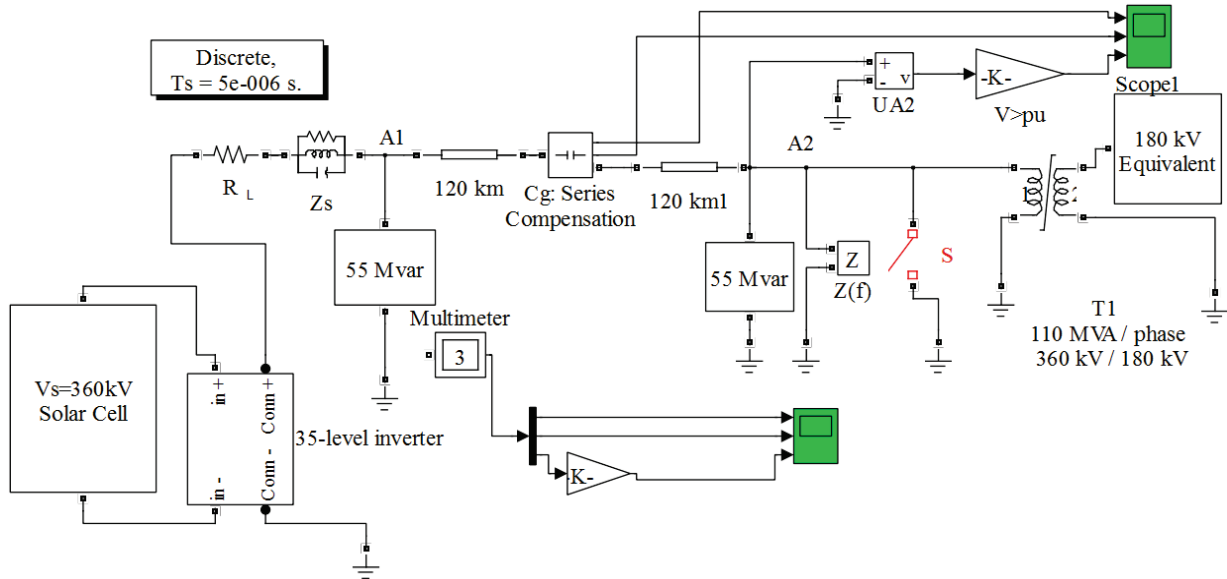


Figure 2 Line fed by solar energy modeled in MATLAB Simulink

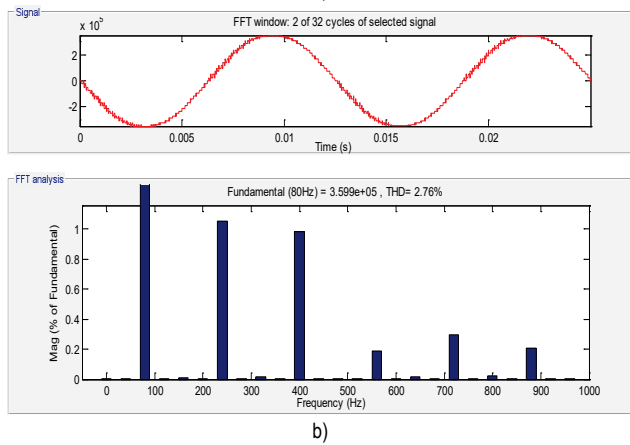
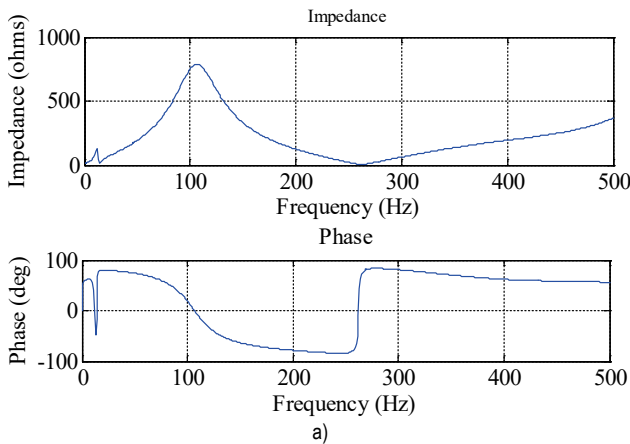


Figure 3 a) Frequency Analysis for alternating voltage at 80 Hz, b) harmonic distortion of alternating voltage converted from a solar power plant

The renewable direct current voltage from solar batteries is converted by a 35-level inverter as in Fig. 4.

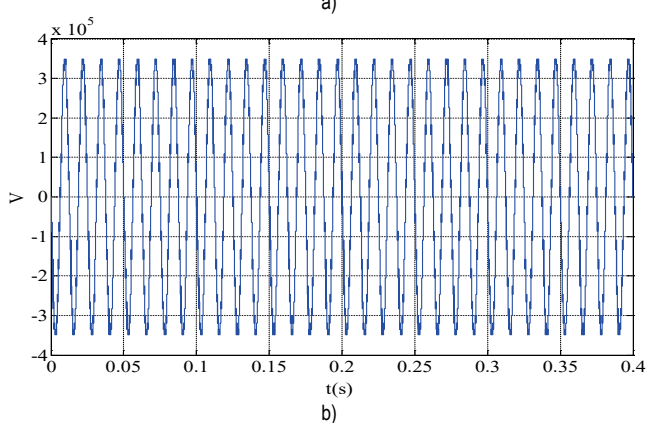
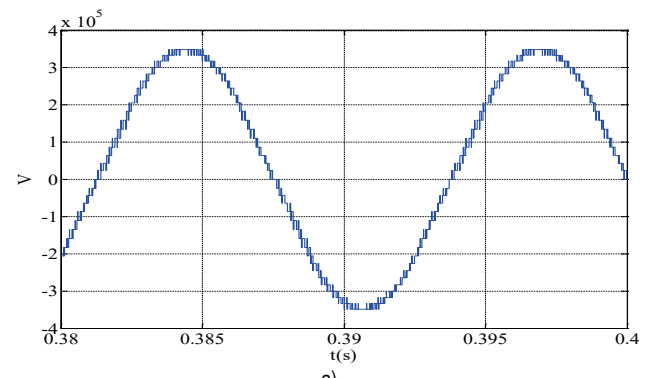


Figure 4 Renewable voltage converted by a 35-level inverter a) short section b) long section

To get the results in Fig. 3, the circuit modeled in MATLAB Simulink is run for 0.4 s. After clicking on the discrete button on the simulation page, the converted voltage and harmonic distortion are obtained by selecting the FFT button from the opened page. Impedance and frequency are clicked and the phase angle and impedance values are taken for a resonance moment as in Fig. 3. According to the impedance curves for the converted voltage from a solar power plant at 80 Hz, parallel resonances correspond to the 10 Hz and 110 Hz modes.

The 10 Hz mode is due to the parallel resonance of series capacitance and the shunt reactance of the line. The 110 Hz mode occurs due to the resonance effect of the shunt line capacitance and the series reactance of the transmission system. By using these two modes, faults can be eliminated. When a conversion of voltage obtained from renewable energy sources is made by a switching inverter circuit, it is difficult that the voltage obtained is close to the sinus. The converted voltage at a sinus shape can be achieved with 35 level inverters in this application. The peak value of 360 kV for a converted wave appears in Fig. 4. The fault current, imaginary transformer current and transformer flux are shown in Fig. 5 when the S switch is turned on and off.

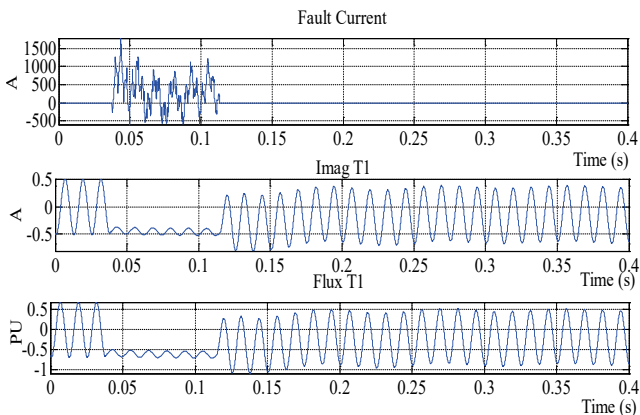


Figure 5 Fault current, imaginary transformer current and transformer flux

When the fault is generated, the transformer flux and the imaginary current decrease by 80% and the fault current reach 800 A. After the fault, ImagT1 is 0.5 A while FluxT1 is 0.5 pu. After the simulation of the line for the alternating voltage at 80 Hz, the capacitor voltage, the current of the MOW and the current of the node A2 appear as shown in Fig. 6.

Capacitor voltage reaches a very high value such as 40 kV and the current of the A2 node is zero from 0.04 s to 1.1s, which is fault duration. After eliminating the fault, capacitor voltage decreases rapidly and becomes stable. After the fault, the flux is at the A2 point as 0.8 pu. After the line is performed for alternating voltage at the 80 Hz, parallel reactive powers are changed to 40 MVar to perform series compensation at 50 Hz. The impedance-frequency response with respect to the A2 point is shown in Fig. 7 when the line is fed with the converted voltage from a solar power plant at 50 Hz.

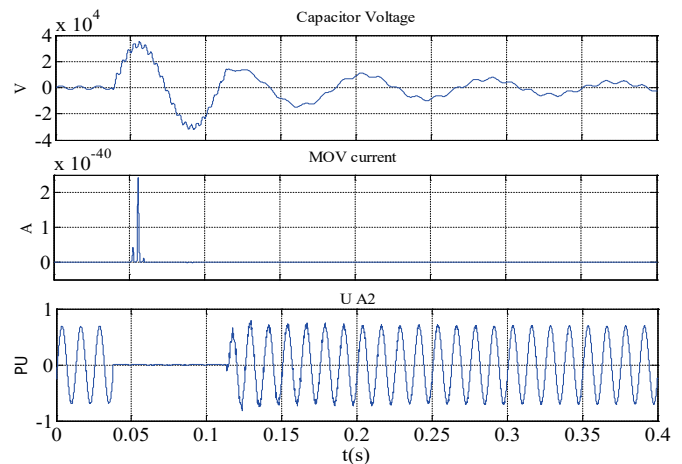


Figure 6 Capacitor voltage, the current of the MOW and the flux of the A2 node at 80Hz

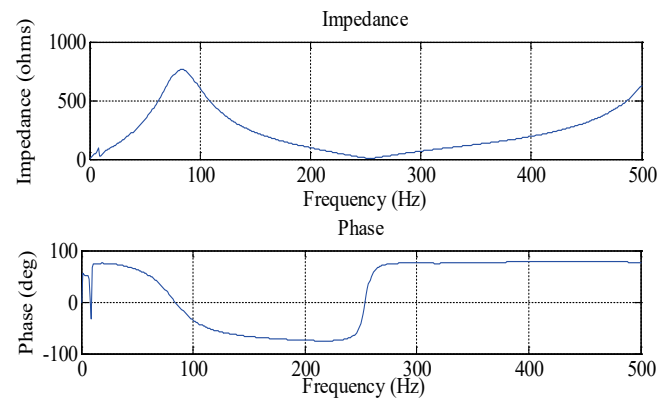


Figure 7a) Frequency Analysis for alternating voltage at 50 Hz

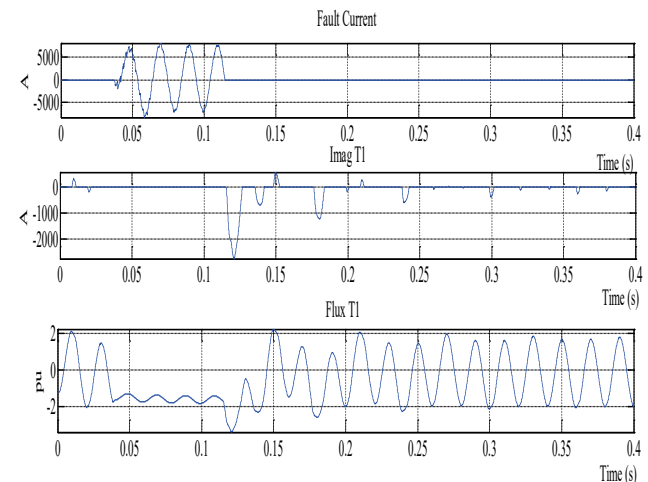


Figure 8 Fault current, ImagT1, and FluxT1

According to the impedance curves for the converted voltage from a solar power plant at 50 Hz, parallel resonances correspond to the 5 Hz and 85 Hz modes. The 5 Hz mode is due to a parallel resonance of the series capacitance and the shunt reactance of the line. The 85 Hz mode occurs due to the resonance effect of the shunt line capacitance and the series reactance of the transmission system. By using these two modes, faults can be eliminated.

After the simulation of the line for alternating voltage at 50 Hz, the capacitor voltage, the current of the MOW and the flux of the A2 node appear in Fig. 9, while Fig. 8 demonstrate the fault current, $ImagT1$, and $FluxT1$.

Fig. 8 shows the fault current, $ImagT1$, and $FluxT1$ for 50 Hz.

Fig. 9 demonstrates capacitor voltage, the current of the MOW and the flux of the A2 node for alternating voltage at 50 Hz.

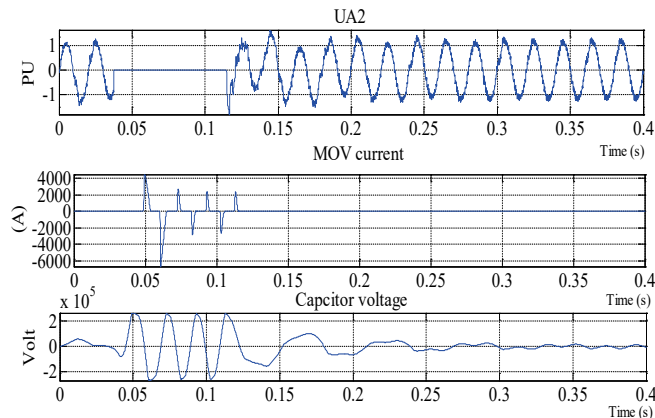


Figure 9 Capacitor voltage, the current of the MOW and the flux of the A2 node for alternating voltage at 50 Hz

At the frequency of 50 Hz, the error current in Fig. 8 is 8000 A, which is why $ImagT1$ and $FluxT1$ become zero. In Fig. 9, after the capacitor voltage reaches 2200 V during the fault, the flux of the UA2 point is 1 pu at 0.13 seconds.

In different frequencies, some variables of the series compensated line are given in Tab. 1.

Table 1 Values of the line at 80 Hz and 50 Hz

	Flux of A2	Q	Resonance frequencies	Capacitor voltages	FluxT1
80 Hz	0.8 pu	55 MVar	10/115 Hz	40 kV	0.5 pu
50 Hz	1.2 pu	40 MVar	5/85 Hz	24 kV	2 pu

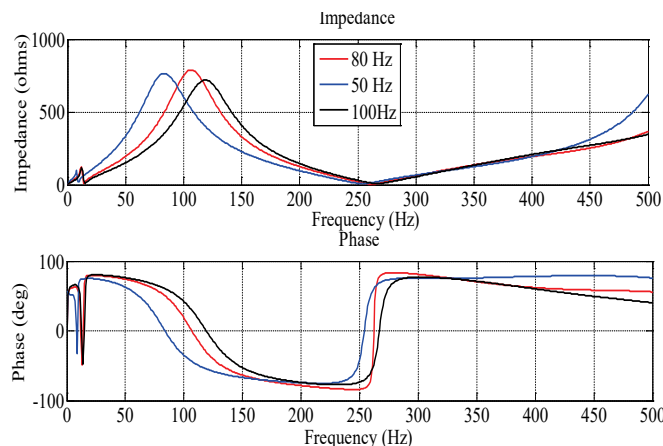


Figure 10 Frequency response of the power line at the 50Hz, 80Hz and 100Hz frequencies

Capacitor voltage is at a very high value such as 25 kV and the flux of the A2 node is zero from 0.04 s to 1.1 s, which is fault duration. After eliminating the fault, capacitor voltage

decreases rapidly and becomes stable. After the fault, the current flows at the A2 point as 1.2 pu.

The flux of the A2 point rises from 0.8pu to 1.2pu due to the frequency dropping from 80 Hz to 5 Hz and the reactive power dropping from 55 MVar to 40 MVar. In this way, the power line powered by solar energy at different frequencies is successfully serial-compensated.

At 50 Hz, 80 Hz and 100 Hz frequencies, the frequency response of the power line appears in Fig. 10.

When the frequency of the alternating voltage obtained from solar energy changes from a frequency of 50 Hz to 100 Hz, the frequency response of the line is shifted from 85 Hz to 125 Hz due to the resonance effect of the line reactance and the parallel line capacitance of the transmission line. The impedance values at these frequencies vary from 750 Ω to 800 Ω. Therefore, while the line is fed by the voltages at different frequencies obtained from solar energy, the condition of the line can be observed. In the application of a renewable energy source with switching inverters, since the mains frequency can vary from country to country, the power line has been tried in the frequency range of 50 - 100 Hz. Furthermore, the energy was then successfully transmitted with the eliminated faults through the power line.

4 CONCLUSION

In this article, when the fault was occurring on the transmission line of 240 km while obtaining voltage at a different frequency with the 35-level inverter from solar energy, the response of the power line at the case of compensation of this fault was investigated in the MATLAB Simulink. So, mathematical models of the power line were created and then the simulation model was tested in MATLAB Simulink.

According to the simulation results for the converted voltage from a solar power plant at 80 Hz, parallel resonances corresponded to the 10 Hz and 110 Hz modes. The 10 Hz mode was due to a parallel resonance of the series capacitance and the shunt reactance of the line. The 110 Hz mode occurred due to the resonance effect of the shunt line capacitance and the series reactance of the transmission system. It was seen that the fault current reached 1750 amperes when the fault at the line was created with the switch. The capacitor voltage was 40 kV when the current of the A2 point was zero from 0.04 s to 1.1 s, at which the fault occurred. According to the simulation results for the converted voltage from a solar power plant at 50 Hz, parallel resonances corresponded to the 5 Hz and 85 Hz modes. The 5 Hz mode was due to a parallel resonance of the series capacitance and the shunt reactance of the line. The 85 Hz mode occurred due to the resonance effect of the shunt line capacitance and the series reactance of the transmission system. The energy transmission on the compensated line continued to be balanced and smooth after the fault had been fixed. The harmonic distortion of the alternating voltage generated by the inverter on the power line was 2.78% and the acceptable value is below 5%. Although it is a difficult, expensive and time-consuming process to work on long lines, this simulated model with MATLAB Simulink

measures the response of a solar-powered line in a short time and at a low cost.

4 REFERENCES

- [1] Millstein, D., Wiser, R., Bolinger, M., & Barbose, G. (2017). The climate and air-quality benefits of wind and solar power in the United States. *Nature Energy*, 2(9), nenergy2017134. <https://doi.org/10.1038/nenergy.2017.134>
- [2] François, B., Zoccatelli, D., & Borga, M. (2017). Assessing small hydro/solar power complementarity in ungauged mountainous areas: A crash test study for hydrological prediction methods. *Energy*, 127, 716-729. <https://doi.org/10.1016/j.energy.2017.03.090>
- [3] Yang, Y., Zhong, W., Kiratipongvoot, S., Tan, S. C., & Hui, S. R. (2017). Dynamic Improvement of Series-Series Compensated Wireless Power Transfer Systems Using Discrete Sliding Mode Control. *IEEE Transactions on Power Electronics*.
- [4] Bogdan, A. V. & Tropin, V. V. (2017, May). Analysis of transient start asynchronous motor series compensated reactive power. *International Conference on Industrial Engineering, Applications and Manufacturing (ICIEAM 2017), IEEE*, 1-4.
- [5] Feng, H., Cai, T., Duan, S., Zhang, X., Hu, H., & Niu, J. (2017). A Dual-Side Detuned Series-Series Compensated Resonant Converter for Wide Charging Region in Wireless Power Transfer System. *IEEE Transactions on Industrial Electronics*.
- [6] Liu, J., Sun, Y., Li, Y., & Fu, C. (2016). Theoretical harmonic analysis of cascaded H-bridge inverter under hybrid pulse width multilevel modulation. *IET Power Electronics*, 9(14), 2714-2722. <https://doi.org/10.1049/iet-pel.2016.0163>
- [7] Xavier, L. S., Cupertino, A. F., de Resende, J. T., Mendes, V. F., & Pereira, H. A. (2017). Adaptive current control strategy for harmonic compensation in single-phase solar inverters. *Electric Power Systems Research*, 142, 84-95. <https://doi.org/10.1016/j.epsr.2016.08.040>
- [8] Saygin, A.; Aksoz, A.; Yilmaz, (2016). E. N. A different model of WECS connected to smart grid through matrix converter. *Smart Grid Congress and Fair (ICSG2016), 4th International IEEE, Istanbul*, 1-5.
- [9] Xavier, L. S., Cupertino, A. F., Mendes, V. F., & Pereira, H. A. (2015, November). A novel adaptive current harmonic control strategy applied in multifunctional single-phase solar inverters. *Power Electronics Conference and 1st Southern Power Electronics Conference (COBEP/SPEC2015) IEEE 13th Brazilian*, 1-6.
- [10] Li, R., Wang, W., Chen, Z., Jiang, J., & Zhang, W. (2017). A Review of Optimal Planning Active Distribution System: Models, Methods, and Future Researches. *Energies*, 10(11), 1715. <https://doi.org/10.3390/en10111715>
- [11] Liu, Y., Meliopoulos, S., Tai, N., Sun, L., & Xie, B. (2017). Protection and Fault Locating Method of Series Compensated Lines by Wavelet Based Energy Traveling Wave. *IEEE Power and Energy Society (PES) General Meeting*.
- [12] Can, E. (2017). Novel high multilevel inverters investigated on simulation. *Electrical Engineering*, 99(2), 633-638. <https://doi.org/10.1007/s00202-016-0396-z>
- [13] Can, E. & Sayan, H.H. (2016). PID and fuzzy controlling three phase asynchronous machine by low level DC source three phase inverter. *Tehnički vjesnik*, 23 (3), 753-760. <https://doi.org/10.17559/TV-20150106105608>
- [14] Kerem, A., Aksoz, A., Saygin, A., & Yilmaz, E. N. (2017). Smart grid integration of micro hybrid power system using 6-switched 3-level inverter. *Smart Grid and Cities Congress and Fair (ICSG2017) 5th International IEEE, Istanbul*, 161-165. <https://doi.org/10.1109/SGCF.2017.7947625>
- [15] Can, E. & Sayan, H.H. (2016). SSPWM three phase inverter design and experimented on unbalanced loads. *Tehnički vjesnik*, 23 (5), 1239-1244. <https://doi.org/10.17559/TV-20150730222021>
- [16] Sarwar, A., & Asghar, M. S. (2011). Simulation and analysis of a multilevel converter topology for solar PV based grid-connected inverter. *Smart Grid and Renewable Energy*, 2(1), 56. <https://doi.org/10.4236/sgre.2011.21007>
- [17] Yelpale, P. R., Jadhav, H. T., & Chormale, C. (2017). New control strategy for grid integrated PV solar farm to operate as STATCOM. *International Conference on Circuit, Power and Computing Technologies (ICCPCT2017), IEEE*, 1-6.
- [18] Sinu, K. J. & Ranganathan, G. (2018). A PV FED Three Phase Switched Z-Source Multi Level Inverter for Induction Motor Drives. *Indonesian Journal of Electrical Engineering and Computer Science*, 9(1), 24-28. <https://doi.org/10.11591/ijeecs.v9.i1.pp24-28>

Author's contacts:

Erol CAN, Assist. Prof. Dr.
 School of Civil Aviation, Erzincan University,
 Aircraft Airframe Power Plant,
 Yanliz Bag Yerleşkesi, 24100 Erzincan, Turkey
 cn_e@hotmail.com

NUMERICAL INVESTIGATION OF HEAT AND MASS TRANSFER INSIDE A WET COOLING TOWER

Paolo BLECICH, Tomislav SENČIĆ, Igor WOLF, Igor BONEFAČIĆ

Abstract: This paper presents a numerical investigation of heat and mass transfer inside a wet cooling tower with forced air draft, which find application in energy process industries and oil refineries. The mathematical model consists of mass, momentum and energy conservation equations, water droplet trajectories and their interaction with the gas phase, the computational domain and boundary conditions. Numerical distributions of air velocity, air temperatures, water vapor fractions and evaporation rates are shown and discussed. The wet cooling tower achieves an efficiency of around 80%, which can be improved by optimizing the value of the water droplet size, nozzle spray angle and water-to-air flow rate ratio. The water droplet size has a dominant effect on the cooling tower efficiency, whereas small droplets improve the efficiency up to 10%. On the other hand, the spray angle and the water-to-air ratio lead to slight improvements, about 2-3% in the best case.

Keywords: cooling tower; forced air draft; latent heat transfer; numerical modeling; water evaporation

1 INTRODUCTION

A cooling tower is a device that transfers waste heat from the warmer working fluid (usually water) into the colder ambient air (atmosphere). Cooling towers find numerous applications, such as in the energy and chemical process industries, in oil refineries, thermal power plants, in heating and air-conditioning systems for buildings [1-2]. The principal parts of a cooling tower are: the reinforced concrete shell, air intake and air discharge sections, mechanical fans with motors, warm water distribution system with spray nozzles, cold water collection basin, PVC filling (exchange surface), and drift eliminator. Cooling towers replace water-cooled heat exchangers when large bodies of water are not available nearby, or their use would be economically or environmentally unsustainable.

Depending on the heat transfer method, two main types of cooling towers exist [3]. In the first type, dry cooling towers, heat transfer occurs only by convection. The water stream is cooled to near the dry-bulb temperature of air. This is achieved by physically separating the water stream from the ambient air with heat exchanging surfaces. Wet cooling towers, on the other hand, work with the principle of evaporative cooling. The water stream is sprayed into the air stream, which allows for both sensible and latent heat transfer. Here, the water stream is cooled to near the wet-bulb temperature of air, which is lower than the dry-bulb temperature, thus making wet cooling towers more efficient.

Heat transfer can be intensified by mechanical air draft, where power-driven fans increase the airflow, unlike natural air draft where the airflow is buoyancy-induced [4]. Mechanical fans are placed either at the air intake side (forced draft) or at the air discharge side (induced draft). With respect to the flow arrangement between air and water streams, there are crossflow, counterflow and parallelflow cooling towers. Cooling towers with counterflow arrangement, where the air flow is opposite to the water flow, generally achieve superior efficiency.

The heat and mass transfer processes in different types of cooling towers have been subject of extensive scientific research. These studies include experimental and numerical investigations of thermal and hydraulic performance of mechanical air draft wet cooling towers with counterflow [5], parallelflow [6], and crossflow arrangements [7, 8], as well as natural air draft dry cooling towers with adjacent Savonius turbines [9], solar preheating of the airflow [10], water redistribution systems [11], water systems with vertical and horizontal spray nozzles [12]. All of these solutions aim to increase the cooling tower efficiency.

This paper analyses the heat and mass transfer phenomena inside a wet cooling tower with forced air draft and counterflow arrangement between air and water stream. The scientific contribution of this study is in the application of the porous zone model with appropriate sink terms for the momentum conservation equations in the mathematical model of the cooling tower. This is a novel approach for the treatment of heat and mass transfer in the filling of the cooling tower. Furthermore, the numerical analysis expands the study about the parameters affecting the cooling tower performance, such as the water droplet size, the water-to-air ratio and the nozzle spray angle. The analyzed cooling tower is part of the cooling tower system in the fuel refinery INA Rijeka (Urinj) [13, 14].

2 MATHEMATICAL MODEL

2.1 Approach

The numerical modeling approach includes the choice of a suitable mathematical model. The mathematical model consists of mass, momentum and energy conservation equations, and of the equations describing the trajectories of the discrete phase (water droplets) and their interaction with the continuous phase (air), as well as of the cooling tower computational domain with the boundary conditions. The numerical analysis of heat and mass transfer in the cooling tower is carried using the computer software ANSYS Fluent.

The computational domain is discretized with the finite volume method while the unknown quantities at the finite volume boundaries are calculated using the second order upwind scheme [15]. The coupling between the flow velocity field and the pressure field is performed by the SIMPLE algorithm.

2.2 Computational Domain

The cooling tower studied in this paper is a model representation of the real cooling tower, which operates as one in the eight-unit cooling tower system of the INA fuel refinery, shown in Fig. 1. The real cooling tower contains 192 water nozzles, which would be unpractical to model all numerically. To facilitate the numerical analysis, the real cooling tower was downsized 16 times in terms of the number of nozzles. Thus, the numerical cooling tower contains only 12 nozzles and one-sixteenth of the air and water mass flow rates. Nevertheless, the water-to-air mass flow rate remains equal, which ensures the validity of this approach. The computational domain is chosen taking into account the geometry of the real cooling tower, its physical phenomena but also the available computer resources. The two-dimensional cross-section of the cooling tower is identified as the computational domain since the airflow is two-axis dominant, as shown in Figure 2. The domain is meshed with 465 000 quadrilateral finite volumes and the average size of which is 4 cm².



Figure 1 The cooling towers of the INA fuel refinery. At the forefront: water supply pipes and air intake.

2.3 Conservation Equations

The air flow in the cooling tower is modeled using the steady-state turbulent model. The system of partial differential equations include mass, momentum and energy conservation for two-dimensional steady-state turbulent airflow in the cooling tower. Their solutions yield the flow velocity, pressure and temperature fields in the cooling tower. The mass conservation equation reads

$$\frac{\partial(\rho w_x)}{\partial x} + \frac{\partial(\rho w_y)}{\partial y} = 0 \quad (1)$$

The momentum conservation (Navier-Stokes) equations are

$$\frac{\partial(\rho w_x w_x)}{\partial x} + \frac{\partial(\rho w_x w_y)}{\partial y} = \frac{\partial}{\partial x} \left(\eta \frac{\partial w_x}{\partial x} \right) + \frac{\partial}{\partial y} \left(\eta \frac{\partial w_x}{\partial y} \right) - \frac{\partial p}{\partial x} + S_{M_x} \quad (2)$$

$$\frac{\partial(\rho w_y w_x)}{\partial x} + \frac{\partial(\rho w_y w_y)}{\partial y} = \frac{\partial}{\partial x} \left(\eta \frac{\partial w_y}{\partial x} \right) + \frac{\partial}{\partial y} \left(\eta \frac{\partial w_y}{\partial y} \right) - \frac{\partial p}{\partial y} - \rho g + S_{M_y} \quad (3)$$

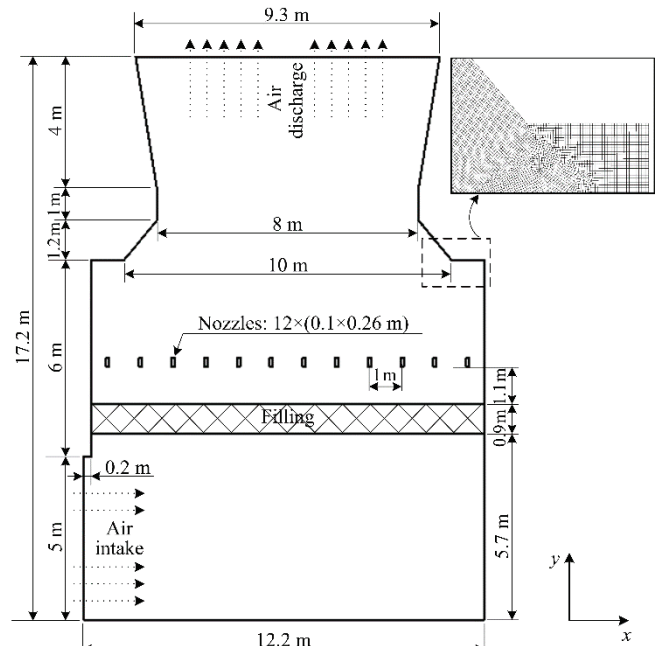


Figure 2 The computational domain with a meshing detail

The air flow in the cooling tower is turbulent and the velocity components (w_x and w_y) are expressed as sums of their mean (\bar{w}_x and \bar{w}_y) and fluctuating terms (w_x' and w_y'). Therefore, additional equations are necessary for each of the momentum conservation equations. In the standard k - ϵ turbulence model, the equations for the turbulence kinetic energy (k) and its rate of dissipation (ϵ) are

$$\frac{\partial}{\partial x_i} (\rho \bar{w}_i k) = \frac{\partial}{\partial x_j} \left[\left(\eta + \frac{\eta_t}{\sigma_k} \right) \frac{\partial k}{\partial x_j} \right] - \rho \left[\overline{w_i' w_j'} \frac{\partial \bar{w}_j}{\partial x_i} - \epsilon \right] \quad (4)$$

$$\frac{\partial}{\partial x_i} (\rho \bar{w}_i \epsilon) = \frac{\partial}{\partial x_j} \left[\left(\eta + \frac{\eta_t}{\sigma_\epsilon} \right) \frac{\partial \epsilon}{\partial x_j} \right] - \rho \left[\overline{w_i' w_j'} \frac{\partial \bar{w}_j}{\partial x_i} C_{1\epsilon} - \epsilon C_{2\epsilon} \right] \frac{\epsilon}{k} \quad (5)$$

The Boussinesq hypothesis gives the relationship between Reynolds stresses and the mean velocity gradients as

$$-\overline{\rho w_i' w_j'} = \eta_t \left(\frac{\partial \bar{w}_i}{\partial x_j} + \frac{\partial \bar{w}_j}{\partial x_i} \right) - \frac{2}{3} \rho k \delta_{ij} \quad (6)$$

The turbulent (eddy) viscosity is calculated as

$$\eta_t = \frac{\rho C_\mu k^2}{\varepsilon} \quad (7)$$

The model constants in the standard k - ε turbulence model are the following: $C_{1\varepsilon} = 1.44$, $C_{2\varepsilon} = 1.92$, $C_\mu = 0.09$, $\sigma_k = 1.0$, $\sigma_\varepsilon = 1.3$. Heat transfer in the continuous phase (air) of the cooling tower is described by the energy conservation equation, i.e.

$$\frac{\partial(\rho w_x T)}{\partial x} + \frac{\partial(\rho w_y T)}{\partial y} = \frac{\partial}{\partial x} \left(\frac{\lambda_\infty}{c_p} \frac{\partial T}{\partial x} \right) + \frac{\partial}{\partial y} \left(\frac{\lambda_\infty}{c_p} \frac{\partial T}{\partial y} \right) + S_q \quad (8)$$

The above conservation equations are complemented with equations for the water droplets trajectories and the heat and mass transfer between water droplets and air. The tracking of water droplets in the gas phase is specified using the Lagrangian approach [15]. The equation that describes the water droplet trajectory is an equilibrium equation for forces acting on droplets. The droplet velocity depends on aerodynamic resistance, gravity and pressure gradients, i.e.

$$\frac{dw_{p,j}}{dt} = \frac{3 C_D}{4 d_p} \frac{\rho}{\rho_p} (w_j - w_{p,j})^2 + \frac{g_j (\rho_p - \rho)}{\rho_p} + \frac{\rho}{\rho_p} w_{p,j} \frac{dw_j}{dx_j} \quad (9)$$

In Eq. (9), the variables related to the water droplets are the velocity w_p , the density ρ_p and the droplet diameter d_p while those describing the gas phase are the velocity w and the density ρ . The aerodynamic drag coefficient of the droplets is denoted with C_D . The turbulent dispersion of water droplets in the gas phase is described by the stochastic discrete random walk model, which takes into account the effect of turbulent fluctuations on droplet trajectories. The energy conservation equation for water droplets describes the heat transfer mechanisms between the discrete phase and the continuous phase. The change in heat content of a water droplet due to convective, radiative and evaporative heat transfer is given by

$$m_p c_p \frac{dT_p}{dt} = \alpha A_p (T_\infty - T_p) + \varepsilon_p A_p \sigma (T_R^4 - T_p^4) + r \frac{dm_p}{dt} \quad (10)$$

Eq. (10) defines the quantity of heat transferred from water droplets into the gas phase, which is also the heat source term S_q in Eq. (8). In Eq. (10), the other variables are as follows: the water droplet mass m_p , its heat capacity c_p , surface area A_p and emissivity ε_p , the air temperature T_∞ , the heat transfer coefficient α , the radiation constant σ , and the temperature T_R . Dalton's law of evaporation defines the rate of mass transfer from water droplets to the gas phase

$$\frac{dm_p}{dt} = -k_m (C_g - C_\infty) A_p M_w \quad (11)$$

In Eq. (11), the evaporation rate depends on the mass transfer coefficient k_m , the difference in vapor concentration at the droplet surface and in the gas phase ($C_g - C_\infty$), the droplet surface area A_p , and the molar mass of water vapor M_w . The vapor concentrations are calculated from the ideal gas law. The partial pressure of vapor at the droplet surface is equal to the saturated pressure ($p_g = p_s$) at the droplet temperature T_p , while the partial pressure in the gas phase is determined by Dalton's law of partial pressures ($p_\infty = r_v p$)

$$C_g = \frac{p_g}{RT_p}, \quad C_\infty = \frac{r_v p}{RT_\infty} \quad (12)$$

The heat and mass transfer coefficients α and k_m , in Eqs. (10)-(11), are determined by the Ranz-Marshall correlations [16] for the Nusselt (Nu) and the Sherwood (Sh) number

$$Nu = \frac{\alpha d_p}{\lambda} = 2 + 0.6 Re_d^{1/2} Pr^{1/3} \quad (13)$$

$$Sh = \frac{k_m d_p}{D_m} = 2 + 0.6 Re_d^{1/2} Sc^{1/3} \quad (14)$$

Above, D_m is the diffusion coefficient of water vapor in the gas phase, λ is the thermal conductivity of air, and the dimensionless quantities are the Reynolds (Re), Prandtl (Pr) and Schmidt (Sc) numbers. The filling of the cooling tower, which increases the contact surface between water droplets and air, is modeled using the porous zone model. The turbulent flow in the cooling tower filling is described by Eqs. (1)-(8) with the addition of momentum sink terms S_{M_x} and S_{M_y} . The momentum sink terms consist of a viscous loss term and an inertial loss term, that is

$$S_{M_i} = -(C_1 \eta w_i + C_2 \rho w_i^2) \quad (15)$$

The coefficients for the two loss terms are derived from the Ergun semi-empirical correlation [17]

$$C_1 = \frac{150(1-\sigma)^2}{\varphi^2 d_{el}^2 \sigma^3}, \quad C_2 = \frac{1.75(1-\sigma)}{\varphi d_{el} \sigma^3} \quad (16)$$

The filling comprises 1440 elements made of hard PVC and of thickness 0.2 mm. The dimension of each element is $1.2 \times 0.3 \times 0.3$ m. Its mass and surface area per unit of volume are 36 kg/m^3 and $243 \text{ m}^2/\text{m}^3$, respectively. The porosity is $\sigma = 0.97$, the characteristic length of the element is $d_{el} = 50$ cm and its sphericity $\varphi = 0.002$. Returning these quantities into (16), the values of the loss terms coefficients are $C_1 = 147917 \text{ m}^{-2}$ and $C_2 = 58 \text{ m}^{-1}$. In the subdomain of the cooling tower filling, the effective thermal conductivity (λ_{ef}) replaces the thermal conductivity of air (λ_∞). It is obtained by averaging the thermal conductivities of the filling material (λ_s) and air over the filling porosity, that is

$$\lambda_{\text{eff}} = \sigma \lambda_{\infty} + (1 - \sigma) \lambda_s \quad (17)$$

2.4 Boundary Conditions

At the air intake of the cooling tower, air mass flow rate, air temperature and participants' mass fractions are defined. The air mass flow rate is 31.75 kg/s and the velocity vector is normal to the inlet cross section. The inlet air temperature and relative humidity are 302 K and 60%, whereas the wet bulb temperature is 296 K. The mass fractions of species in the inlet air are nitrogen 0.755, oxygen 0.23 and water vapor 0.015. The physical properties of air are calculated by interpolating the physical properties of the individual participants. The density is calculated with the incompressible ideal gas state equation. The dynamic viscosity is determined by the three coefficients method of Sutherland's law. The boundary condition of pressure outlet is applied at the air discharge, ensuring good solution convergence in case of backflow or recirculation. The walls of the cooling tower shell are adiabatic since the heat exchange with the environment is negligible compared to the heat transfer inside the cooling tower. The warm water mass flow rate is 26.16 kg/s and the inlet water temperature is 311 K. The water flow rate is uniformly distributed into 12 nozzles that eject water droplets with a spray angle of 135°, counterflow to the air flow. The spray nozzles are modeled as discrete phase injections and their positions in the cooling tower are shown in Fig. 2. The Rosin-Rammler function describes the size distribution of water droplets, with user-defined values for the range of droplet diameters. The minimum, mean and maximum diameters in the Rosin-Rammler distribution are 1 mm, 1.5 mm and 2 mm, respectively. The material of the tower filling is high-density PVC with the following properties: density $\rho_s = 1300 \text{ kg/m}^3$, specific heat capacity $c_s = 900 \text{ J/kgK}$, thermal conductivity $\lambda_s = 0.19 \text{ W/mK}$. In the filling, a constant temperature of 311 K is assumed while the heat transfer coefficient of $40 \text{ W/m}^2\text{K}$ is determined from (11) taking an air velocity of 2.3 m/s. The effective thermal conductivity in the filling subdomain is calculated with (17).

3 RESULTS AND ANALYSIS

3.1 Numerical Field Data

The following results are shown for a wet cooling tower with an air mass flow rate of 31.75 kg/s and a water flow rate of 26.16 kg/s, which returns a water-to-air flow rate ratio of 0.824. The air temperature and relative humidity at the intake are 29 °C and 60%. The wet bulb air temperature is 23 °C. Warm water is supplied at a temperature of 38 °C. Fig. 3 shows the air velocity magnitude and direction in the cooling tower. The air velocity at the cooling tower entrance is 5.5 m/s, after which it decreases gradually and its direction turns towards the discharge. A recirculation zone generating low air velocity is attached to the left wall of the cooling tower, around the left-most nozzles. In addition to that, the air flow slows down at the bottom right side of the cooling tower, where it turns abruptly upwards. These zones with low air

velocity have reduced evaporation rate which negatively affects the cooling tower overall performance. On the other hand, the highest air velocity occurs at the right wall of the cooling tower, around the right-most nozzles, where it hits the walls and turns upwards.

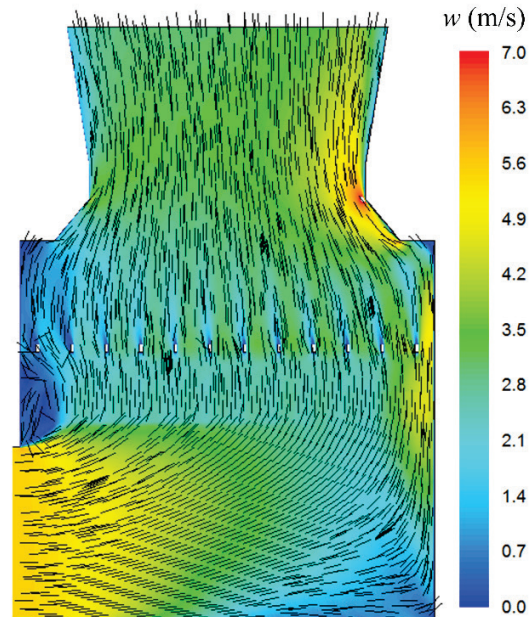


Figure 3 Air flow velocity and direction in the cooling tower

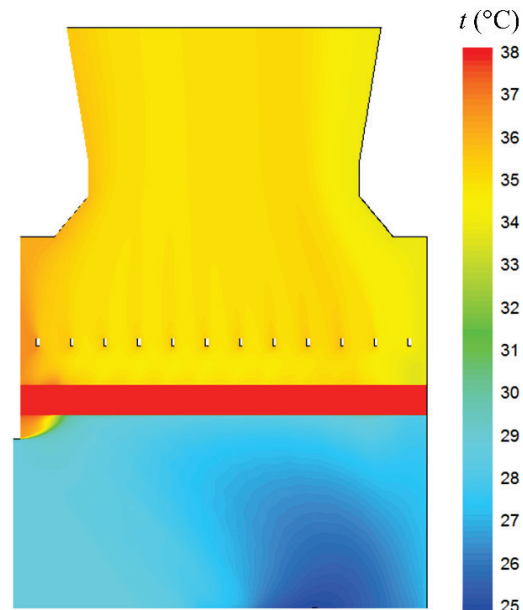


Figure 4 Air temperature in the cooling tower

Fig. 4 shows the air temperature distributions in the cooling tower. The air inlet temperature is 29 °C and the water inlet temperature is 38 °C. In the region below the filling, air is cooled by a few degrees due to the dominant effect of evaporative cooling. On the other hand, sensible heat transfer is dominant in the filling and air is heated by the warm water droplets and filling surfaces. The mean air temperature at the discharge is 35.1 °C.

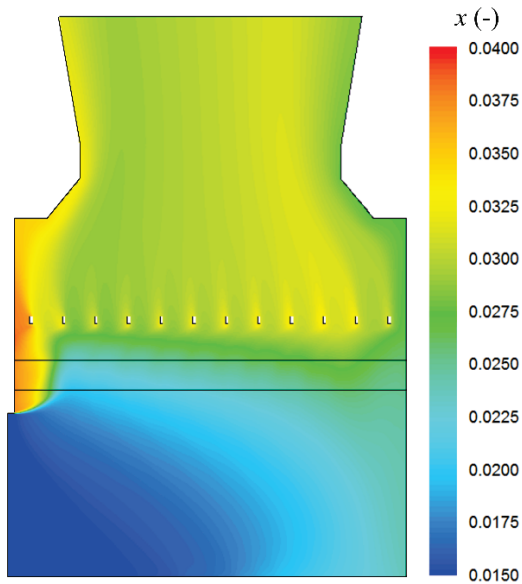


Figure 5 Mass fraction of water vapor in the cooling tower

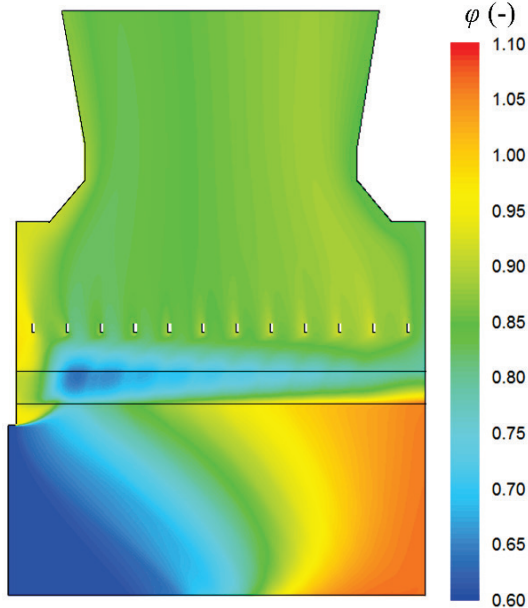


Figure 6 Relative humidity of air in the cooling tower

The mass fraction of water vapor in the gas phase (specific humidity or moisture content, x) is depicted in Fig. 5. The mass fraction of water vapor at the intake is 0.015 and increases as air flows towards the discharge. The mass fraction of vapor at the discharge is 0.03007. The highest mass fraction of 0.04 occurs in the recirculation zone attached to the left wall of the cooling tower. Here, air is stagnant and becomes saturated with vapor because of the reduced flow of fresh air. Fig. 6 shows the relative humidity of air in the cooling tower. The relative humidity of air is 0.6 at the intake and 0.86 at the discharge. In the bottom right zone of the tower, the relative humidity of air is greater than 1.0, which means that air is supersaturated and that water vapor condenses to form droplets.

Fig. 7 shows water droplet trajectories colored by the local rate of evaporation. The droplet trajectories are deflected to the right under the force of the incoming air flow. The rate of evaporation is the highest just below the nozzles and along the trajectories of the droplets. The evaporation rate reduces in the bottom part of the cooling tower as air humidity increases up to the point of saturation.

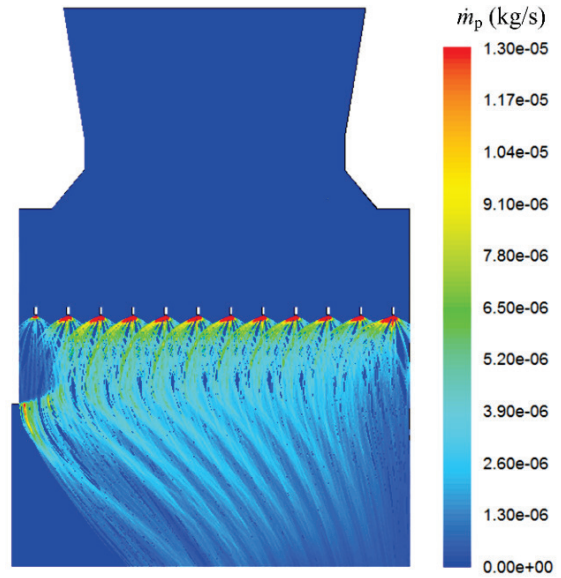


Figure 7 Water droplet trajectories and rate of evaporation

3.2 Evaporation Loss

The amount of evaporated water from the cooling tower can be determined using the results shown in Figure 5. The mass fraction of water vapor increases from 0.015 at the intake to 0.03 at the discharge. Thus, the mass of evaporated water per unit of air flow is 0.015 kg/kg. Taking into account that the air mass flow in the cooling tower is 31.75 kg/s, the evaporation loss is 0.476 kg/s. Since the water mass flow rate in the cooling tower is 26.16 kg/s, the loss of evaporation is 1.82%. The water lost to evaporation must be replaced in order to maintain the cooling tower in steady operation. Usually, wet cooling towers exhibit evaporation losses between 1% and 2%, as reported by [3].

3.3 Energy Balance and Efficiency of the Cooling Tower

The mass balances for dry air and water in the cooling tower are

$$\dot{m}_{\text{air, in}} = \dot{m}_{\text{air, out}} \quad (18)$$

$$\dot{m}_{\text{water, out}} = \dot{m}_{\text{water, in}} - \dot{m}_{\text{air}}(x_{\text{out}} - x_{\text{in}}) \quad (19)$$

The water mass balance (19) accounts for the evaporation losses by taking into account the difference in the mass fractions of water vapor at the intake and discharge. The energy balance of a cooling tower with negligible heat loss to the ambient (adiabatic cooling tower) states that the heat

content in the inlet streams is equal to that of the outlet streams, that is

$$\begin{aligned} \dot{m}_{air}h_{air, in} + \dot{m}_{water, in}h_{water, in} &= \\ &= \dot{m}_{air}h_{air, out} + \dot{m}_{water, out}h_{water, out} \end{aligned} \quad (20)$$

The increase in the heat content of air is due to the change in sensible and latent heat contents, that is

$$\begin{aligned} \dot{m}_{air}(h_{air, out} - h_{air, in}) &= \\ &= \underbrace{\dot{m}_{air}c_p(t_{air, out} - t_{air, in})}_{\text{sensible heat}} + \underbrace{\dot{m}_{air}r(x_{out} - x_{in})}_{\text{latent heat}} \end{aligned} \quad (21)$$

The unknown in the energy balance is the water temperature at the cooling tower outlet, which can be determined by putting (19) and (21) in (20) and rearranging

$$\begin{aligned} t_{w, out} &= \\ &= \frac{\dot{m}_{w, in}c_w t_{w, in} - \dot{m}_{air} [c_p(t_{air, out} - t_{air, in}) + r(x_{out} - x_{in})]}{[\dot{m}_{w, in} - \dot{m}_{air}(x_{out} - x_{in})]c_w} \end{aligned} \quad (22)$$

The specific heat capacities of air and water are 1006 J/kgK and 4179 J/kgK, respectively. The latent heat of water evaporation is 2420 kJ/kg and the water inlet temperature is 38 °C. The air temperature is 29 °C at the inlet and 35.1 °C at the outlet. The mass flow rates of air and water are 31.75 kg/s and 26.16 kg/s, respectively. The mass fractions of water vapor in the air at the inlet and at the outlet are 0.015 and 0.3007, respectively.

From (21), the total rejected heat in the cooling tower is 1352 kW, where the latent heat transfer is 1158 kW and the sensible heat transfer is 194 kW. Latent heat transfer is the dominant heat transfer method in the wet cooling tower with a share of more than 85% in the total heat rejection. Now, from equation (22), the water temperature at the outlet is 26.1 °C, which is close to the value of 26 °C, reported by the INA fuel refinery [13-14]. It should be noted that the numerical analysis is performed on a cooling tower, which, for convenience, operates with one-sixteenth of the air and water mass flow rates found in the real cooling tower. Therefore, the heat rejection of the cooling tower would be 21.6 MW, when working with the real air and water flow rates. The eight-unit cooling tower system would then achieve a heat rejection of 173 MW.

The efficiency of the cooling tower is determined as the ratio of the range to the approach temperature differences. The range is the difference between water inlet and outlet temperatures, and the approach is the difference between the water inlet and the wet bulb air temperatures. Therefore, the efficiency of the cooling tower is

$$\eta = \frac{t_{w, in} - t_{w, out}}{t_{w, in} - t_{air, wb}} \cdot 100\% \quad (23)$$

The efficiency of the cooling tower is 78.8%, taking into account that the wet bulb temperature of air at the intake is 23 °C. For comparison, the real cooling tower has a declared efficiency of 80%.

3.4 Effect of Operating Parameters

Several operating parameters in the spray nozzles and inside the cooling tower may have a significant influence on the water temperature at the outlet, on the heat rejection and the efficiency of the cooling tower. Some of them, such as the water droplet size, the nozzle spray angle and the water-to-air flow rate ratio are discussed here. In the previous analysis the values of these parameters were as follows: mean droplet diameter of 1.5 mm, water-to-air ratio of 0.824, and nozzle spray angle of 135°. The results obtained with those parameters are referred to as referent values.

The effect of the water-to-air flow rate ratio is studied by changing the air flow rate at the cooling tower intake. Fig. 8 shows that by increasing the air flow rate, the water temperature at the outlet decreases. This means that heat transfer in the cooling tower is enhanced and that heat rejection and efficiency are increased, too. For example, decreasing the water-to-air ratio from the referent value of 0.824 to 0.75 causes an increase in the cooling tower efficiency from 78.8% to 82.1%. This is at the expense of a higher energy consumption in the mechanical fan that now has to move a larger quantity of air.

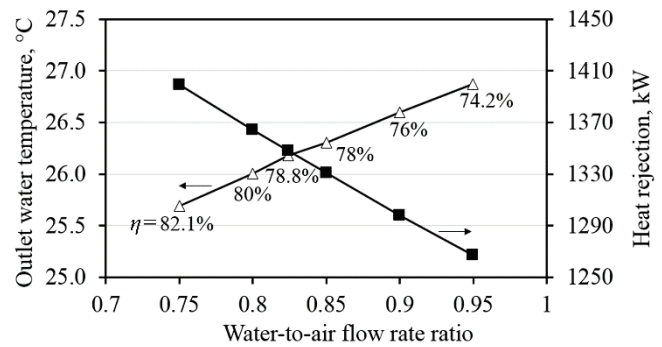


Figure 8 Effect of water-to-air flow rate ratio

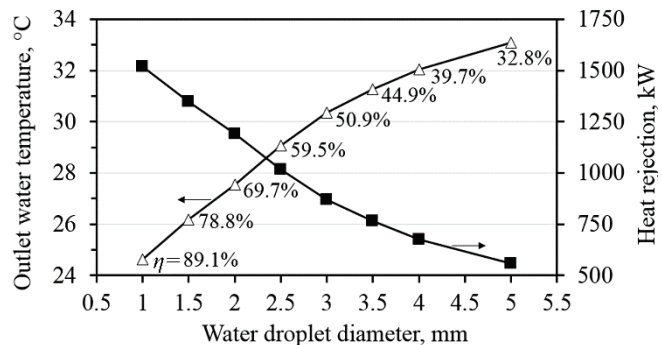


Figure 9 Effect of water droplet diameter

The effect of water droplet size is analyzed by varying the mean diameter of water droplets. As shown in Fig. 9, the water droplet diameter has a dominant influence on the

cooling tower performance. By reducing the size of water droplets, the water temperature at the outlet decreases while the heat rejection and cooling tower efficiency increase.

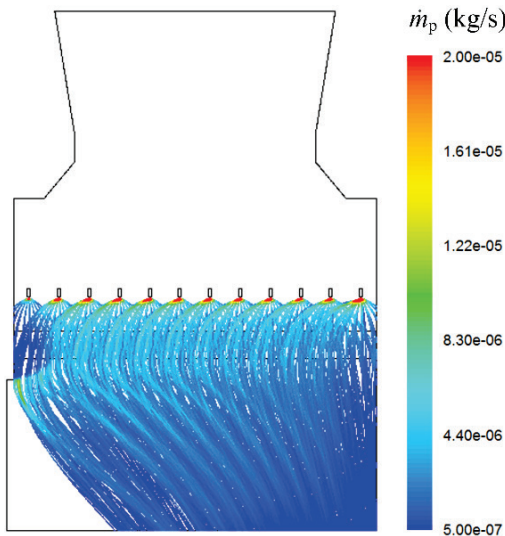


Figure 10 Rate of evaporation for water droplets of 2 mm

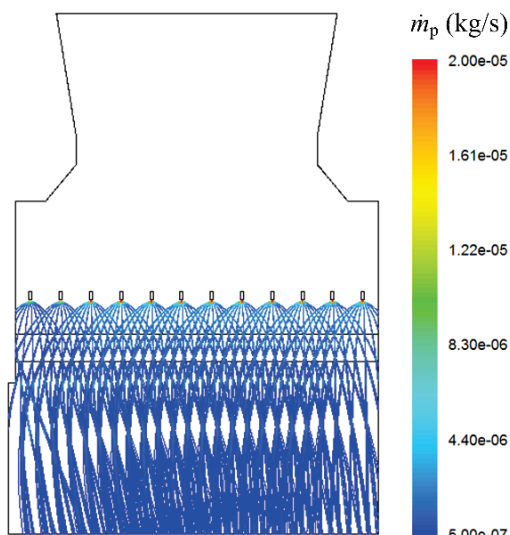


Figure 11 Rate of evaporation for water droplets of 5 mm

Smaller water droplets intensify heat exchange in the cooling tower, especially the latent heat transfer, since the contact surface between water and air is increased. For example, if the diameter of water droplets is halved then the contact surface doubles and the total number of droplets increases eight times for an unchanged water flow rate. The difference in the rate of evaporation arising because of the size of water droplets is shown below. Figs. 10 and 11 show the local rate of evaporation in the cooling tower operating with water droplets having mean diameter of 2 mm and 5 mm, respectively. The local rate of evaporation is higher for the smaller water droplets. The total rate of evaporation is 0.413 kg/s for 2 mm droplets and 0.144 kg/s for 5 mm droplets. The latent heat transfer is 997 kW in the first case and 348 kW in the second case. The cooling tower efficiency

is 69.7% for the smaller droplets and 32.8% for the larger droplets.

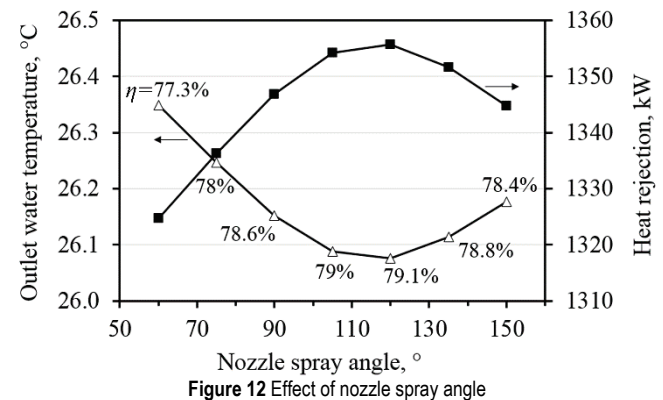


Figure 12 Effect of nozzle spray angle

The effect of the nozzle spray angle is shown in Fig. 12. Unlike the water-to-air ratio and the water droplet size, the spray angle exhibits an optimum value across its range of values. This is noticeable at around 120°, for which heat rejection and the cooling tower efficiency are the greatest. The referent spray angle in this study was 135° and the cooling tower efficiency 78.8%; with a spray angle of 120° the cooling tower would achieve a slightly better efficiency of 79.1%. Narrow spray angles (less than 70°) negatively affect the efficiency of the cooling tower. This is explained by the decreased latent heat transfer, caused by deteriorated mixing between water droplets and air.

4 CONCLUSION

This paper presented a numerical study of heat and mass transfer inside a wet cooling tower with forced air draft. The obtained results include the distribution of air flow velocity, air temperature, specific and relative air humidity, water evaporation rates, and water droplets trajectories inside the cooling tower.

The reference cooling tower performance is obtained for water droplet diameter of 1.5 mm, water-to-air ratio of 0.824 and nozzle spray angle of 135°. In that case the efficiency of the cooling tower is 78.8%. The loss of water due to evaporation is 1.8% in this case. The latent heat transfer is the dominant mode of heat transfer, with a share of 85% in the total heat rejection of the cooling tower.

The size of water droplets affect significantly the latent heat transfer and the total heat rejection. Smaller water droplets mix better with the air flow and increase the total surface for heat and mass transfer. Consequently, the local evaporation rates and the total heat rejection are also increased. For example, the efficiency of the cooling tower is 89.1% for an average droplet diameter of 1 mm. Larger water droplets, on the other hand, decrease the evaporation rates and reduce the cooling tower efficiency. It has been seen that the evaporation rates are highest beneath the water nozzles and along the droplet trajectories. The evaporation rates decrease in the bottom part of the cooling tower as air

humidity increases up to the saturation point. Sensible heat transfer is dominant in the cooling tower filling.

The water-to-air ratio and the nozzle spray angle exhibit weaker effects on the cooling tower efficiency relatively to the water droplet size. The cooling tower efficiency increases with the air flow rate, which reduces the water-to-air ratio. The efficiency is 74.2% for a water-to-air ratio of 0.95, and 82.1% when the water-to-air ratio is 0.75.

The nozzle spray angle has an effect of less than 2% on the cooling tower efficiency, over a wide range of values. The maximum cooling tower efficiency is observed for a spray angle of 120°. Narrow spray angles, on the other hand, deteriorate the mixing between the air stream and water droplets and diminish the cooling tower efficiency.

Future research on this subject should expand the present analysis onto three-dimensional cooling towers, including detailed mathematical models and thorough analysis of the parameters affecting the performance of wet cooling towers.

Acknowledgements

This work has been supported by the Croatian Science Foundation under the project IP-2016-06-4095.

5 REFERENCES

- [1] Kröger, D. (2004). *Air-Cooled Heat Exchangers and Cooling Towers, Thermal-Flow Performance Evaluation and Design*. Vol I, PennWell Corporation, Oklahoma.
- [2] Kröger, D. (2004). *Air-Cooled Heat Exchangers and Cooling Towers, Thermal-Flow Performance Evaluation and Design*. Vol II, PennWell Corporation, Oklahoma.
- [3] Stanford, H. W. (2012). *HVAC Water Chillers and Cooling Towers, Fundamentals, Application and Operation*. CRC Press, Taylor & Francis Group, New York.
- [4] Mungan, I. & Wittek, U. (2004). *Natural Draught Cooling Towers*, Taylor & Francis Group, London, UK.
<https://doi.org/10.1201/b17001>
- [5] Söylemez, M. S. (2004). On the Optimum Performance of Forced Draft Counter Flow Cooling Towers. *Energy Conversion and Management*, 45, 2335-2341.
<https://doi.org/10.1016/j.enconman.2003.11.023>
- [6] Zunaid, M., Murtaza, Q., & Gautam, S. (2017). Energy and Performance Analysis of Multi Droplets Shower Cooling Tower at Different Inlet Water Temperature for Air Cooling Application. *Applied Thermal Engineering*, 121, 1070-1079.
<https://doi.org/10.1016/j.applthermaleng.2017.04.157>
- [7] Bourouni, K., Bassem, M. M., & Chaibi, M. T. (2008). Numerical Study of Coupled Heat and Mass Transfer in Geothermal Water Cooling Tower. *Energy Conversion and Management*, 49, 988-994.
<https://doi.org/10.1016/j.enconman.2007.10.003>
- [8] Jiang, J.-J., Liu, X.-H., & Jiang, Y. (2013). Experimental and Numerical Analysis of a Crossflow Closed Wet Cooling Tower. *Applied Thermal Engineering*, 61, 678-689.
<https://doi.org/10.1016/j.applthermaleng.2013.08.043>
- [9] Goodarzi, M. & Keimanesh, R. (2015). Numerical Analysis on Overall Performance of Savonius Turbines Adjacent to a Natural Draft Cooling Tower. *Energy Conversion and Management*, 99, 41-49.
<https://doi.org/10.1016/j.enconman.2015.04.027>
- [10] Zou, Z. & Gong, H. (2016). Numerical Analysis of Solar Enhanced Natural Draft Dry Cooling Tower Configuration. *Applied Thermal Engineering*, 94, 697-705.
<https://doi.org/10.1016/j.applthermaleng.2015.10.141>
- [11] Smrekar, J., Oman, J., & Širok, B. (2006). Improving the Efficiency of Natural Draft Cooling Towers. *Energy Conversion and Management*, 47, 1086-1100.
<https://doi.org/10.1016/j.enconman.2005.07.012>
- [12] Xia, L., Gurgenci, H., Liu, D., Guan, Z., & Zhou, L. (2016). CFD Analysis of Pre-Cooling Water Spray System in Natural Draft Dry Cooling Towers. *Applied Thermal Engineering*, 105, 1051-1060.
<https://doi.org/10.1016/j.applthermaleng.2016.03.096>
- [13] Šoić, I. (2015). Thermodynamic Analysis of Heat and Mass Transfer in a Cooling Tower, *Master thesis*, Faculty of Engineering, University of Rijeka, Rijeka.
- [14] Šoić, I., Blecich, P., & Franković, B. (October 2016). Termodinamička analiza izmjene topline i prijenos tvari u rashladnom tornju. *Zbornik radova 24. međunarodnog kongresa Energija i okoliš/Proceedings of the 24th International Congress Energy and the Environment*, Opatija, 497-508.
- [15] Versteeg, H. K. & Malalasekera, W. (2007). *An Introduction to Computational Fluid Dynamics: The Finite Volume Method*, 2nd ed., Pearson Education, Essex, UK.
- [16] Ranz, W. E. & Marshall, W. R. (1952). Evaporation from Drops, Part I and Part II. *Chemical Engineering Progress*, 48, 173-180.
- [17] Ergun, S. (1952). Fluid Flow through Packed Columns. *Chemical Engineering Progress*, 48, 89-94.

Authors' contacts:

Paolo BLECICH, PhD, Assistant Professor
Faculty of Engineering, University of Rijeka
Vukovarska 58, HR-51000 Rijeka, Croatia
Tel.: +385 51 651 543, paolo.blecich@riteh.hr

Tomislav SENČIĆ, PhD, Associate Professor
Faculty of Engineering, University of Rijeka
Vukovarska 58, HR-51000 Rijeka, Croatia
Tel.: +385 51 651 515, tomislav.sencic@riteh.hr

Igor WOLF, PhD, Associate Professor
Faculty of Engineering, University of Rijeka
Vukovarska 58, HR-51000 Rijeka, Croatia
Tel.: +385 51 651 510, igor.wolf@riteh.hr

Igor BONEFAČIĆ, PhD, Assistant Professor
Faculty of Engineering, University of Rijeka
Vukovarska 58, HR-51000 Rijeka, Croatia
Tel.: +385 51 651 561, igor.bonefacic@riteh.hr

ALTERNATIVE CONTROLLER DESIGN FOR ROTARY INVERTED PENDULUM

Mehmet ÖKSÜZ, Mehmet Burak ÖNAL, Recep HALICIOĞLU, Lale Canan DÜLGER

Abstract: The inverted pendulum has been considered a classical control problem. Two designs of inverted pendulum are planar and rotary with a nonlinear unstable system characteristic. Inverted pendulum systems are nonlinear. They can be used for testing and studying various observers and controllers. Control of a rotary inverted pendulum is studied here. This paper proposes stabilization of the rotary inverted pendulum at its upright position by using full-state controller. Full-state controllers are designed by using different damping ratios. MATLAB simulation results and the experimental results are taken for 10 degrees step for 5 seconds. The best controller is chosen for SRV02-Rotary inverted pendulum by looking at the simulation and experimental results.

Keywords: controller design; full-state controller; linearization; pole placement; rotary inverted pendulum (RIP); stabilization

1 INTRODUCTION

Inverted pendulum systems are treated as underactuated mechanical systems. Different control algorithms are applied for solving swing-up control and stabilization problem. The equations of motion are nonlinear. This makes the inverted pendulum problem one of the favorite topics for control problem. Therefore, they can be linearized at an operating point to carry out proper solution.

Many studies are found in the area of control issues related to inverted pendulum systems. Some of the studies dealing with inverted pendulum control are summarized herein. Yan [1] developed a tracking control law for underactuated RIP by applying nonlinear back stepping, differential flatness, and small gain theorem. Mirsaeid and Zarei [2] presented a mechatronic system case study on adaptive modeling and control of an inverted pendulum. Hassanzadeh et al. [3] presented an optimum Input-Output Feedback Linearization (IOFL) cascade controller. Genetic Algorithm (GA) was applied for the inner loop with PD controller forming the outer loop for balancing the pendulum in an inverted position. The control criterion was to minimize the Integral Absolute Error (IAE) of the system angles. The optimal controller parameters are found by minimizing the objective function related to IAE using Binary Genetic Algorithm (BGA). Ozbek and Efe [4] focused on the swing up and stabilization control of a rotary inverted pendulum (RIP) system with linear quadratic regulator (LQR). Sliding Mode Control (SMC) is based on hard boundary switching law and fuzzy logic control (FLC). Akhtaruzzaman et al. [5] have described different controller designs for rotary pendulum. Experimental and MATLAB based simulation results are given. Hassanzadeh et al. [6] also studied control by using evolutionary approaches. GA, Particle Swarm Optimization (PSO) and Ant Colony Optimization (ACO) are used for designing the rotational inverted pendulum. Quyen et al. [7] presented the dynamic model of RIP. ANN controller is used for controlling the system.

Jadlovská and Sarnovsky [8] have revealed an approach for the control of the rotary single inverted pendulum system. State feedback control techniques are used as pole placement and the LQR optimal control. Mathew et al. [9] performed a study on swing up and stabilization control of a RIP system. Two control schemes are performed for stabilization as LQR and SMC. Chen and Huang [10] have proposed an adaptive controller for RIP with time-varying uncertainties to bring the pendulum close to the upright position regardless of the various uncertainties and disturbances. Its underactuated dynamics was first decoupled by Olfati's transformation into a cascade form. Oltean [11] has proposed solution for swing up and stabilization of RIP using PD and fuzzy PD controllers. The models are performed in MATLAB/Simulink environment. Ding and Li [12] have proposed a cascade fuzzy controller based on Mamdani for the outer loop and Sugeno for the inner loop. The simulation graphs are performed with Simulink. Dang et al. [13] have designed a robust Takagi-Sugeno (T-S) fuzzy descriptor approach for a stabilizing controller for the RIP with real-time implementation. Chandran et al. [14] derived the nonlinear dynamics of the RIP. Artificial neural network (ANN) is applied to identify the model.

This study presents nonlinear and linearized model of the RIP. Four full-state controllers are designed by using MATLAB for the system stabilizing for linear dynamic model. The results of four controllers are compared. The best controller is chosen for SRV02.

2 ROTARY INVERTED PENDULUM

The experimental setup is in downright position, which is unstable. It consists of PC (1), data acquisition system (2), rotary inverted pendulum (3), and amplifier (4), shown in Fig. 1. The expected upright position of the pendulum after applying controller is shown in Fig. 2.

Fig. 3 presents the rotary inverted pendulum's schematic representation in x - y - z coordinates. The rotary arm pivot is attached to the SRV02 system. The pendulum is connected to the end of the arm by using a revolute joint. The arm

length, the arm angle, the pendulum length, and the pendulum angle are denoted by L_r , θ , L_p , and α , respectively. The arm has a mass of m_r , and the pendulum has m_p . The mass moment of inertia for the arm and the pendulum are J_r and J_p , respectively.

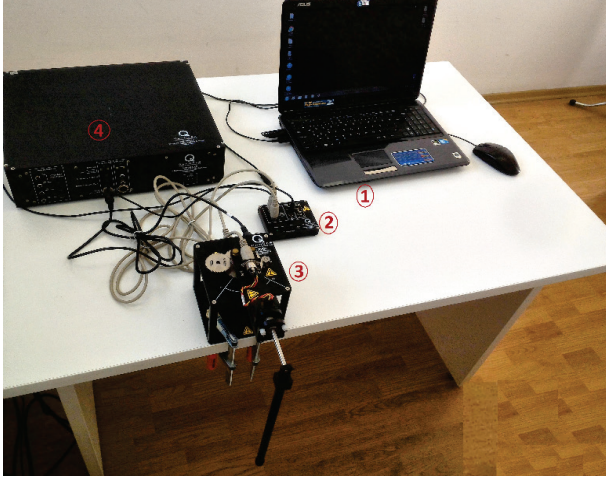


Figure 1 Experimental setup in downright position

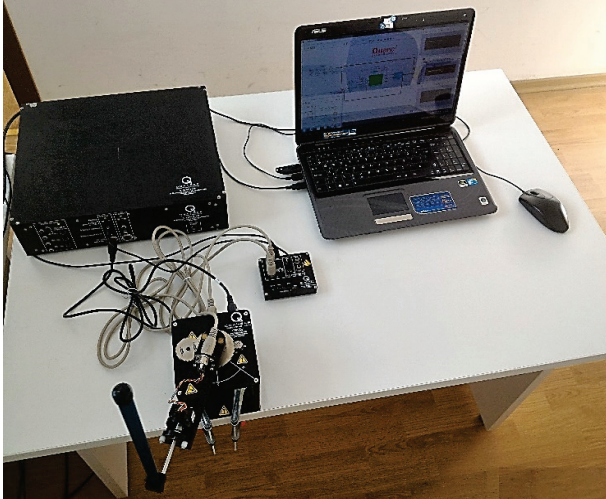


Figure 2 Expected position of the pendulum after applying the controller

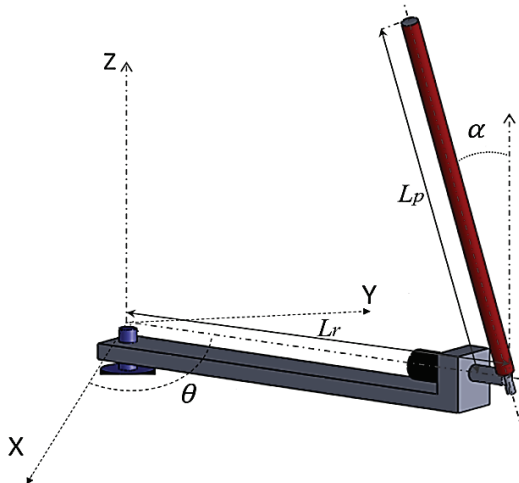


Figure 3 Schematic Representation of RIP

Parameters of the SRV02 motor and the rotary inverted pendulum are given with their values and units in Tab. 1. These parameters are then used while performing simulation from the mathematical model of the system [15].

Table 1 Technical specifications of the SRV02 and rotary inverted pendulum [15]

Parameters	Symbols	Values	Units
Gearbox efficiency	η_g	0.9	-
Motor efficiency	η_m	0.69	-
Motor torque constant	k_t	0.007683	N·m/A
Total gear ratio	K_g	70	-
Motor back-EMF constant	k_m	0.0076777	V·s/rad
Motor armature resistance	R_m	2.6	Ω
Pendulum mass	m_p	0.127	kg
Arm full length	L_r	0.2159	m
Pendulum full length	L_p	0.33655	m
Arm moment of inertia	J_r	0.0009983	kg·m ²
Pendulum moment of inertia	J_p	0.0012	kg·m ²
Equivalent arm viscous damping coefficient	B_r	0.0024	N·m·s/rad
Equivalent pendulum viscous damping coefficient	B_p	0.0024	N·m·s/rad
Gravity	g	9.81	kg·m ²

3 MATHEMATICAL MODEL OF THE RIP

The dynamic model of the rotary inverted pendulum is derived by using the Lagrangian ($L = T - V$) based on energy expressions with respect to variables [16, 17]. Independent generalized coordinates for this problem are α and θ . T is the sum of the rotary arm kinetic energy T_{arm} and the pendulum's kinetic energy T_{pend} is given in Eq. (1). V is the sum of the rotary inverted pendulum potential energy, which includes only pendulum's potential energy, it is given in Eq. (2).

$$T = T_{\text{pend}} + T_{\text{arm}} = \frac{1}{2} m_p \dot{P}^2 + \frac{1}{2} J_p \dot{\alpha}^2 + \frac{1}{2} J_r \dot{\theta}^2 \quad (1)$$

$$V = \frac{1}{2} m_p g L_p \cos \alpha \quad (2)$$

To attain velocity of the center of the pendulum, the coordinates of the center of mass of the pendulum are determined in Eq. (3) to Eq. (5).

$$P_x = L_r \cos \theta + \frac{1}{2} L_p \sin \alpha \sin \theta \quad (3)$$

$$P_y = L_r \sin \theta - \frac{1}{2} L_p \sin \alpha \cos \theta \quad (4)$$

$$P_z = \frac{1}{2} L_p \cos \alpha \quad (5)$$

By taking derivatives of the positions, the velocity of point P is found. Lagrange equation becomes as Eq. (6).

$$L = \frac{1}{2} \left(J_r + m_p L_r^2 + \frac{1}{4} m_p L_p^2 \sin^2 \alpha \right) \dot{\theta}^2 + \frac{1}{2} \left(J_p + \frac{1}{4} m_p L_p^2 \right) \dot{\alpha}^2 - \frac{1}{2} m_p L_r L_p \cos \alpha \dot{\theta} \dot{\alpha} - \frac{1}{2} m_p g L_p \cos \alpha \quad (6)$$

The system dynamic model is resulted in Eq. (7) and Eq. (8). Here τ is the applied torque, B_r is the viscous friction coefficient of the torque, and B_p is the viscous damping coefficient of the pendulum. Torque based on the rotary arm is generated by a servo motor. It is defined in Eq. (9) where η_g , η_m , K_g , R_m , k_t and V_m are the efficiency of gear, the efficiency of motor, the gear ratio, the motor armature resistance, the motor current, the torque constant and the input motor voltage, respectively [16, 17].

$$\ddot{\theta} \left(J_r + m_p L_r^2 + \frac{1}{4} m_p L_p^2 \sin^2 \alpha \right) + \ddot{\alpha} \left(-\frac{1}{2} m_p L_r L_p \cos \alpha \right) + \dot{\theta} \dot{\alpha} \left(\frac{1}{2} m_p L_p^2 \sin \alpha \cos \alpha \right) + \dot{\alpha}^2 \left(\frac{1}{2} m_p L_r L_p \sin \alpha \right) = \tau - B_r \dot{\theta} \quad (7)$$

$$\ddot{\theta} \left(-\frac{1}{2} m_p L_r L_p \cos \alpha \right) + \ddot{\alpha} \left(J_p + \frac{1}{4} m_p L_p^2 \right) + \dot{\theta}^2 \left(-\frac{1}{4} m_p L_p^2 \sin \alpha \cos \alpha \right) - \frac{1}{2} m_p g L_p \sin \alpha = -B_p \dot{\alpha} \quad (8)$$

$$\tau = \frac{\eta_g \eta_m K_g k_t (V_m - K_g k_m \dot{\theta})}{R_m} \quad (9)$$

For a generalized coordinate, vector q , can be generalized into the matrix form as Eq. (10) in which D is the inertial matrix, C is the damping matrix and $g(q)$ is the gravitational vector.

$$\ddot{q}D(q) + \dot{q}C(q, \dot{q}) + g(q) = \tau \quad (10)$$

Eq. (7) and Eq. (8) are nonlinear equations. They are to be linearized at the zero initial conditions as $[\theta \ \alpha \ \dot{\theta} \ \dot{\alpha} \ \ddot{\theta} \ \ddot{\alpha}]^T = [0 \ 0 \ 0 \ 0 \ 0 \ 0]^T$. The resultant mathematical model of the inverted pendulum is defined as matrix form in Eq. (11).

$$\begin{bmatrix} \tau \\ 0 \end{bmatrix} = \begin{bmatrix} J_r + m_p L_r^2 & -\frac{1}{2} m_p L_r L_p \\ -\frac{1}{2} m_p L_r L_p & J_p + \frac{1}{4} m_p L_p^2 \end{bmatrix} \begin{bmatrix} \ddot{\theta} \\ \ddot{\alpha} \end{bmatrix} + \begin{bmatrix} B_r & 0 \\ 0 & B_p \end{bmatrix} \begin{bmatrix} \dot{\theta} \\ \dot{\alpha} \end{bmatrix} + \begin{bmatrix} 0 & 0 \\ 0 & -\frac{1}{2} m_p g L_p \end{bmatrix} \begin{bmatrix} \theta \\ \alpha \end{bmatrix} \quad (11)$$

The equation for the angular acceleration of arm $\ddot{\theta}$, and the angular acceleration of pendulum $\ddot{\alpha}$ should be determined by using Eq. (11). The equations can be simplified by defining a constant gain G in Eq. (12).

$$G = \frac{1}{\left(J_r + m_p L_r^2 \right) \left(J_p + \frac{1}{4} m_p L_p^2 \right) - \frac{1}{4} m_p^2 L_r^2 L_p^2} \quad (12)$$

The rotary inverted pendulum has two coordinates for description. Two second order equations; thus it has four state variables where: $X_1 = \theta$, $X_2 = \alpha$, $X_3 = \dot{\theta}$ and $X_4 = \dot{\alpha}$. The general state space equations are given in Eq. (13) [15] where; A is the state matrix that gives information about characteristic of the system; B is the input-to-state matrix; C is the state-to-output matrix; and D is the feed through matrix.

$$\dot{x} = Ax + Bu \quad \text{and} \quad y = Cx + Du \quad (13)$$

4 DESIGN OF A CONTROLLER - POLE PLACEMENT

A linear dynamic system in the state space form is given in Eq. (13) where; $D = 0$. To stabilize the system to improve its response, full state feedback is $u = -Kx$. The closed loop system is given in Eq. (14). The main purpose of the state feedback control is to stabilize the system. Thus, all closed loop poles should be located in the left-hand of the complex plane.

$$\dot{x} = (A - BK)x \quad \text{and} \quad y = Cx \quad (14)$$

4.1 The System Poles

The system poles give information on the system characteristic. Tab. 2 shows the state-space representation matrices of the system. To define the poles of the system $\det(SI - A) = 0$ is estimated. The poles of the system are found as: $p_1 = 0$, $p_2 = -32.39$, $p_3 = 7.32$ and $p_4 = -5.15$.

The system was expected to be unstable because when the inverted pendulum is kept in an upright position, a small perturbation will remove the inverted pendulum from the stable position. The inverted pendulum will not return back to the upright position. The system is not stable since one of the poles is in the right-hand plane. The pole or poles which are located in the right-hand plane should be transferred in the left-hand plane to provide the stability of the system [11].

Table 2 State-Space matrix equations and their results

A	$\begin{bmatrix} 0 & 0 & 1 & 0 \\ 0 & 0 & 0 & 1 \\ 0 & \frac{1}{4}Gm^2gL_rL_p^2 & -GB_r\left(J_p + \frac{1}{4}mL_p^2\right) & -\frac{1}{2}GmL_pL_rB_r \\ 0 & \frac{1}{2}GmgL_p\left(J_r + mL_r^2\right) & -\frac{1}{2}GmL_pL_rB_r & -GB_p\left(J_r + mL_r^2\right) \end{bmatrix}$	$\begin{bmatrix} 0 & 0 & 1 & 0 \\ 0 & 0 & 0 & 1 \\ 0 & 81.34 & -28.81 & -0.93 \\ 0 & 121.96 & -28.18 & -1.40 \end{bmatrix}$
B	$\begin{bmatrix} 0 \\ 0 \\ G\left(J_p + \frac{1}{4}mL_p^2\right) \\ \frac{1}{2}GmL_pL_r \end{bmatrix}$	$\begin{bmatrix} 0 \\ 0 \\ 51.81 \\ 49.84 \end{bmatrix}$
C	$\begin{bmatrix} 1 & 0 & 0 & 0 \\ 0 & 1 & 0 & 0 \end{bmatrix}$	$\begin{bmatrix} 1 & 0 & 0 & 0 \\ 0 & 1 & 0 & 0 \end{bmatrix}$
D	$\begin{bmatrix} 0 \\ 0 \end{bmatrix}$	$\begin{bmatrix} 0 \\ 0 \end{bmatrix}$

4.2 The Desired Poles

There are four eigenvalues of the system. Two of them are specified as follows: $p_1 = -\delta w_n + jw_d$ and $p_2 = -\delta w_n - jw_d$. They are the complex conjugate dominant poles, where δ is the damping ratio, w_n is the natural frequency, and the other poles p_3 and p_4 are defined at -30 and -40 , as shown in Fig. 4.

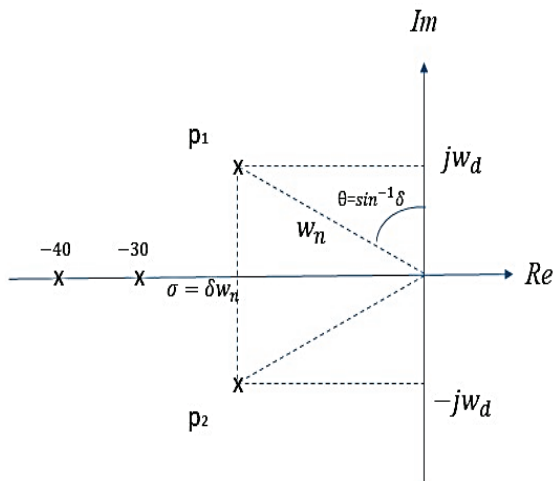

Figure 4 Desired poles in complex plane

Table 3 Desired poles for different damping ratios

No	Damping ratio δ	dp_1	dp_2	dp_3	dp_4
1	0.7	$-2.8 + 2.86j$	$-2.8 - 2.86j$	-30	-40
2	0.75	$-3 + 2.64j$	$-3 - 2.64j$	-30	-40
3	0.8	$-3.2 + 2.4j$	$-3.2 - 2.4j$	-30	-40
4	0.85	$-3.4 + 2.11j$	$-3.4 - 2.11j$	-30	-40

The natural frequency is taken $w_n = 4$ rad/s [15], and four values of damping ratios are used. The desired poles are

found according to the damping ratios introduced. The required systems are given with their poles in Tab. 3.

4.3 Full-State Controller Coefficient – Pole Placement

The controllability of the system should be checked to decide whether the system can be controlled by full-state controller or not. If A and B matrices of the state-space model are controllable, the system can be controlled by the pole placement method with full-state control gains. The controllability matrix of the system is determined by $M = [B \ AB \ A^2B \ \dots \ A^{n-1}B]$ and the rank of M is four. The system is controllable with 4 states.

The general equation form of the open loop characteristic equation is given in Eq. (15) and companion matrices of A and B should be estimated in z-plane. They can be denoted by A_z and B_z as given in Eq. (16) and the controllability matrix of the companion $M_z = [B_z \ A_zB_z \ A_z^2B_z \ \dots \ A_z^{n-1}B_z]$ could be accounted.

$$s^4 + a_3s^3 + a_2s^2 + a_1s^1 + a_0 \quad (15)$$

$$A_z = \begin{bmatrix} 0 & 1 & 0 & 0 \\ 0 & 0 & 1 & 0 \\ 0 & 0 & 0 & 1 \\ -a_0 & -a_1 & -a_2 & -a_3 \end{bmatrix}, \quad B_z = \begin{bmatrix} 0 \\ 0 \\ 0 \\ 1 \end{bmatrix} \quad (16)$$

Control gain in z-plane, K_z , should be computed to assign the poles of $A_z - B_zK_z$ to required places. The closed loop equation form for desired poles is given in Eq. (17) and $K_z = [K_{z1} \ K_{z2} \ K_{z3} \ K_{z4}]$. Calculations are given in Eq. (18).

$$(s - dp_1)(s - dp_2)(s - dp_3)(s - dp_4) = s^4 + a_{d3}s^3 + a_{d2}s^2 + a_{d1}s^1 + a_{d0} \tag{17}$$

$$\begin{bmatrix} 0 & 1 & 0 & 0 \\ 0 & 0 & 1 & 0 \\ 0 & 0 & 0 & 1 \\ -a_0 - k_{z1} & -a_1 - k_{z2} & -a_2 - k_{z3} & -a_3 - k_{z4} \end{bmatrix} = \begin{bmatrix} 0 & 1 & 0 & 0 \\ 0 & 0 & 1 & 0 \\ 0 & 0 & 0 & 1 \\ -a_{d0} & -a_{d1} & -a_{d2} & -a_{d3} \end{bmatrix}, K_z^T = \begin{bmatrix} a_{d0} - a_0 \\ a_{d1} - a_1 \\ a_{d2} - a_2 \\ a_{d3} - a_3 \end{bmatrix} \tag{18}$$

The transformation matrix, Z should be calculated by multiplication of controllability and inverse controllability of the companion, $Z = M \cdot M_z^{-1}$. Finally, the control gain from z-plane should be transformed to actual plane control gain.

The system poles are located in the desired poles by estimating the control gain, $K = K_z Z^{-1} = [K_1 \ K_2 \ K_3 \ K_4]$, where K is the control gain. Four controllers are designed using different damping ratios. The control gains for using ratios are given in Tab. 4.

Table 4 Controllers for different damping ratios

Controllers No	Damping ratio δ	K_1	K_2	K_3	K_4
1	0.7	-8.47	48.36	-4.36	5.70
2	0.75	-8.47	49.16	-4.83	5.94
3	0.8	-8.47	49.95	-5.05	6.18
4	0.85	-8.47	50.74	-5.27	6.41

5 THEORETICAL AND EXPERIMENTAL RESULTS

The system Simulink model and the system real model are created in MATLAB/Simulink program. The block diagram of the simulation model is presented in Fig. 5.

Then the encoders are read in the plant block by using Simulink Real-Time™. It is given as the real system block diagram in Fig. 6.

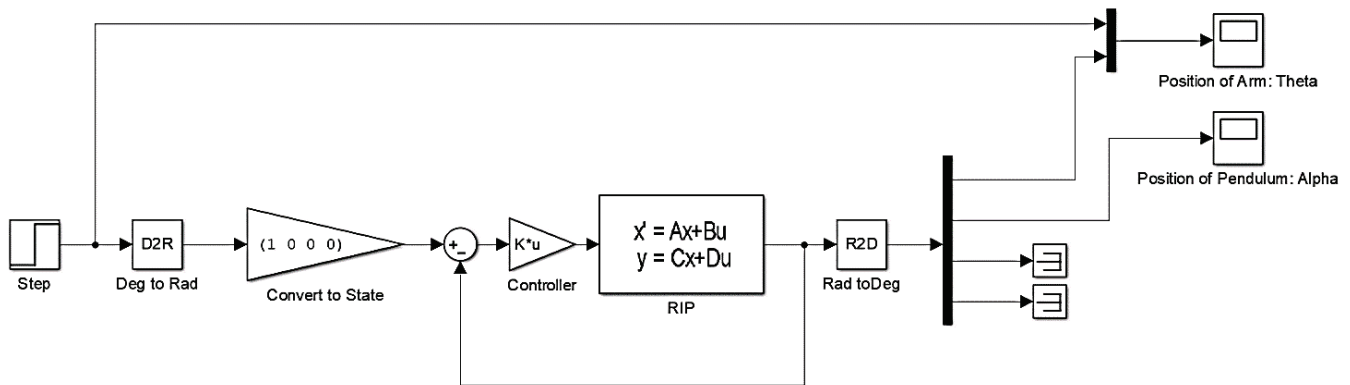


Figure 5 The system simulation block diagram

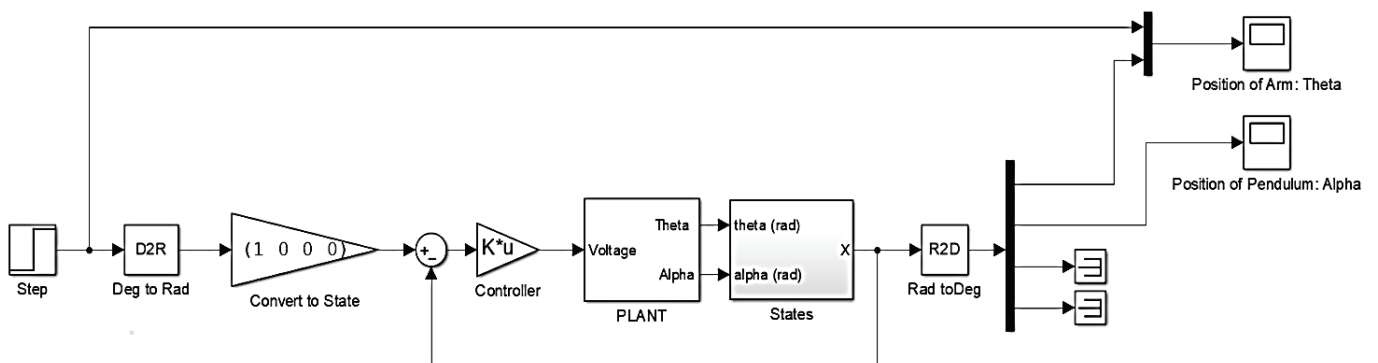


Figure 6 The real system block diagram

A step input of 10 degrees for the angular position of arm is applied for 5 seconds. The arm positions and the pendulum positions are taken and presented for all controllers in Fig. 7 and Fig. 8. A comparison is made between them. All designed controllers stabilize the pendulum at its up-right position. It shows that the system is quite stable for all controllers. The 3rd and 4th controllers have given better responses. The fastest response, minimum overshoot and the

steady state errors are seen. 10 degrees of a step input is applied to the arm of the rotary inverted pendulum for 5 seconds. The experimental results are taken by encoders which can read the arm and the pendulum positions of the system. Fig. 9 and Fig. 10 show actual positions of the arm and the pendulum.

The 4th controller is given the best system to hold the pendulum at its up-right position. Finally, it can be said that

$\delta = 0.85$ of damping ratio with $w_n = 4$ rad/s of the natural frequency is better to use for the SRV02 rotary inverted pendulum system.

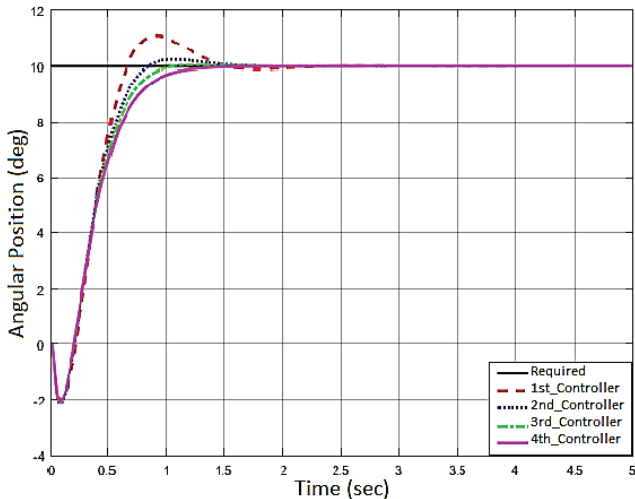


Figure 7 Simulation results of the arm angular position θ

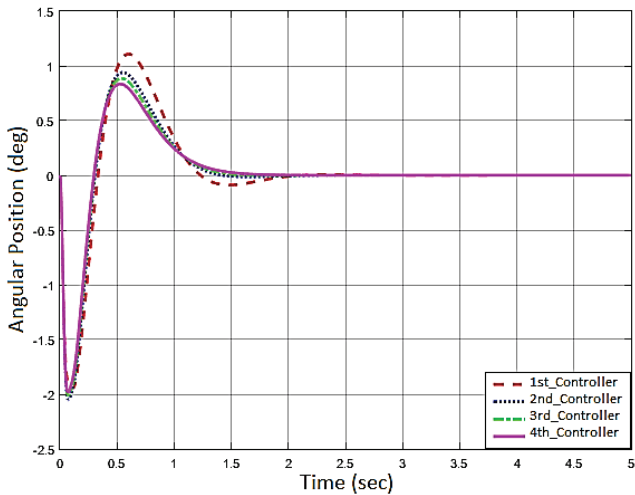


Figure 8 Simulation results of the pendulum angular position α

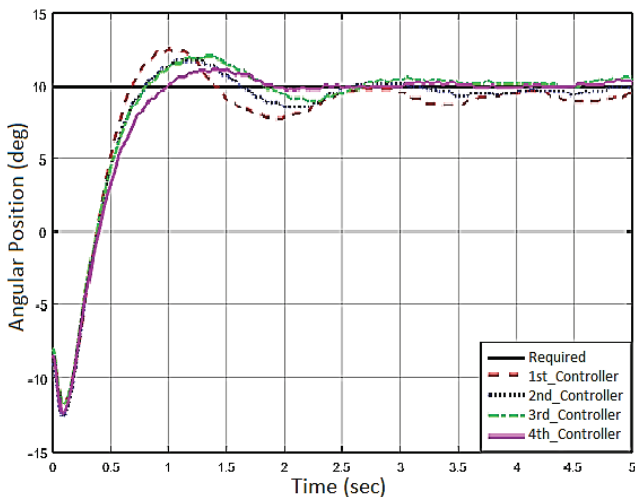


Figure 9 Experimental results of the arm angular position θ

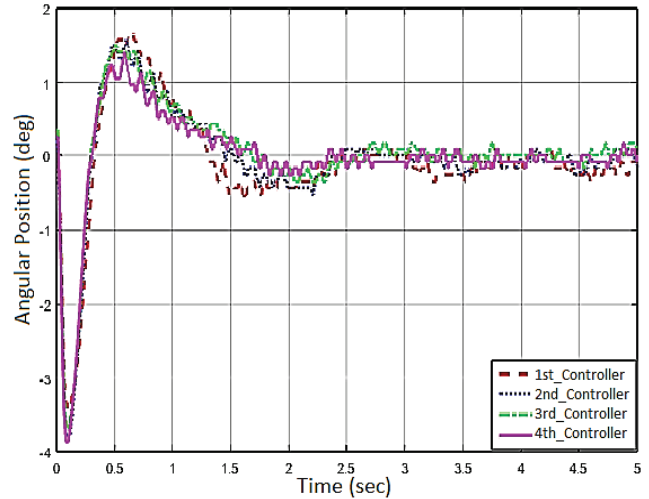


Figure 10 Experimental results of the pendulum angular position α

6 CONCLUSIONS

Inverted pendulum system has a great role in real application of engineering fields. Thus, companies in industry and researches have studied the inverted pendulum. In this study, the SRV02 rotary inverted pendulum is studied with controllers which have different damping ratios. Experiments have been performed in Mechatronics Laboratory, Turkish Aeronautical Association University Mechatronics Engineering Department. Having dynamic models of the rotary inverted pendulum, four controllers are designed. $\delta = 0.8$ and $\delta = 0.85$ of damping ratios show better responses than the other controllers. The experimental results for 5 seconds with a 10-degree step input are obtained for all designed controllers. The 4th controller which has $\delta = 0.85$ of damping ratio with $w_n = 4$ rad/s is the best controller. The pendulum is held at upright position.

7 REFERENCES

- [1] Yan, Q., (2003). Output tracking of underactuated rotary inverted pendulum by nonlinear controller. *Decision and Control. Proceedings. 42nd IEEE Conf.*, 2395-2400.
- [2] Mirsaeid Ghazi S. S. & Zarei A. (2007). A Mechatronic System Design Case Study: Adaptive Modeling and Control of an Inverted Pendulum. *IEEE Int Conf on Networking, Sensing and Control*, London, 291-296. <https://doi.org/10.1109/ICNSC.2007.372793>
- [3] Hassanzadeh, I., Mobayen, S., & Harifi, A. (2008). Input-output feedback linearization cascade controller using genetic algorithm for rotary inverted pendulum system. *American Journal of Applied Sciences*, 5(10), 1322-1328. <https://doi.org/10.3844/ajassp.2008.1322.1328>
- [4] Özbek, N.S. & Efe, M. Ö. (2010). Swing up and stabilization control experiments for a rotary inverted pendulum—An educational comparison. *IEEE International Conference on Systems Man and Cybernetics (SMC)*, 2226-2231. <https://doi.org/10.1109/ICSMC.2010.5641962>
- [5] Akhtaruzzaman MD., Shafie A.A., (2010). Modeling and Control of a Rotary Inverted Pendulum using Various Methods, Comparative Assessment and Result Analysis. *Pr. of the IEEE Int. Conf. on Mechatronics and Automation*, 1342-1347. <https://doi.org/10.1109/ICMA.2010.5589450>

- [6] Quyen, N. D., Thuyen, N. V., Nguyen, Q. H., & Nguyen, D. H. (2012). Rotary Inverted Pendulum and Control of rotary Inverted Pendulum by Artificial Neural Network. *Proc. Natl. Conf. Theory Phys.*, 37, 243-249.
- [7] Mathew, N. J., Rao K. K., & Sivakumaran N. (2013). Swing up and Stabilization Control of a Rotary Inverted Pendulum. *10th IFAC Int. Symp. on Dynamics and Control of Process Systems*, Dec. 18-20, Mumbai / India, 654-659.
<https://doi.org/10.3182/20131218-3-IN-2045.00128>
- [8] Jadlovska, S. & Sarnovsky, J. (2013). A Complex Overview of modeling and control of the rotary single inverted pendulum system. *Power Eng and El. Eng.*, 11(2), 73-85.
<https://doi.org/10.15598/aece.v11i2.773>
- [9] Chen, Y-F. & Huang, A-C. (2014). Adaptive control of rotary inverted pendulum system with time-varying uncertainties. *Nonlinear Dynamics*, 76(1), 95-102.
<https://doi.org/10.1007/s11071-013-1112-4>
- [10] Oltean, S. E. (2014). Swing up and stabilization of the rotary inverted pendulum using PD and fuzzy-PD Controllers. *INTER-ENG 2013, Procedia Technology*, 12, 57-64.
<https://doi.org/10.1016/j.protcy.2013.12.456>
- [11] Ding, Z. & Li, Z. (2014). A Cascade Fuzzy Control System for Inverted Pendulum based on Mamdani-Sugeno Type. *IEEE 9th Conf. on Ind. Electronics and Apps (ICIEA)*, 792-797.
<https://doi.org/10.1109/ICIEA.2014.6931270>
- [12] Dang, Q. V., Allouche, B., Vermeiren, L., Dequidt, A., & Dambrine, M. (2014). Design and implementation of a robust fuzzy controller for a rotary inverted pendulum using the Takagi-Sugeno descriptor representation. *IEEE Symp. on Comp. Intelligence in Control and Automation (CICA2014)*, 1-6. <https://doi.org/10.1109/CICA.2014.7013249>
- [13] Chandran, D., Krishna, B., George, V., & Thirunavukkarasu, I. (2015). Model identification of rotary inverted pendulum using artificial neural networks. *IEEE Int. Conf. on Recent Developments in Control, Automation and Power Engineering (RDCAPE2015)*, 146-150.
<https://doi.org/10.1109/RDCAPE.2015.7281385>
- [14] Quanser 2014 Modeling Documentation: *QUBE-Servo Rotary Inverted Pendulum Modeling*. http://www.quanser.com/courseware/qubeservo_matlab/?P=307 (2014). Accessed January 2017.
- [15] Ogata, K. (2010). *Modern Control Engineering*. 5th Edition, Pearson.
- [16] Ginsberg, J. (2008). *Engineering Dynamics*. Cambridge University Press.

Authors' contacts:**Mehmet ÖKSÜZ****Mehmet Burak ÖNAL**

Turkish Aeronautical Association University,
Mechatronics Engineering Department,
Etimesgut, 06790, Ankara, Turkey
mehmet.oksuz@thk.edu.tr

Recep HALICIOĞLU, PhD

Researcher
rhaliocioglu@gmail.com

L. Canan DÜLGER, PhD, Professor

Corresponding Author
İzmir University of Economics
Mechanical Engineering Department
+902324888557, lalecanandulger@gmail.com (After September 2018)
[canan.dulger@ieu.edu.tr](mailto:(canan.dulger@ieu.edu.tr))

THE EFFECT OF BIOMATERIAL SELECTION ON THE STATIC STRENGTH OF FEMUR PROSTHESIS

Saim KURAL, Safiye İPEK AYVAZ

Abstract: Throughout the history, biomaterials have been widely used for replacing damaged human organs. Biocompatibility is generally defined as the harmony of the biomaterials with human body physically, chemically and biologically. Mechanical strength properties are of great importance in biocompatibility of the biomaterials which are used as orthosis and prosthesis in skeletal system. In this study, static analyses of femur implants which were modelled by using 316 stainless steel and Ti6Al4V titanium alloy, were carried out under three different axial forces (500, 750 and 1000 N). As a result of the analyses made, the effect of material selection on the biomechanical and biocompatibility properties of femoral implants was determined.

Keywords: biocompatibility; biomaterials; biomechanical; femur Implant; Finite Element Analysis

1 INTRODUCTION

Some of the innate causes or the resulting health problems may result in the loss of the function of human living tissues and organs, partially or completely. To recover the lost functions, the living tissues are replaced with implanted materials called biomaterial [1]. Biocompatibility includes definitions of the biocompatibility of implanted biomaterials with respect to their mechanical, physical, and chemical properties, and biocompatibility to surrounding tissues [2]. Biocompatibility of biomaterials is determined by many test results.

The human body has pH values ranging from 1 to 9. Therefore, the material to be used should not be exposed to corrosion by surrounding tissues and body fluids. If biomaterials are corroded or physically eroded, biomaterial breakdown particles can pass into human plasma, causing significant health problems such as ulcers, anemia and even Alzheimer's disease [3]. It is therefore important that the chemical and physical abrasion resistance of the material is well defined [3-6]. In addition, the biomaterial used should not have toxic effects on or cause infection of the living tissue around it and should not adversely affect vital activities of the tissue. To determine this biocompatibility feature, in-vitro tests are used to examine the effect of biomaterials on vital activities of prepared cell cultures. Another method used is in-vivo testing of biomaterials implanted in guinea pigs [7, 8].

The human femur thighbone is the heaviest, longest, and most durable bone in the human body [9, 10]. Femur fractures are a common occurrence. In the United States alone, 6.5 million people are reported to have broken or injured their femur because of traffic accidents every year. [11]. Mechanical strengths and designs are especially important in the biocompatibility of implants used in skeletal systems such as femur prosthesis. The inclination angle between the head and the body of the prosthesis is especially important in the design of the femoral prosthesis. In some studies, the effect of the angle on the static strength of the

prosthesis has been investigated. However, it is known that Coxa Valga occurs when the natural inclination angle of the femur bone is about 130° and the angle is larger than 130°, while Coxa Vara disorders occur when it is smaller [12-14].

Studies show that most of the human weight is carried by the femurs and that the load applied to the femurs is increasing by walking and running [9, 15]. The mechanical strength of the prosthetic material used to carry these loads must be good. The most commonly used metallic biomaterials in femurs and other skeletal system implant applications are CoCr alloys, 316 stainless steel alloys and Ti6Al4V titanium alloys [16-19].

In this study, the biomechanical biocompatibility of the femoral prosthesis modeled using 316 stainless steel and Ti6Al4V titanium alloy under different patient weight conditions (500, 750 and 1000 N) was evaluated and determined.

2 MODELING AND FINITE ELEMENT ANALYSIS

In this study, mechanical behaviors of human femoral prosthesis patients at different weights were examined by modelling with ANSYS® software using 500, 750 and 1000 N loads. 316L stainless steel alloy and Ti6Al4V titanium alloy, the physical and mechanical properties of which are shown in Tab. 1, were selected as femoral prosthesis materials.

Table 1 Physical and mechanical properties of Ti6Al4v and 316l alloys

Material	Density (kg/m ³)	Poisson ratio	Elasticity module (GPa)	Yield strength (MPa)
Ti6Al4V	4.43	0.342	114	883
316L	7.99	0.33	200	300

Fig. 1 shows the geometry and mesh structure of the prosthesis analyzed. In the femoral prosthesis, the mesh structure is thinned by applying a regional mesh to the head and neck which is critical to the load angle. In total 199,196 nodes and 131,665 elements were used. Supported boundary conditions are entered by applying "fixed support" to the

body part of the prosthesis in the bone. 500, 750 and 1000 N loads were applied to the head of the prosthesis in contact with the pelvic bone (Fig. 2). As a result of static analysis, total deformation and Von-Mises equivalent stresses were determined and evaluated.

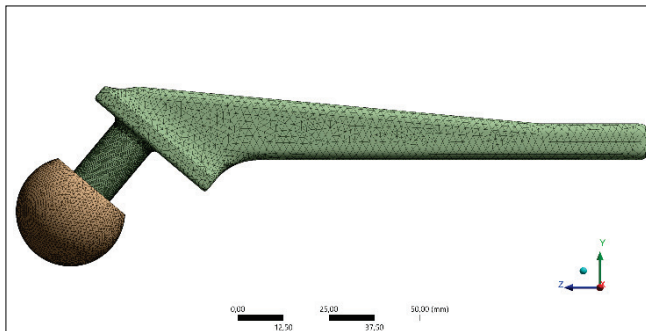


Figure 1 Geometry and mesh structure of femur prosthesis

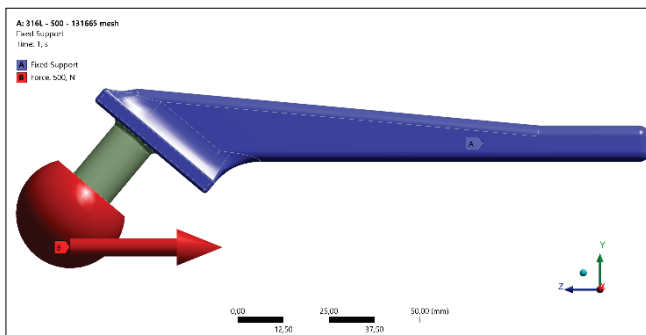


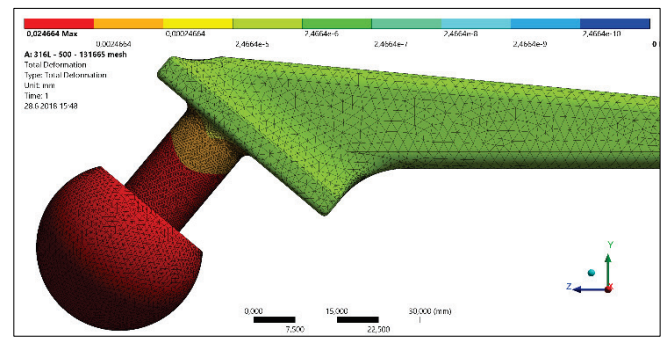
Figure 2 Loads and boundary conditions applied to geometry

3 RESULTS

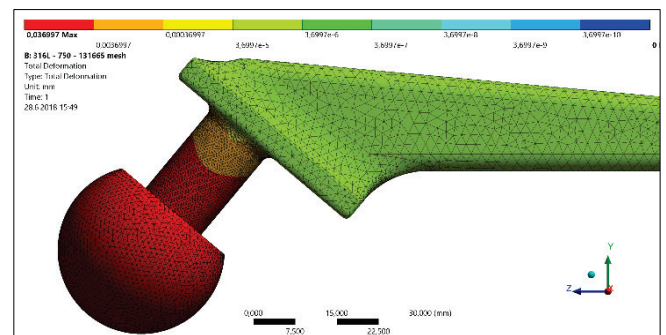
In Fig. 3 and 4, Von-Mises equivalent stresses and total deformations occurring under 500, 750 and 1000 N loads are given for femoral prosthesis made of 316L stainless steel alloy material. The maximum stresses on the prosthesis were seen in the regions where the neck and body parts joined. When the stress analysis results and total deformation data are examined together, it can be seen that the greatest strain change due to stress is in the region where stress is greatest, that is, the region where the prosthesis neck and body join. The maximum total deformation occurs at the head of the prosthesis. The highest total deformation and tensile strengths were observed in prostheses for 1000 N load, as 0.049329 mm and 174.05 MPa, respectively.

In Fig. 5 and Fig. 6, Von-Mises equivalent stresses and total deformations occurring under 500, 750 and 1000 N loads are given for femoral prosthesis made of Ti6Al4V material. Under the load of 1000 N, a total deformation obtained as 0.086237 mm and an equivalent stress obtained as 174.05 MPa. Under 750 N load, 0.064678 mm total deformation and 130.24 MPa equivalent stress, and under a load of 500 N, 0.043118 mm total deformation, 86.25 MPa equivalent stress occurred. The greatest displacement occurs at the head of the prosthesis, the greatest deformation and the greatest stress, in the regions where the prosthesis body and neck join.

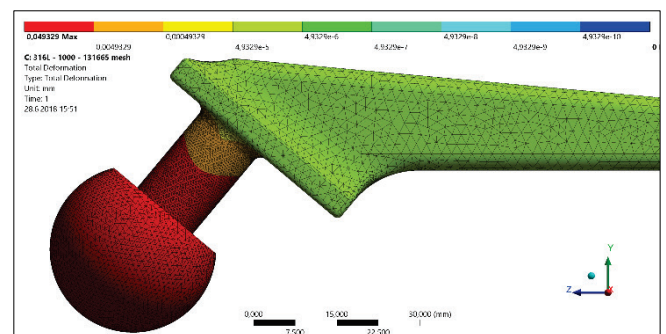
Fig. 7 shows the safety coefficients calculated for yield strength of 316L stainless steel alloy and Ti6Al4V titanium alloy femoral prosthesis. Although the deformations and displacements in the Ti6Al4V alloy prosthesis are larger, the safety factors under different loads have been determined to be significantly higher than those of the 316L stainless steel prosthesis. The static safety coefficient of the 316L stainless steel prosthesis under the 1000 N load drops below 2 (~1.72). It will be understood that this prosthesis has a safety factor that is small enough to cause an undesirable situation in terms of human health when it is thought to be exposed to different dynamic loads, twists and shrinks during the vital activities of an overweight patient. This result shows that the 316L stainless steel alloy is mechanically biodegradable as a femoral prosthetic material for overweight patients.



(a)

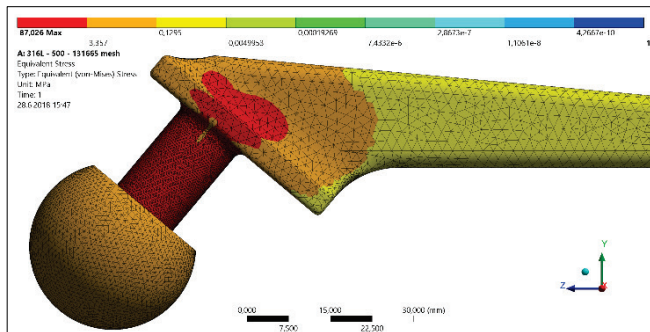


(b)

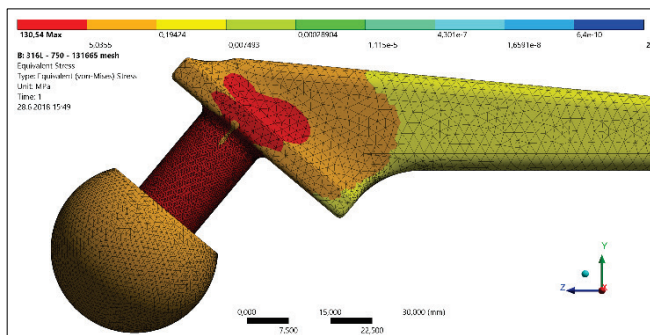


(c)

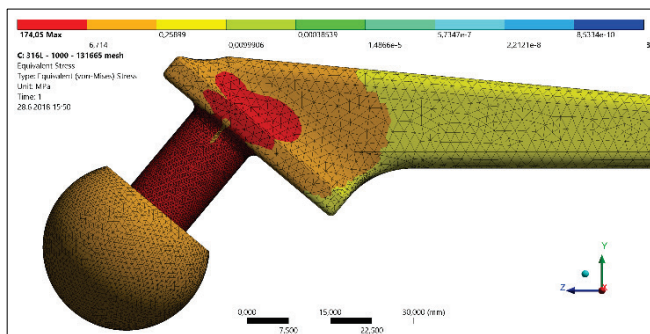
Figure 3 Total deformations under (a) 500 N, (b) 750 N, and (c) 1000 N loads on 316L femur prosthesis



(a)

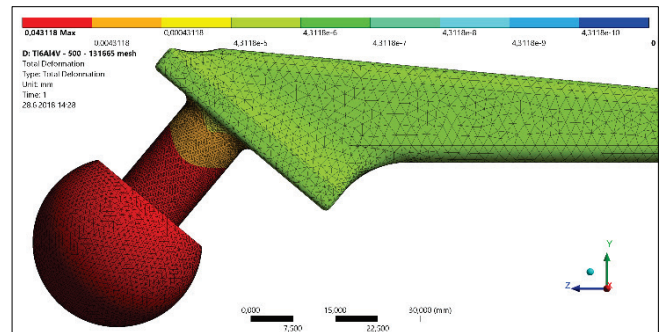


(b)

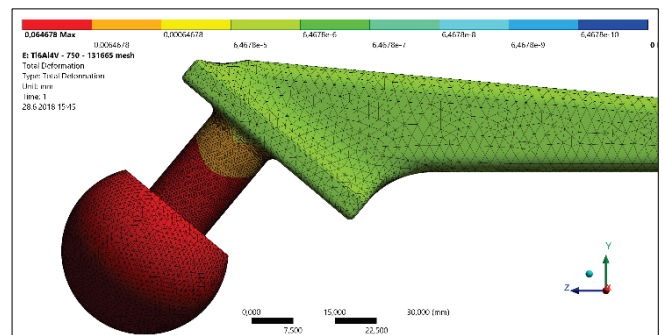


(c)

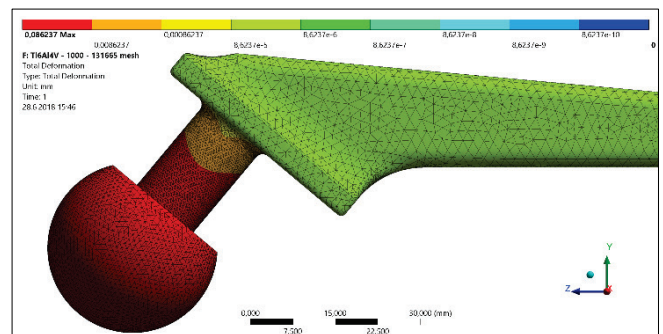
Figure 4 Equivalent stresses under (a) 500 N, (b) 750 N, and (c) 1000 N loads on 316L femur prosthesis



(a)



(b)



(c)

Figure 5 Total deformations under (a) 500 N, (b) 750 N, and (c) 1000 N loads on Ti6Al4V femur prosthesis

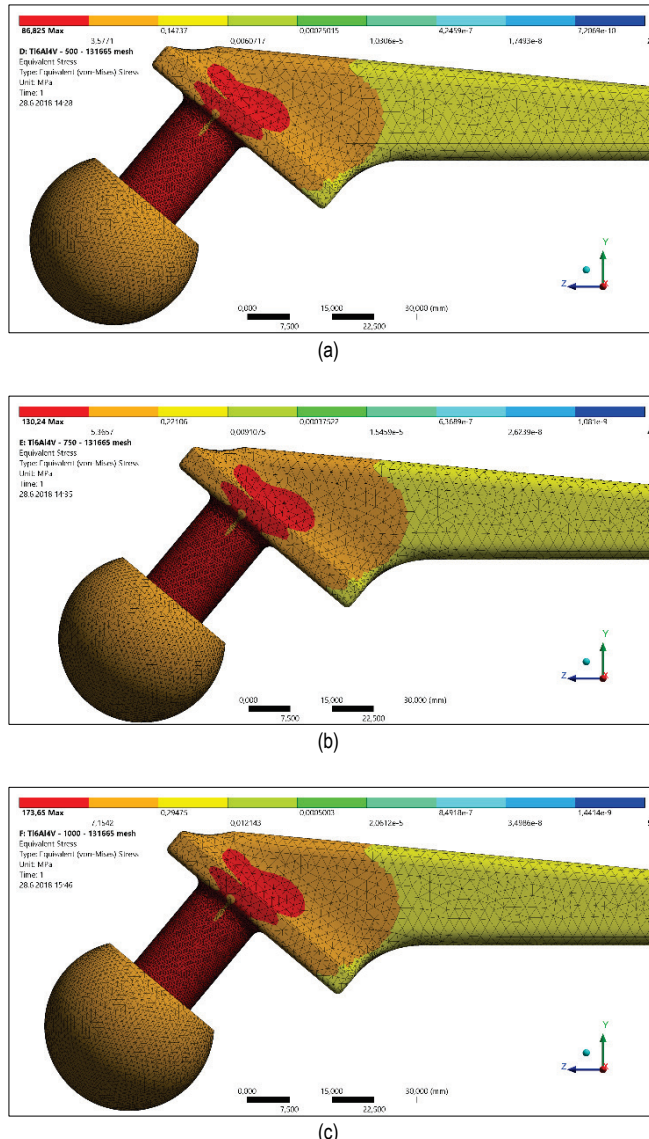


Figure 6 Equivalent stresses under (a) 500 N, (b) 750 N, and (c) 1000 N loads on Ti6Al4V femur prosthesis

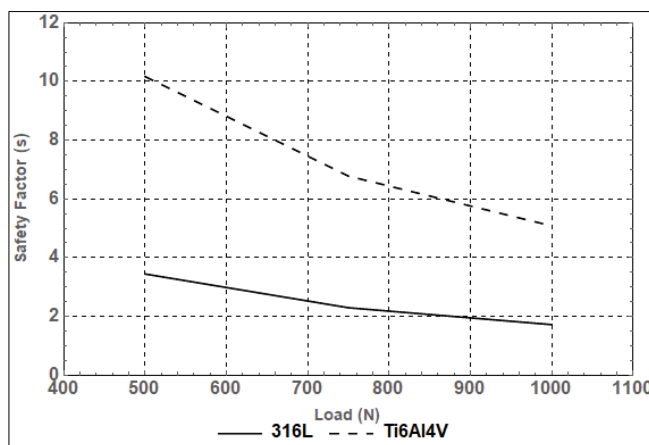


Figure 7 Maximum safety coefficients calculated according to yield strength of 316L stainless steel alloy and Ti6Al4V titanium alloy femoral prostheses

4 DISCUSSIONS

In biomaterials, mechanical properties are of great importance in terms of biocompatibility. In this study, human femoral prosthesis was modelled using 316L stainless steel and Ti6Al4V titanium alloys and static analysis was performed under 500, 750 and 1000 N loads.

The results of the analyses are as follows:

- 1) With the femur implants whose body part is fixed in the bone, the region where the prosthesis body and neck join is the most critical region of the implant in terms of static resistance. This region is also critical in terms of fatigue due to constantly changing stresses during vital activities.
- 2) The load resulting from the weight of the human body causes the greatest spatial displacement at the head of the femoral implant. The largest deformation occurs in the neck region where stress is the highest.
- 3) The 316L stainless steel alloy is mechanically biodegradable to replace the femur bone in overweight patients.
- 4) Ti6Al4V titanium alloy has very high mechanical biocompatibility even in patients with high piles.

5 REFERENCES

- [1] Gür, A., & Taşkın, M. (2004). Metalik biyomalzemeler ve biyoyoum. *Doğu Anadolu Bölgesi Araştırmaları Dergisi*, 2, 106-113.
- [2] Özalp, Y., & Özdemir, N. (1996). Biyomateryaller ve biyoyoumluluk. *Ankara Üniversitesi Eczacılık Fakültesi Dergisi*, 2, 57-72.
- [3] Manivasagam, G., Dhinasekaran, A., & Rajamanickam, A. (2010). Biomedical implants: corrosion and its prevention. *Recent Patents on Corrosion Science*, 2, 40-45. <https://doi.org/10.2174/1877610801002010040>
- [4] Mudali, U. K., Sridhar, T. M., & Raj, B. (2003). Corrosion of bio implants. *Sadhana*, 28(3-4), 601-637.
- [5] Thomann, U. I., & Uggowitz, P. J. (2000). Wear-corrosion behavior of biocompatible austenitic stainless steels. *Wear*, 239, 48-58. [https://doi.org/10.1016/S0043-1648\(99\)00372-5](https://doi.org/10.1016/S0043-1648(99)00372-5)
- [6] S. F. E., Shi, L., Guo, Z. G., & Liu, W. M. (2015). The recent progress of tribological biomaterials. *Biosurface and Biotribology*, 1, 81-97. <https://doi.org/10.1016/j.bsbt.2015.06.002>
- [7] Atilla, B. & Alpaslan, M. (2002). Materyaller ve Enfeksiyon. *TOTBİD*, 1(2): p. 111-113.
- [8] Tuncer, S. & Demirci, M. (2011). Dental materyallerde biyoyoumluluk değerlendirmesi. *Atatürk Üniv. Diş Hek. Fak. Der.*, 21(2), 141-149.
- [9] Maharaj, P. S. R., Maheswaran, R., & Vasanathanan, A. (2013). Numerical analysis of fractured femur bone with prosthetic bone plates. *Procedia Engineering*, 64, 1242-1251. <https://doi.org/10.1016/j.proeng.2013.09.204>
- [10] Nithin, K. K. C., Tandon, T., Silori, P., & Shaikh, A. (2015). Biomechanical stress analysis of a human femur bone using ANSYS. *Materials Today: Proceedings*, 2, 2115-2120. <https://doi.org/10.1016/j.matpr.2015.07.211>
- [11] Ebrahimi, H., Rabinovich, M., Vuleta, V., Zalcmán, D., Shah, S., Dubov, A., Roy, K., Siddiqui, F. S., Schemitsch, E. H., Bougherara, H., & Zdero, R. (2012). Biomechanical properties of an intact, injured, repaired and healed femur: An

- experimental and computational study. *Journal of the Mechanical Behavior of Biomedical Materials*, 16, 121-135.
<https://doi.org/10.1016/j.jmbbm.2012.09.005>
- [12] Özkan, A., Mutlu, İ., Atmaca, H., Buluç, L., Müezzinoğlu, M. S., & Kişioğlu, Y. (2009). İnsan uyluk kemiğinin (femur) modellenmesi ve yük dağılım analizi. *UMTS2009: Kıbrıs*.
- [13] Özkan, A. & Atmaca, H. (2013). Femur boyun geometrisinin ve pelvis üzerindeki gerilme dağılımına etkisi. *Düzce Tıp Dergisi*, 15(2), 1-6.
- [14] Marangoz, S. (2009). Gelişimsel Koksa Vara, *Türk Ortopedi ve Travmatoloji Birliği Derneği Dergisi*, 8(3-4), 30-34.
- [15] Hanumantharaju, H. G. & Shivanand, H. K. (2009). Static analysis of bi-polar femur bone implant using FEA. *Int. J. of Recent Trends in Engineering and Technology*, 1(5), 118-121.
- [16] Gervais, B., Vadean, A., Raison, M., & Brochu, M. (2016). Failure analysis of a 316L stainless steel femoral orthopedic implant. *Case Studies in Engineering Failure Analysis*, 5(6), 30-38. <https://doi.org/10.1016/j.csefa.2015.12.001>
- [17] Davis, E. T., Olsen, M., Zdero, R., Papini, M., Waddell, J. P., & Schemitsch, E. H. (2009). A biomechanical and finite element analysis of femoral neck notching during hip resurfacing. *Journal of Biomechanical Engineering*, 131(4), 041002-041002-8. <https://doi.org/10.1115/1.3072889>
- [18] Spinelli, L. F., Macedo, C. A. S., Galia, C. R., Rosito, R., Schnaid, F., Corso, L. L., & Iturrioz, I. (2012). Femoral stem-bone interface analysis of logical uncemented stem. *Revista Brasileira de Engenharia Biomédica*, 28(3), 238-247.
<https://doi.org/10.4322/rbeb.2012.031>
- [19] Aydın, İ., Çetinel, H., Pasinli, A., & Yuksel, M. (2013). Preparation of hydroxyapatite coating by using citric acid sodium citrate buffer system in the biomimetic procedure. *Materials Testing*, 58(2), 140-145.
<https://doi.org/10.3139/120.110826>

Authors' contacts:**Saim KURAL**, Asst. Prof. Dr.

Mechanical Engineering Dept., Manisa Celal Bayar University
MCBU Engineering Faculty AB-18 Yunusemre-Manisa Türkiye
+90 236 201 2380
saimkural@gmail.com

Safiye İPEK AYVAZ, Lecturer

Corresponding Author
Turgutlu Vocational High School, Manisa Celal Bayar University
Belediye Fidanlık Tesisleri 45400 Turgutlu-Manisa Türkiye
+90 236 313 5502
s.ipekayvaz@gmail.com

APPLICATION OF THERMOELECTRIC MODULES AS RENEWABLE ENERGY SOURCES

Ivan ŠUMIGA, Dunja SRPAK, Živko KONDIĆ

Abstract: Thermoelectric modules are used for heating or cooling if an electric current flows through them. If one side of such a module is heated and the other side is cooled, the outputs show a potential difference that creates the current flow through an enclosed circuit. The paper describes briefly the physical basis of the operation of semiconductor thermoelectric modules and their application for generating electricity as thermoelectric generators. The experimental measurements were made with different available modules of thermoelectric generators. The analysis of obtained results has provided the conclusions about the possibility of their application as sources of electricity. Although the efficiency of thermoelectric modules is still quite low, the latest research reveals the possibility of the use of materials that make modules more efficient. Considering the fact that they do not contain moving parts, they are characterized by reliable, long-lasting work and simple operation and maintenance.

Keywords: electricity generation; materials; Peltier's cell; reliability; renewable energy sources; thermoelectric module

1 INTRODUCTION

Thermoelectric modules are often used for heating or cooling, but they can be used as generators as well, if one side of this module is heated and the other one is cooled. The basic concept of the thermoelectric theory is described in [1], as well as the experimental techniques helpful in the research of new thermoelectric materials.

The status of material development and thermo-electric applications is reviewed in [2]. The potential of achieving the environmental and economic benefits with thermoelectric applications in different areas are presented there, concluding the usability for micro/small applications, with the current conversion efficiency. However, using thermoelectrics in medium/large scale applications would be possible with better thermo-electric materials.

Different mechanical and electrical structures were explored in [3] to find the optimal solution to apply thermoelectric generators in low temperature resources, such as on thermal and geothermal sites or facilities where thermal energy is a by-product. Testing with different materials for thermoelectric generators in geothermal resources is also discussed in [4]. The evaluation of the manufacturability of thermoelectric devices combined with the total cost of system components is described in [5] in various applications for the use of the waste heat. Different vehicular applications are analyzed in [6] in order to reduce energy losses. Finding the optimal solution for the use of thermoelectric generators in automobiles was studied in [7-9] in order to recover the waste heat from the exhaust. As a heat source for thermoelectric generators, heat pipes were tested in [10] and the solar radiation in [11].

Theoretical analyses and experimental research as presented in [12-15] seek for better materials and structures that can improve the efficiency of thermoelectric modules.

This research examines the usability of market available thermoelectric modules with different prices but with similar technical characteristics. A comparison of the achieved electrical values will demonstrate the profitability of

applying the tested modules in the use of waste heat from industrial machines.

The paper is organized as follows. First, the physical basis of the operation of semiconductor thermoelectric modules is described. Then, the possibility of their application for generating electricity is analyzed. The results of experimental measurements on several available thermogenerator modules are presented afterwards. The analysis of the obtained results, as well as the conclusions, give an overview of the possibilities of applying the Peltier modules as thermoelectric generators.

2 DESCRIPTION OF THERMOELECTRIC MODULES

If the electric conductive material is heated at one end, the electrons on that warmer part have higher kinetic energy than those at the colder part. Therefore, it comes to the electron diffusion from the warmer end to the colder end, i.e. the electrons are going to the state of lower temperature. Due to the uneven distribution of electrons, an electric field is formed, with a positive pole on the warmer part and negative pole on the colder part of the wire. The difference in potentials is created at the ends of the wire, which represent the source of the electromotive force.

If the connection point of two different metals that form an electrical circuit is heated, (point B in Fig. 1), the U_o voltage will appear between the T1 and T2 points. That voltage is known as Seebeck's electromotive force. If resistance is connected between T1 and T2, the electrical current will flow through it. The compound acts as a thermoelectric voltage generator.

On the other hand, if the U_{in} voltage is connected between T1 and T2, current will flow in that closed loop. At the junction point A of two metals, the cooling effect occurs because of the current flow; while at the junction point B, the heating effect appears (Fig. 2). By changing the polarity of the voltage, the current flow is also changed. That results with the cooling in point B and heating in point A. Herein, the amount of heat absorbed at the cold end is equal to the heat released at the warm end.

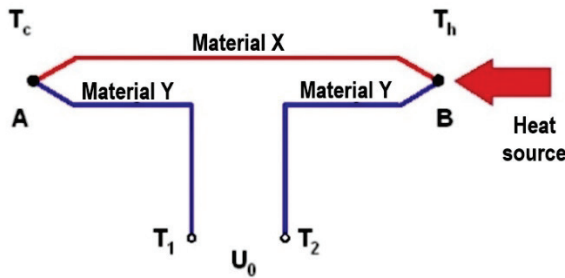


Figure 1 Seebeck effect [16]

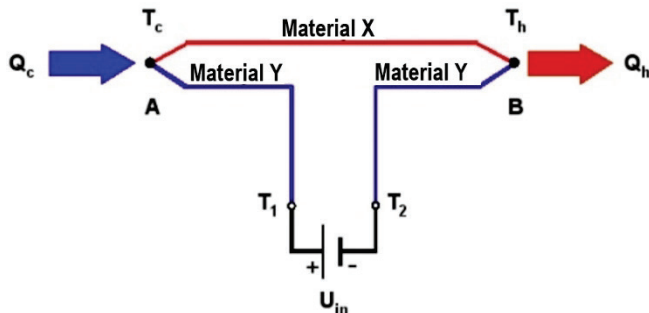


Figure 2 Peltier effect [16]

This phenomenon was first described by the French physicist Jean Peltier; therefore, it is called the Peltier effect. By applying the described phenomenon, a thermoelectric power generator or a heating or cooling device can be realized. The use of semiconductors instead of metals brings significant progress in the realization of thermoelectric modules. The realization of the thermoelectric module with semiconductors is shown in Fig. 3.

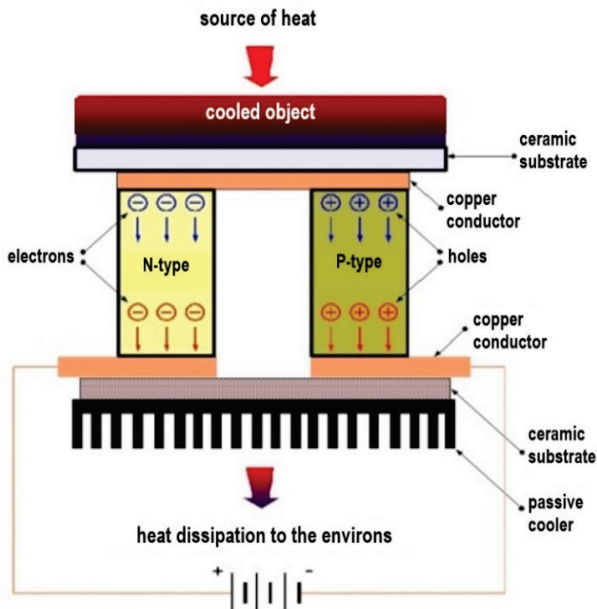


Figure 3 Thermoelectric modules for heating / cooling [16]

The free electrons in the copper conductor are at a higher energy level than the holes in the p-type semiconductor. Therefore, electrons release a part of the heat energy when passing from the copper conductor to the semiconductor. In

the p-type semiconductor, electrons are recombined with the holes that move in the valence energy field of the semiconductor in the direction opposite of the direction of electron shifting. Since the p-type semiconductor is at a lower energy level than the conductor, at the next transition point, from the p-type semiconductor to the copper conductor, the electrons have to absorb the needed energy, due to which this joint is colder.

The next joint is the connection of the cold conductor, the n-type semiconductor having a bottom of the conductive band at the higher energy level than Fermi level of the conductor. The electrons need to re-absorb enough heat energy to pass into the conductive band of the n-type semiconductor, which is why the joint is colder. Through the n-type semiconductor, electrons move in a conductive energy band to the next connection of metals and semiconductors. Since free electrons in the conductive energy band of semiconductors are at a higher energy level than the Fermi level of the metal, at the transition to metal, they lose energy. Therefore, this joint is warmer than the environment.

Since no juncture of metal and semiconductor is a rectifier, by alteration of the polarity of external voltage, the side of the module used for cooling can also perform heating.

In order to obtain the higher heating or cooling power, more of the basic modules can be connected in series. Thus, the Peltier's heat pump is made, and is assembled of a large number of alternately arranged basic elements between two ceramic layers (Fig. 4). The heating or cooling capacity of such a heat pump depends on geometric dimensions, the number of the p-type and n-type semiconductor pairs, as well as on the properties of used materials. Unlike Joule's heat, which is proportional to the square of current, in this pump, the heat is proportional to the current.

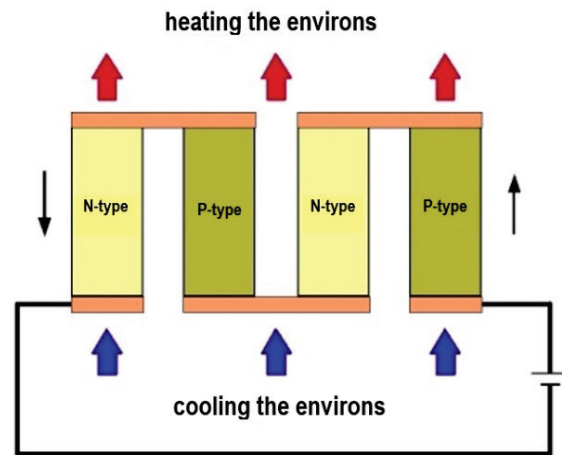


Figure 4 Serial connection of modules [16]

The basic module for the thermoelectric generator is shown in Fig. 5.

If the hotter ends of the p-type and n-type semiconductors are joined together by metal, and electrical resistance is connected between the colder ends, the voltage caused by the Seebeck effect will send the electric current through resistance. Such a joint generates power on the

electric consumer. The serial connection of more modules can create higher voltages.

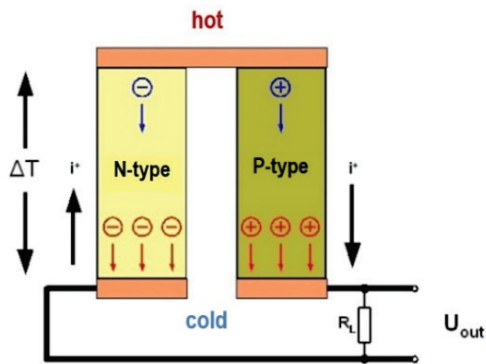


Figure 5 Thermoelectric generator [16]

3 MATERIALS FOR THERMOELECTRICAL MODULES

Until the end of the last century, an interest in thermoelectric modules was not large because of low efficiency in most applications. Theoretical analyses suggesting that certain material structures could improve the efficiency of thermoelectric modules stimulated the experimental research of different material structures with the aim of realizing modules that would have acceptable efficacy in certain applications [15-17].

In the realization of thermoelectric modules, high efficiency is important at the transformation of electricity in the heat or vice versa. The most important requirements for module materials are electrical and thermal conductivity. Electrical conductivity should be as large as possible. Considering this, they must be cold at one end of the module and warm at the other, and the heat conductivity should be as low as possible in order to maintain the temperature difference, i.e. the high temperature gradient.

The problem is that materials that have high electrical conductivity also have high thermal conductivity. Therefore, as thermoelectric materials are those semiconductor structures investigated, that show the high conductivity of free electrons and at the same time aggravating the movement of a quantum of heat energy (phonon). Until today, the compounds of the tellurite family have been shown as one of the best.

The materials from which thermoelectric modules were made are called thermoelectrics. Their quality is evaluated by a parameter called the thermoelectric figure of merit (ZT), which is defined by the Eq. (1):

$$ZT = \frac{\alpha^2 \sigma}{\kappa} T \quad (1)$$

Where α – Seebeck's coefficient, σ – specific conductivity of the material, κ – coefficient of thermal conductivity, and T – temperature. The dependency of ZT factors on today's temperature change most frequently used p-types and n-types of thermoelectrics, as it is shown in Figs. 6 and 7, respectively.

For PbTe, the values of the ZT factor in 1960 and today are shown. Significant improvements can be noted, due to technological progress. It is also visible that different materials have maximal ZT at different temperature ranges: lead-telluride (PbTe), silicon-germanium (SiGe) and bismuth antimony alloy (Bi-Sb).

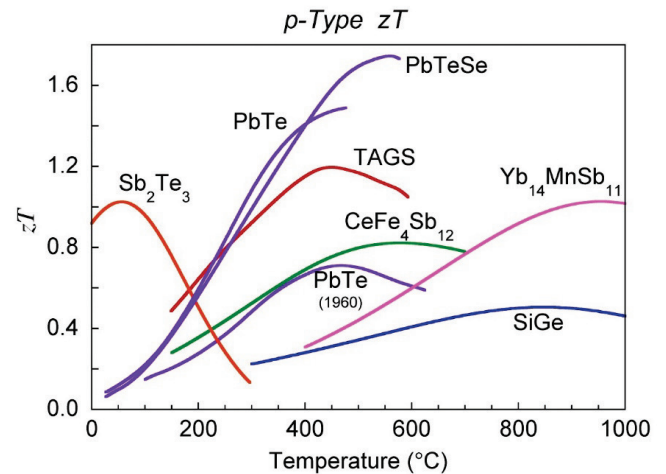


Figure 6 Thermoelectric figure of merit for the p-type of thermoelectrics [17]

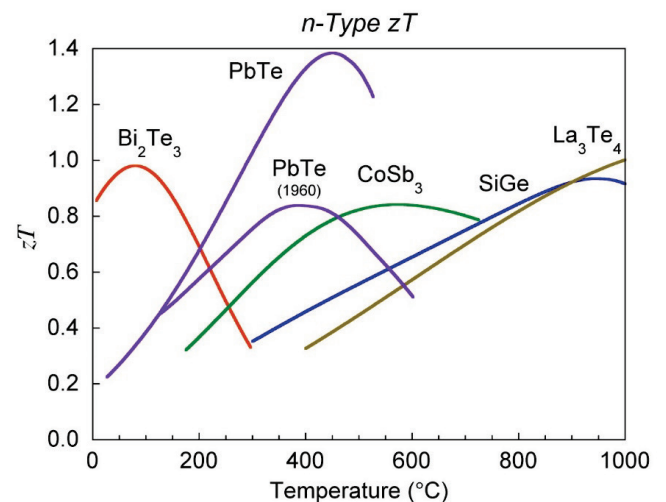


Figure 7 Thermoelectric figure of merit for the n-type of thermoelectrics [17]

The higher the value of the thermoelectric figure of merit, the better the thermoelectric material. Today, most materials have the value of ZT less than 1. The ZT value of the specific material will be higher if its specific electrical conductivity is higher and if the coefficient of thermal conductivity is lower. For a particular dielectric, the area where ZT is the highest is obtained with well-doped p-type and n-type semiconductors (free concentration of electrons or holes between 10^{19} and 10^{20} per cubic centimeter).

Today, the intensive search for materials that will have a ZT greater than 1 is conducted by using the latest developments in the field of nanotechnology [16]. Thereby, a particular interest is placed on a complex crystal structure where the aim is to disperse the phonons within the unit cell of the structure, thus reducing thermal conductivity, but without disturbing the flow of electrons, i.e. without reducing

electrical conductivity. According to the available information, the value of $ZT = 2.4$ is reached, and in the near future $ZT = 3$ can be expected [13].

Although the effectiveness of new materials has to yet be tested, the promising ZT intensifies the research and experimentation with new thermoelectrics. For a large number of applications, materials with a thermoelectric figure of merit between 2 and 3 will be competitive to other renewable energy sources.

4 COOLING

Thermoelectric modules are used for heating or cooling when the electrical current is sent through them, or for electricity generation when one side is heated and the other one is cooled. In both applications, the most important part is the good thermal bondage of the hot and cold side of the module and environment. On the other hand, thermal conductivity within the module itself should be as low as possible in order to maintain a temperature difference of the hot and cold sides.

If the module is used for cooling, the other side of the module will dissipate the heat. Therefore, it is necessary to mount a cooler on the module to dissipate the generated Joule's heat because of the electrical resistance of the module and the heat from the heat pump. The surface of the module that for the beholder appears to be smooth and flat, under the magnifying glass often looks as seen in Figure 8. When the heat cooler is placed on such a surface, the heat passes only where the surfaces are touching, which is only about 5% of the surface. The larger parts of the surfaces (95%) actually do not touch each other. In order to increase contact surface, a thermal paste must be used to fill the cavities.



Figure 8 The contact of two apparently smooth surfaces

The cooler should have the temperature increase as low as possible during the operation of the module. The acceptable increase of temperature of the passive cooler is 5 - 10 °C above the ambient temperature. For low-power heat pumps, the passive coolers with natural convection of heat resistance of 0.5 °C/W, but often also with over 10 °C/W, are used. The coolers combined with a cooling fan (with forced convection) with a heat resistance of 0.02 - 0.5 °C/W are more efficient. The liquid cooled passive coolers have an even higher thermal efficiency per volume unit, of 0.01 to 0.1 °C/W.

5 APPLICATION OF THERMOELECTRICAL MODULES

The greatest advantage of thermoelectric modules is that they work without moving parts, which significantly simplifies maintenance. Moreover, their reliable and long-lasting operation does not depend on the module position or the environment. They do not create clamor or electric noise

during operation, so they can be used together with sensitive electronic sensors. Compared to mechanical systems for the same purpose, thermoelectric modules are much smaller and lighter, having the same power. Additionally, they do not use any chemicals or gases that can be harmful to the environment during the work.

Thermoelectric modules are used in activities with different technical requirements: military, medical, industry, telecommunications, science and consumer technology. The heating or cooling function depends only on the polarity of the connected voltage.

Thermoelectric refrigerators can remove the heat from mW to several thousands of W. The most used modules are those with the size of 100 W.

Thermoelectric modules are used as coolers for laser diodes, laboratory instruments, electronic casings and components, etc. With a suitable control circuit, the temperature adjustment precision can be even below ± 0.001 °C.

The function of generating the electricity depends on the temperature difference between the hot and cold side of the module.

Today, many companies produce thermoelectric generators that convert waste heat into electricity. They use different heat sources (hot plate heaters, gas cookers, wood stoves, etc.) that can generate power from about 10 W to the size of several hundreds of W. For cooling, they use ambient temperature, fan or water. Thermoelectric generators are mostly used for lighting, powering up the electronic devices and charging batteries. They are lightweight, small in dimensions, robust and practical to carry.

The most modern thermoelectrics allow the realization of thermoelectric generators that are by volume competitive to batteries and to solar cells and wind power plants by economics.

Because of their robustness, (lifetime of modules is often higher than the lifetime of other equipment), they are interesting for the military industry and space programs (spacecraft, satellites) and for applications in inaccessible locations or in extreme conditions (lighthouses, isolated islands).

At remote, isolated locations, robust thermoelectric generators that use waste heat can be combined with a solar power plant as the reliable power supply system for various consumers (sensors, actuators, wireless communication devices, maintenance and monitoring systems, etc.).

In the area of small dimensions, low power and small temperature differences, thermoelectric generators are particularly interesting in converting the heat of a human body into electrical energy. An example described in [18] is a wristwatch powered by a thermoelectric generator with 22 μ W at a temperature difference of 1.5 °C.

Thermoelectric generators, due to their robustness and longevity, can provide power supplies for medical devices such as pacemakers. That can extend life expectancy for thirty years, a fivefold increase compared to today's technology.

6 TESTINGS

Testing was conducted in order to establish the possibilities of application of commercially available modules for electricity generation from the waste heat of some machines.

To draw the conclusions on the possibility of using thermoelectric generators, three different modules of M1, M2 and M3 were purchased. The dimensions of the modules are:

- M1: length 40 mm, width 40 mm, height 3.6 mm,
- M2: length 40 mm, width 40 mm, height 3.8 mm,
- M3: length 57 mm, width 54.4 mm, height 3.4 mm.

Module prices are also different. Module M1 is the cheapest, M2 is considerably more expensive and M3 is even more expensive. Identical tests were conducted on all three modules, under the same conditions. The aim was not to measure module parameters in laboratory conditions, but to compare the modules' properties by using the available equipment.

The aluminum plates, each 10mm thick, were placed on both sides of the thermoelectric module. To reduce the thermal resistance between the aluminum plates and the modules, a thin layer of thermal paste was applied on both sides of the module. The aluminum plate on the warm side was heated with electric heaters and the plate on the cold side was cooled with ice. Holes were made in aluminum plates at the contact place with the module, within which the temperature sensors were installed. During the measurement process, it was noticed that the quality of the join with the ice tray on the cold side of the module had the most influence on the generated voltage.

For each module, the following measurements were done, according to the electrical schemes in Figs. 9-11:

1. Idle voltage at various temperature differences (Fig. 9),
2. Short circuit current at various temperature differences (Fig. 10),
3. Currents and voltages for various loads on the module at various temperature differences (Fig. 11).

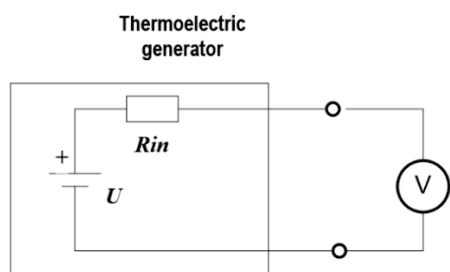


Figure 9 Electrical scheme for the measurement of idle voltage

Idle voltage was measured with a voltmeter connected to the external outputs of thermogenerators. The hot side of the M1 module was heated up to 120 °C, and of the modules M2 and M3 up to 180 °C, whilst cooling the other side with ice. The temperature of the cold side (T_c) did not exceed 30 °C at M1, 40 °C at M2 and 50 °C at M3, even at the highest temperatures of the warm side (T_h). At the warm side of the modules, the permissible temperature limits were considered

(for M1, T_h did not exceed 120 °C, and for M2 and M3 190 °C). It should be noted that the same temperature difference ($\Delta T = T_h - T_c$) can be achieved with e.g. $T_c = 20$ °C or $T_c = 80$ °C. Higher T_c results in reduced power for the same load.

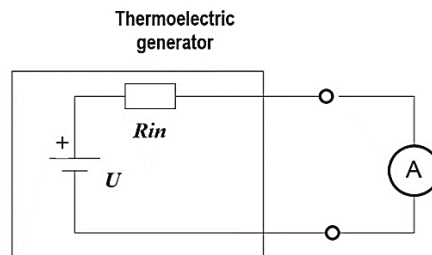


Figure 10 Electrical scheme for the measurement of short circuit current

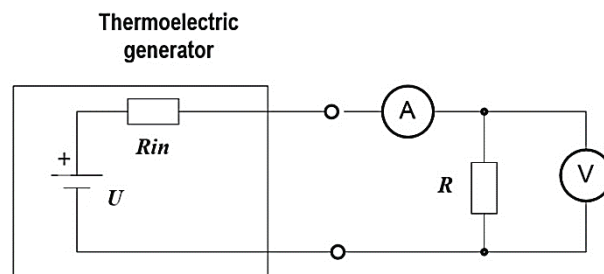


Figure 11 Electrical scheme for the measurement of currents and voltages for various loads

In Fig. 12, it can be seen that the module M1 reached the maximum idle voltage of around 4 V, M2 around 10 V and M3 around 18 V.

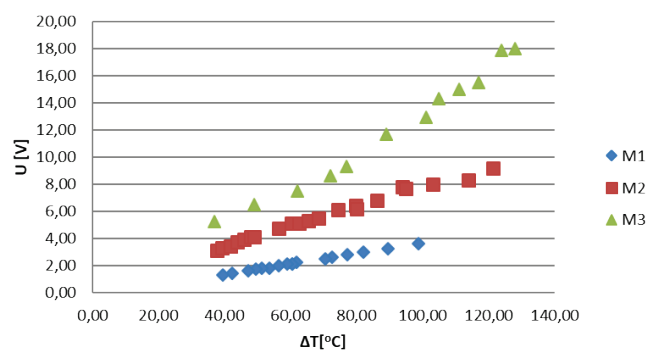


Figure 12 Dependency of the idle voltage and the temperature difference

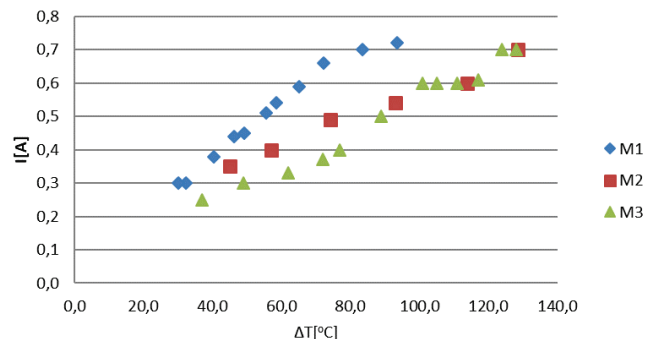


Figure 13 Dependency of the short circuit current and the temperature difference

The short-circuit current was measured with an ammeter connected to the external outputs of thermogenerators. The measurement procedure was carried out for different temperatures under the same conditions as previously explained. Fig. 13 shows the obtained results. It can be noticed that the maximum short circuit current is approximately the same for all modules despite the different idling voltages. The reason for that is the greater internal resistance of the M2 and M3 modules.

Based on the short circuit current measured according to Fig. 10 and idle voltage measured according to Fig. 9, the internal resistance of the thermogenerator as a source can be obtained ($R_{in} = U / I$). The changes of R_{in} with the change of temperature difference is shown in Fig. 14.

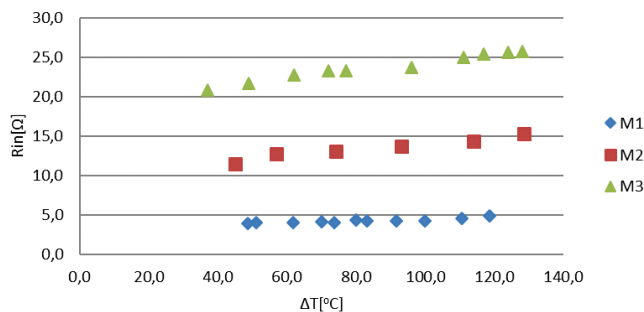


Figure 14 Dependency of the internal resistance and the temperature difference

The thermogenerator M1 has an internal resistance of around 5 Ω, M2 of around 15 Ω and M3 of 20 - 30 Ω. It is visible that the internal resistance of the thermo-generator slightly increases with the increase of ΔT .

Power measurement as the product of the output current and voltage ($P = U \cdot I$) was performed on resistors of 4 Ω, 10 Ω, 20 Ω and 40 Ω, according to the electrical scheme in Fig. 11. Figs. 15-18 show the achieved power for different resistors for all three modules.

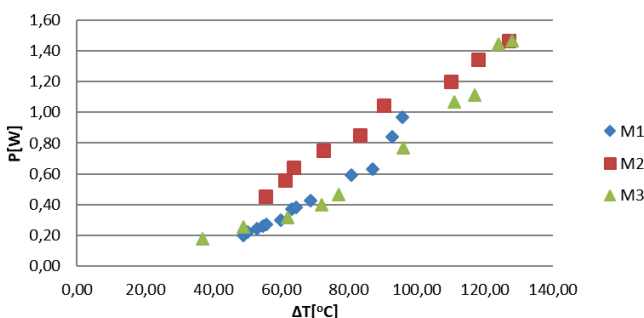


Figure 15 Achieved power for all three modules at $R = 4 \Omega$

Based on the diagrams in Figs. 15-18, it can be concluded which module will give the maximum power for a given temperature difference, with which resistance, to a certain consumer. Thus, the module M1 gives the highest power rating to the resistor of 4 Ω, the module M2 to the resistor of 10 - 20 Ω and the module M3 to the resistor around 20 Ω. Figs. 19-21 show the power that each module gives for different loads. From these diagrams, the expected useful

power on the resistors can be determined for a given temperature difference.

The efficiency of the tested modules of M1, M2 and M3 is below 10% and it depends on the connected load. For the tested loads, it was mostly higher on M3 and M2, while slightly smaller on M1. Modules that are more expensive are more efficient, because they can work at higher temperature differences.

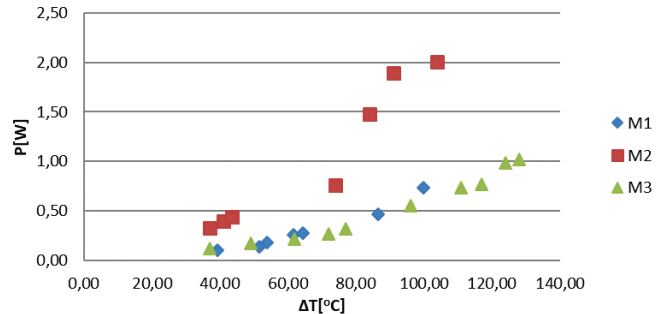


Figure 16 Achieved power for all three modules at $R = 10 \Omega$

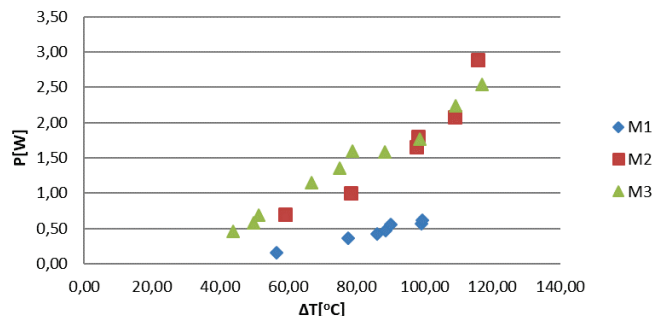


Figure 17 Achieved power for all three modules at $R = 20 \Omega$

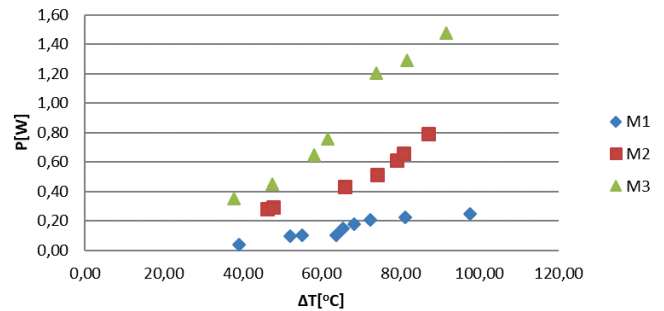


Figure 18 Achieved power for all three modules at $R = 40 \Omega$

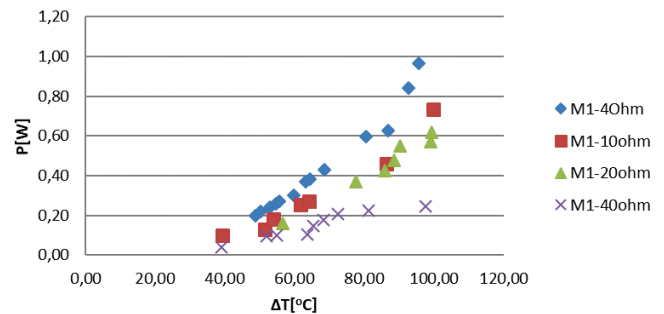


Figure 19 Achieved power for the module M1 for each resistor

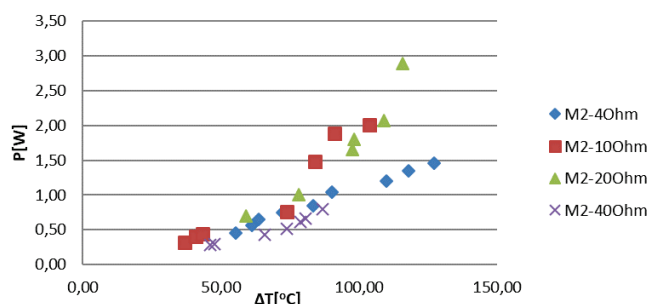


Figure 20 Achieved power for the module M2 for each resistor

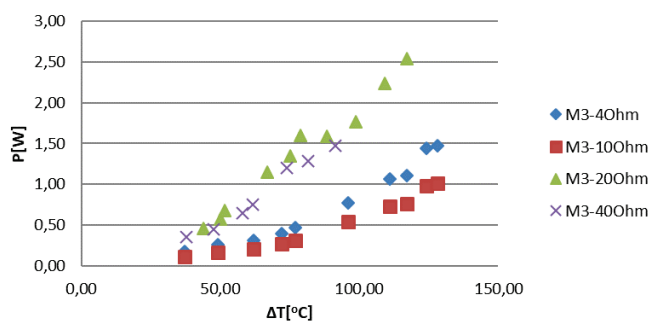


Figure 21 Achieved power for the module M3 for each resistor

7 CONCLUSION

Although the efficiency of the thermoelectric modules is still quite low, the latest research has resulted in materials needed for the building of increasingly more efficient modules. Those modules can be competitive to the renewable sources of electricity such as solar power plants and wind power plants. The greatest advantages of thermoelectric generators are small dimensions, compactness, long lasting, quiet and reliable operation because they do not have moving parts, they have low maintenance requirements and a wide range of heat sources.

Despite the low efficiency of the conversion of thermal energy to electricity, the interest in thermoelectric modules is constantly increasing due to the fact that waste heat is used and the thermoelectric figure of merit of the thermoelectrics increases. Therefore, the presence of thermoelectric modules and thermoelectric generators in the market is on the rise. Moreover, the generators used today have the power range from μW to kW .

This paper presents the experimental results of measurements on three different modules. The maximum voltage of 3.6 V at $\Delta T = 100\text{ }^\circ\text{C}$ was achieved by measuring on module M1. At the same value of ΔT , M2 gives 8 V and M3 gives 13 V . Since the modules of M2 and M3 can work at higher temperatures, the measured voltage on M2 is 9.2 V and on M3 it is 18 V at a temperature difference of $\Delta T = 120\text{ }^\circ\text{C}$. All modules show linear dependence of the generated voltage on the rise in the temperature difference ΔT (Fig. 9). The maximum short circuit current is approximately the same on all modules, considering the fact that the modules that can generate higher voltages have higher internal resistance (Fig. 11). The maximum power measured on the module M1 is about 1 W at $\Delta T = 100\text{ }^\circ\text{C}$, and for M2 and M3 slightly above 2.5 W at $\Delta T = 120\text{ }^\circ\text{C}$.

The tested modules point to the conclusion that the modules that are more expensive give higher energy density per unit of volume at higher temperatures. On the other side, cheaper modules are more cost-effective due to a large number of inexpensive modules in order to compensate for the lack of power on a single unit. Considering the small dimensions of the modules, the realization of a thermal power generator with lower kW power can be competitive with wind power plants and solar power plants.

Note: This research was partially presented as a poster at the International Conference MATRIB 2017 (29 June - 2 July 2017, Vela Luka, Croatia).

8 REFERENCES

- [1] Nolas, G. S., Sharp, J., & Goldsmid, H. J. (2001). *Thermoelectrics: basic principles and new materials developments*, Springer. <https://doi.org/10.1007/978-3-662-04569-5>
- [2] Zheng, X. F., Liu, C. X., Yan, Y. Y., & Wang, Q. (2014). A review of thermoelectrics research – Recent developments and potentials for sustainable and renewable energy applications. *Renewable and Sustainable Energy Reviews*, 32, 486-503. <https://doi.org/10.1016/j.rser.2013.12.053>
- [3] Chen, J., Li, K., Liu, C., Li, M., Lv, Y., Jia, L., & Jiang, S. (2017). Enhanced Efficiency of Thermoelectric Generator by Optimizing Mechanical and Electrical Structures. *Energies*, 10, 1329. <https://doi.org/10.3390/en10091329>
- [4] Liu, C., Chen, P., & Li, K. (2014). A 1 kW Thermoelectric Generator for Low-temperature Geothermal Resources. *Proceedings, Thirty-Ninth Workshop on Geothermal Reservoir Engineering*, Stanford University, Stanford, California, February 24-26.
- [5] LeBlanc, S. (2014). Thermoelectric generators: Linking material properties and systems engineering for waste heat recovery applications. *Sustainable Materials and Technologies*, 1-2, 26-35. <https://doi.org/10.1016/j.susmat.2014.11.002>
- [6] Fairbanks, J. W. (2006). Thermoelectric developments for vehicular applications. *Diesel Engine-Efficiency and Emissions Research (DEER) Conference*, Detroit, MI.
- [7] Lui, X., Deng, Y. D., Chen, S., Wang, W. S., Xu, Y. & Su, C. Q. (2014). A case study on compatibility of automotive exhaust thermoelectric generation system, catalytic converter and muffler. *Case Studies in Thermal Engineering*, 2, 62-66. <https://doi.org/10.1016/j.csite.2014.01.002>
- [8] Su, C. Q., Wang, W. S., Liu, X., & Deng, Y. D. (2014). Simulation and experimental study on thermal optimization of the heat exchanger for automotive exhaust-based thermoelectrical generators. *Case Studies in Thermal Engineering*, 4, 85-91. <https://doi.org/10.1016/j.csite.2014.06.002>
- [9] Bai, S., Lu, H., Wu, T., Yin, X., Shi, X., & Chen, L. (2014). Numerical and experimental analysis for exhaust heat exchanger for automobile thermoelectric generators. *Case Studies in Thermal Engineering*, 4, 99-112. <https://doi.org/10.1016/j.csite.2014.07.003>
- [10] Orr, B., Akbarzadeh, A., Mochizuki, M., & Singh, R. (2016). A review of car waste heat recovery systems utilising thermoelectric generators and heat pipes. *Applied Thermal Engineering*, 101, 490-495. <https://doi.org/10.1016/j.applthermaleng.2015.10.081>

- [11] Jaworski, M., Bednarczyk, M., & Czachor, M. (2016). Experimental investigation of thermoelectric generator (TEG) with PCM module. *Applied Thermal Engineering*, 96, 527-533. <https://doi.org/10.1016/j.applthermaleng.2015.12.005>
- [12] Brown, S. R., Kauzlarich, S. M., Gascoin, F., & Snyder, G. J. (2006). Yb₁₄MnSb₁₁: New High Efficiency Thermoelectric Material for Power Generation. *Chemistry of Materials*, 18(7), 1873-1877. <https://doi.org/10.1021/cm060261t>
- [13] Yan, X., Poudel, B., Ma, Y., Liu, W. S., Joshi, G., Wang, H., Lan, Y., Wang, D., Chen, G., & Ren, Z. F. (2010). Experimental Studies on Anisotropic Thermoelectric Properties and Structures of n-Type Bi₂Te_{2.7}Se_{0.3}. *Nano Letters*, 10(9), 3373-3378. <https://doi.org/10.1021/nl101156v>
- [14] Cooley, J. A., Promkhan, P., Gangopadhyay, S., Donadio, D., Pickett, W. E., Ortiz, B. R., Toberer, E. S., & Kauzlarich, S. M. (2018). High Seebeck Coefficient and Unusually Low Thermal Conductivity near Ambient Temperatures in Layered Compound Yb_{2-x}Eu_xCdSb₂. *Chemistry of Materials*, 30(2), 484-493. <https://doi.org/10.1021/acs.chemmater.7b04517>
- [15] Qiu, B., Bao, H., Zhang, G., Wu, Y., & Ruan, X. (2012). Molecular dynamics simulations of lattice thermal conductivity and spectral phonon mean free path of PbTe: Bulk and nanostructures. *Computational Materials Science*, 53, 278-285. <https://doi.org/10.1016/j.commatsci.2011.08.016>
- [16] Šumiga, I., Grđan, M., & Huđek J. (2007). Termoelektrični moduli – fizikalne osnove i smjernice za uporabu. *Technical journal*, 1(1-2), 5-10.
- [17] <http://thermoelectrics.matsci.northwestern.edu/thermoelectrics> Available May 2017.
- [18] Snyder, G. J. (2008). Small thermoelectric generators. *Electrochemical Society Interface*, 17, 54-56.

Authors' contacts:

Ivan ŠUMIGA, MSc, Senior Lecturer
University North, University Centre of Varaždin
104. brigade 3, 42000 Varaždin, Croatia
e-mail: ivan.sumiga@unin.hr

Dunja SRPAK, PhD, Lecturer
(Corresponding author)
University North, University Centre of Varaždin
104. brigade 3, 42000 Varaždin, Croatia
e-mail: dunja.srpak@unin.hr

Živko KONDIĆ, PhD, Professor
University North, University Centre of Varaždin
104. brigade 3, 42000 Varaždin, Croatia
e-mail: zivko.kondic@unin.hr

COLOR PERCEPTION OF THE OBSERVER WITH THE MANIFESTATION OF THE CHROMATIC EFFECT OF CRISPENING

Krunoslav HAJDEK, Petra BRADIĆ, Martina HAJDEK, Mile MATIJEVIĆ

Abstract: This research presents the results of the appearance of chromatic effect of crispening on a designer solution in which the primary stimuli are made in the purple color with the values of 55% RTV and 65% RTV and backgrounds are made in the green-blue color, and their variations are designed in the values of 25% RTV, 50% RTV, 75% RTV and 100% RTV that are placed around the primary stimuli. The test subjects (n=10) that took part in the research had the task to equalize the test primary stimuli with the referential stimuli on a computer screen with the help of the technique of simultaneous binocular harmonization. The strength of the crispening effect was defined and shown in the CIEDE00 system. The conclusion of the conducted tests indicates that the intensity of crispening was stronger on the test primary stimuli 65% RTV, where the differences in the perception of color were more significant.

Keywords: color; crispening; perception; vision adaptation; visual psychophysics

1 INTRODUCTION

Simultaneous contrast is one of the oldest illusions for perception. Simultaneous contrast is a psychophysical visual effect that causes a shift in the manifestation of the color of a stimulus. It is caused by a change in the background color (Fig. 1). Simultaneous contrast is the effect that shows that the representation of one part of light depends not only on the light but also on the context in which the light is presented [1, 2]. The effect of simultaneous contrast is a subjective psychological experience, which is proved by the fact that the same physical stimulation (the same dominant wavelength) in different people causes different color experiences. Studying the phenomenon of simultaneous contrast has a long history [3]. It is one of the most studied phenomena ever since Aristotle's time [4]. Despite more than a century of intense research and study of simultaneous contrast, it is still a confusing and poorly understood phenomenon [5].

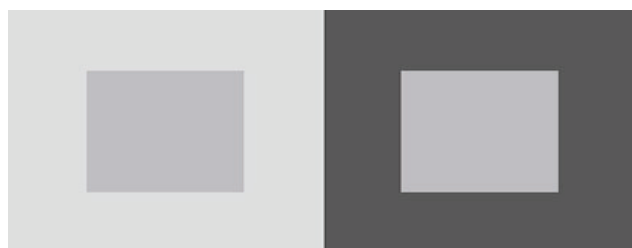


Figure 1 Example of the effect of simultaneous contrast

There are two explanations for this effect. One explanation stems from Hering's idea of processes in the optical system [6, 7], whereas the other stems from Helmholtz [8], who claims that the effect is a result of erroneous illumination.

As we very rarely see a particular color, isolated simultaneous contrast affects our sensation of the color we see. Put differently, a background which is light causes the enhancement of the characteristics of a particular stimulus so that it may appear darker, i.e. a dark background affects the

perception on its surface so that the observed stimulus appears lighter on it. Many studies include color and its lightness, which are mostly described by the scientists Beck [9] and Wyszecki [10].

The main parameter in color dynamics is the contrast that also has a great impact on color perception. The contrast describes the influence of one color on the perception of colors in adjacent areas [11]. Contrast is the difference of luminance between the surfaces of different areas and/or elements on the surface [12]. When placing a brighter color as the background, the color appears darker; while when placing a darker color as the background, the color appears brighter.

Apart from the aforementioned psychophysical visual effect of achromatic simultaneous contrast which is also called achromatic induction, there is also chromatic induction which is based on the difference between the chromatic pairs of colors.

The psychophysical visual effect that seemingly increases the intensity of the perception of color between the two stimuli of color that are being compared is called crispening (Fig. 2). The background itself, in that case, must be very similar to the perception of the color of the stimuli [13].



Figure 2 Example of the crispening effect

The effect of crispening was first discovered and named by Takasaki in his papers [14, 15]. Semmerloth [16] follows his research, and recently, the scientist Whittle is significantly involved in the research of the crispening effect

[17]. Hajdek et al. already explored in what way the crispening effect [18] and the simultaneous contrast effect [19, 20] with a change in background lightness affect the perception of the respondents.

In each research of the crispening effect, it is always necessary to determine to what extent the variations in the lightness or color of the background affect the shift in the cognizance of the viewer, and to establish the difference that will be present on the same model that causes the appearance of the background effect and that is presented in another media. Accordingly, it was sought, by using particular formulas, to establish in advance the possible intensity of the crispening effect in relation to the switch in the lightness/color of the background [21, 22].

In this article, what is presented are the results of the research of the appearance of the chromatic crispening effect on a designer solution where the inner squares (primary stimuli) are made in the purple color with the values 55% RTV and 65% RTV, and the backgrounds (secondary stimuli) are made in the green-blue color and their variations are designed in the values of 25% RTV, 50% RTV, 75% RTV and 100% RTV which encircle the inner squares. The selected RTV values of primary stimuli (55% RTV and 65% RTV) and secondary stimuli (25% RTV, 50% RTV, 75% RTV and 100% RTV) were used to cover the entire area of RTV color coverage from 0%-100% RTV in increments of 25% RTV. Backgrounds are divided into four areas 0-25% RTV, 25%-50% RTV, 50%-75% RTV and 75% -100% RTV. Primary stimuli of 55% RTV and 65% RTV were used as mean values, but the value of 50% RTV for primary stimuli was avoided because that value would cause an effect of assimilation at the same value of background [19, 20].

2 EXPERIMENTAL PART

This research is a continuation of the research conducted by the same authors [23]. In this part of the work, samples due to which the manifestation of the crispening effect appears were designed. The chromatic test samples were designed in a next manner: as a secondary stimulus, a square was colored in the green-blue color; and for the primary stimulus, the purple color was used. For the background, four variations were used; the initial secondary stimuli had the value of 25% RTV, and every following background was increased by 25% RTV. Within this geometrical shape, there are two same, but smaller geometrical shapes which represent the primary stimuli, and they are painted in the purple color that has the value of 55% RTV for the left rectangle and 65% RTV for the right rectangle (Figs. 3-6). The mentioned samples are seen as referential, and below them, there were samples with the background of a particular value, and on them were empty fields (white) of the primary stimuli, where the subjects had the task of choosing the harmonized values of the primary stimuli so that the test primary stimuli be, as they perceive them, the same/similar as possible to the referential primary stimuli.

Test samples were designed in the Indesign CC program, and the referential primary stimuli had the following Lab values: square of 55% RTV; $L = 72,00$, $a = 41,00$ and $b =$

$-6,00$, and the values of the referential primary stimuli of 65% RTV were $L = 67,00$, $a = 49,00$ and $b = -7,00$. The test subjects in the experiment used the technique of simultaneous binocular harmonization [24, 25] (original and reproduction are in visual field at the same time), and they were given the instructions to try to harmonize (equalization of the referential and test primary stimuli in order so they are perceived the same or equally) in the Indesign CC program the empty fields so that they are the same/similar to the value of the field of the referential primary stimuli that are situated right above the test sample, and the secondary stimuli were in the corresponding values of all four RTV (25% RTV-100% RTV), on the referential sample and the test sample respectively.



Figure 3 Used sample with the background of 25% RTV and the inner squares of 55% RTV (L) and 65% RTV (R)



Figure 4 Used sample with the background of 50% RTV and the inner squares of 55% RTV (L) and 65% RTV (R)

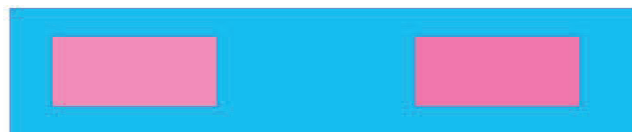


Figure 5 Used sample with the background of 75% RTV and the inner squares of 55% RTV (L) and 65% RTV (R)



Figure 6 Used sample with the background of 100% RTV and the inner squares of 55% RTV (L) and 65% RTV (R)

The lack of the Indesign CC program is that the mentioned program allows only the use of whole numbers without decimal points.

The samples were evaluated on a Lenovo G580 portable computer that had a LED-backlit HD Vibrant View display, diagonal of the screen of 15.6" and a resolution of 1366×768. The conditions in which the experiment was carried out were in conformity with the ISO 3664:2009 guidelines (distance from the screen of 60 cm, viewing angle of 10° and D50 lighting), and the subjects had unlimited time for their experimental evaluation.

Ten subjects of both sexes with no previous experience in the research of this type evaluated the samples. Every test subject who was involved in the experiment had to pass the

Ishihara test for defective color vision which confirmed that every subject was 100% successful on the test.

The research results are presented with the ΔE_{00} formula [26].

$$\Delta E_{00} = \left[\left(\frac{\Delta L'}{k_L S_L} \right)^2 + \left(\frac{\Delta C'_{ab}}{k_C S_C} \right)^2 + \left(\frac{\Delta H'_{ab}}{k_H S_H} \right)^2 + R_T \left(\frac{\Delta C'_{ab}}{k_C S_C} \right) \left(\frac{\Delta H'_{ab}}{k_H S_H} \right) \right]^{0.5} \tag{1}$$

Where S_L stands for lightness compensation, S_C for chroma compensation, S_H for hue compensation and R_T for hue rotation. The k_L , k_C and k_H factors are the unity and weighting factors that depend on the material that they are being measured on (graphic arts of textiles).

$$\Delta L = L'_b - L'_s \tag{2}$$

$$\Delta C'_{ab} = C'_{ab,b} - C'_{ab,s} \tag{3}$$

$$\Delta H'_{ab} = \left[2 \left(C'_{ab,b} C'_{ab,s} \right)^{0.5} \sin \left(\frac{\Delta h'_{ab}}{2} \right) \right] \tag{4}$$

3 RESEARCH RESULTS WITH DISCUSSION

In this section, the results of the research present how big the difference between the referential and test samples is by using the ΔE_{00} values. After subjects made the harmonization, with the use of the color picker tool, Lab values were measured on all test samples in the Indesign CC program, and the size of the difference in color between the referential and the test samples was presented with the ΔE_{00} formula.

Table 1 Display of the associated Lab values of the primary stimuli of 55% RTV for the test samples on all four background variations

Subjects	25% RTV				50% RTV				75% RTV				100 % RTV			
	L	a	b	ΔE	L	a	b	ΔE	L	a	b	ΔE	L	a	b	ΔE
1	77	32	-6	5.04	75	35	-6	2.90	75	35	-6	3.16	78	31	-5	5.82
2	69	46	-7	2.88	69	46	-7	2.88	70	44	-6	1.84	69	46	-7	2.88
3	71	42	-6	0.83	71	43	-6	1.03	71	42	-6	0.83	72	41	-6	0.00
4	69	45	-6	2.68	69	46	-7	2.87	69	45	-6	2.68	70	44	-6	1.84
5	70	44	-6	1.85	70	44	-6	1.85	68	48	-7	3.88	69	47	-7	3.07
6	73	39	-6	1.04	71	43	-6	1.03	72	41	-6	0.00	70	44	-5	1.95
7	71	42	-6	0.84	71	42	-6	0.84	71	42	-6	0.84	73	40	-6	0.83
8	69	46	-7	2.88	68	48	-7	3.88	69	45	-6	2.68	69	46	-7	2.87
9	7	44	-6	1.85	70	44	-6	1.85	71	43	-6	1.03	72	41	-6	0.00
10	70	44	-6	1.85	72	41	-6	0.00	72	41	-6	0.00	74	38	-6	1.85

Tab. 1 presents every Lab value individually, for every test subject who harmonized the test primary stimuli compared to the referential primary stimuli with the value of 55% RTV on every background variation (25% RTV, 50% RTV, 75% RTV, and 100% RTV).

It can also be seen from Tab. 1 how large the value of the ΔE_{00} difference between both samples for every test subject individually is.

Table 2 Display of the associated Lab values of the primary stimuli of 65% RTV for the test samples on all four background variations

Subjects	25% RTV				50% RTV				75% RTV				100 % RTV			
	L	a	b	ΔE	L	a	b	ΔE	L	a	b	ΔE	L	a	b	ΔE
1	66	51	-7	1.02	68	48	-7	0.85	63	56	-7	3.90	72	41	-6	4.71
2	64	55	-7	3.04	65	54	-7	2.22	65	54	-7	2.22	64	55	-7	3.04
3	64	56	-7	3.22	64	55	-7	3.04	64	55	-7	3.04	66	51	-6	1.02
4	64	55	-7	3.05	64	56	-7	3.23	65	53	-7	2.03	66	52	-7	1.23
5	65	54	-7	2.22	67	49	-7	0.00	63	57	-7	4.06	66	51	-7	1.02
6	69	46	-7	1.85	69	46	-7	1.85	67	49	-7	0.00	68	48	-7	0.86
7	69	45	-6	2.07	67	50	-7	0.31	69	46	-7	1.85	68	48	-7	0.86
8	67	49	-7	0.00	65	53	-7	2.03	65	53	-7	2.03	64	55	-7	3.05
9	65	54	-7	2.22	64	56	-7	3.23	6	55	-7	3.05	63	56	-7	3.90
10	68	48	-7	0.86	68	48	-7	0.86	69	47	-7	1.71	67	49	-7	0.00

Tab. 2 presents every Lab value individually, for every test subject who harmonized the test primary stimuli compared to the referential primary stimuli with the value of 65% RTV on every background variation.

It can also be seen from Tab. 2 how large the value of the ΔE_{00} difference between both samples for every test subject individually is.

In the next part of the article, Figs. 7-10 present the measured difference of the ΔE_{00} value for every test subject

on the primary stimuli of 55% RTV, and the difference is shown for every secondary stimulus individually.

In Fig. 7, subjects harmonized the primary stimuli of 55% RTV, where the background is of 25% RTV, and it shows that the biggest difference belonged to subject 1, while on the other hand, the smallest difference belonged to subjects 3 and 7, where the difference basically does not exist due to the fact that subjects harmonized the values of both stimuli very close to each other.

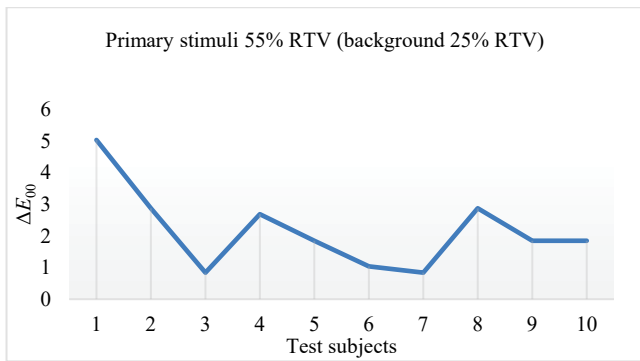


Figure 7 Display of the ΔE_{00} difference for every subject for the primary stimuli of 25% RTV on the secondary stimuli of 25% RTV

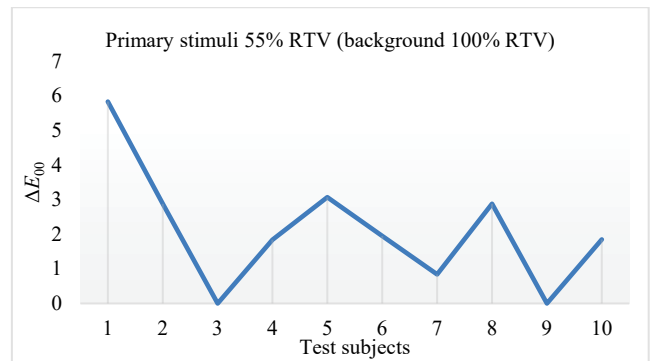


Figure 10 Display of the ΔE_{00} difference for every subject for the primary stimuli of 55% RTV on the secondary stimuli of 100% RTV

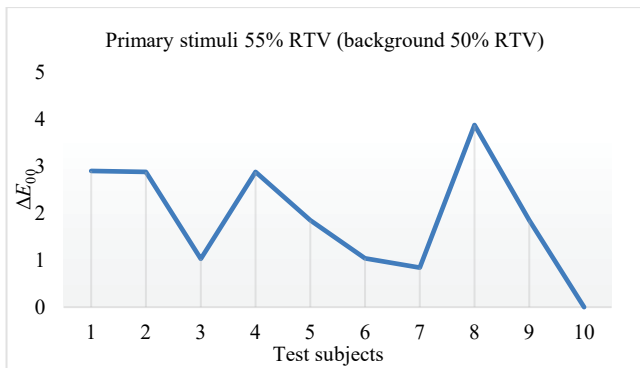


Figure 8 Display of the ΔE_{00} difference for every subject for the primary stimuli of 55% RTV on the secondary stimuli of 50% RTV

Fig. 8 presents the results of harmonization on the primary stimuli of 55% RTV with the background of 50% RTV, and it shows that the biggest difference belonged to subject 8, while on the other hand, the smallest difference belonged to subject 10; in fact, there is no difference due to the fact that the subject harmonized the values of the test stimuli equivalently to the values of the original pattern.

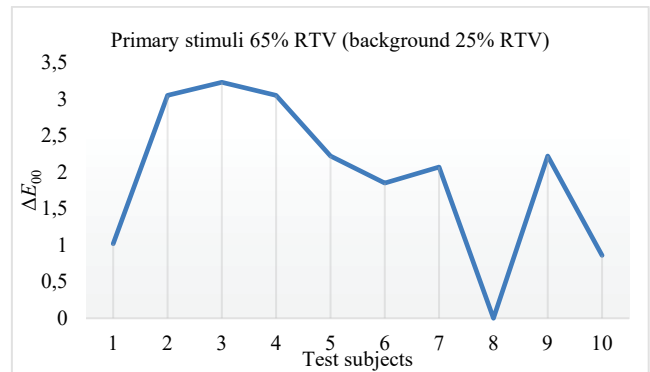


Figure 11 Display of the ΔE_{00} difference for every subject for the primary stimuli of 65% RTV on the secondary stimuli of 25% RTV

Fig. 11 presents the results of the harmonization of the primary stimuli of 65% RTV on the background of 25% RTV, and it shows that the biggest difference belonged to subject 3, while the smallest difference belonged to subject 8, who harmonized the test primary stimuli equivalently to the values of the original primary stimuli.

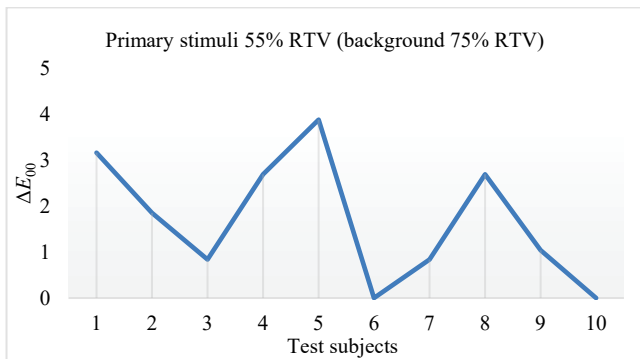


Figure 9 Display of the ΔE_{00} difference for every subject for the primary stimuli of 55% RTV on the secondary stimuli of 75% RTV

Fig. 9 shows the harmonization of the primary stimuli of 55% RTV on the background of 75% RTV, and it shows that the biggest difference belonged to subject 5, while on the other hand, the smallest difference belonged to subjects 6 and 10; in fact, there are no differences.

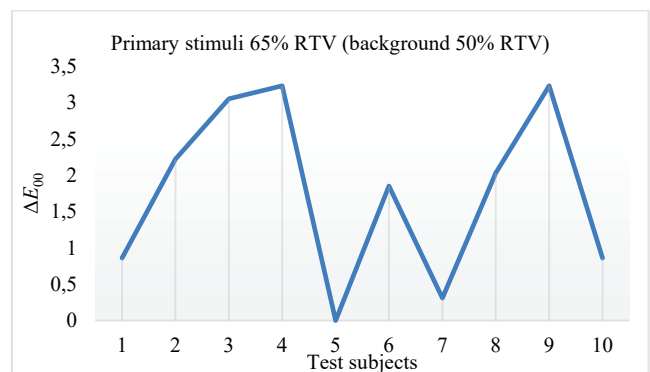


Figure 12 Display of the ΔE_{00} difference for every subject for the primary stimuli of 65% RTV on the secondary stimuli of 50% RTV

In Fig. 12, where it can be seen that the subjects had the task to harmonize the primary stimuli of 65% RTV on the background of 50% RTV, it is shown that the biggest difference belonged to subjects 4 and 9, while on the other hand, the smallest difference belonged to subject 5, due to the fact that subject 5 harmonized the values of the test stimuli equivalently to the referential stimuli.

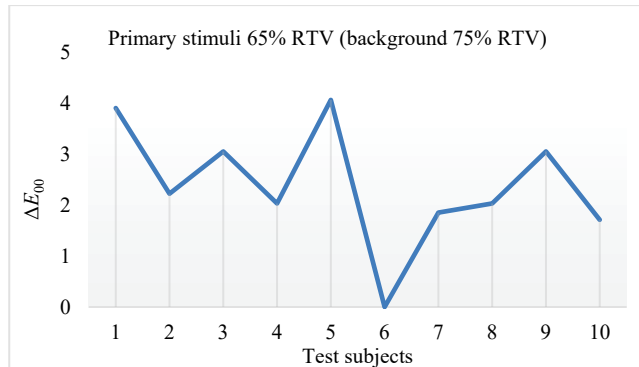


Figure 13 Display of the ΔE_{00} difference for every subject for the primary stimuli of 65% RTV on the secondary stimuli of 75% RTV

In Fig. 13, where it can be seen that the subjects had the task to harmonize the primary stimuli of 65% RTV with the background of 75% RTV, it is shown that the biggest difference belonged to subject 5, and that the smallest difference belonged to subject 6, who harmonized the test stimuli equivalently to the original stimuli (referential).

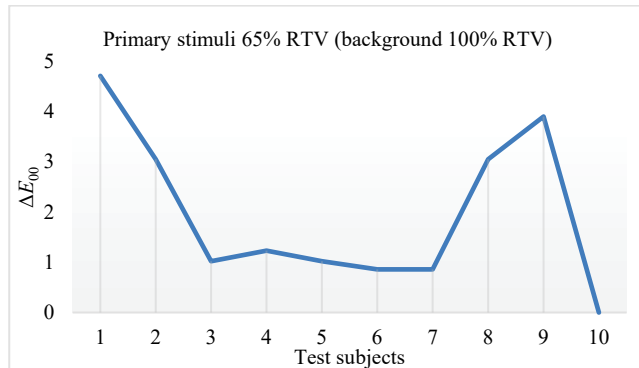


Figure 14 Display of the ΔE_{00} difference for every subject for the primary stimuli of 65% RTV on the secondary stimuli of 100% RTV

In Fig. 14, where it can be seen that the subjects had the task to harmonize the primary stimuli of 65% RTV with the background of 100% RTV, it can be seen that the biggest difference belonged to subject 1, and that the smallest difference belonged to subject 10 on the primary stimuli, where there was actually no difference.

In the Figs. 15-18, it can be seen how big the difference of every subject is for both primary stimuli (55% RTV and 65% RTV) on every background variation.

Fig. 15 shows the comparison of both test primary stimuli for every subject on the secondary stimuli of 25% RTV. From Fig. 15 it can be seen that the subjects accomplished nearly identical results of the harmonization on both primary stimuli. In other words, the overall sum of

the ΔE_{00} values for the test primary stimuli of 55% RTV is 21,74, and the overall sum of the ΔE_{00} values for the test primary stimuli of 65% RTV is 19,55.

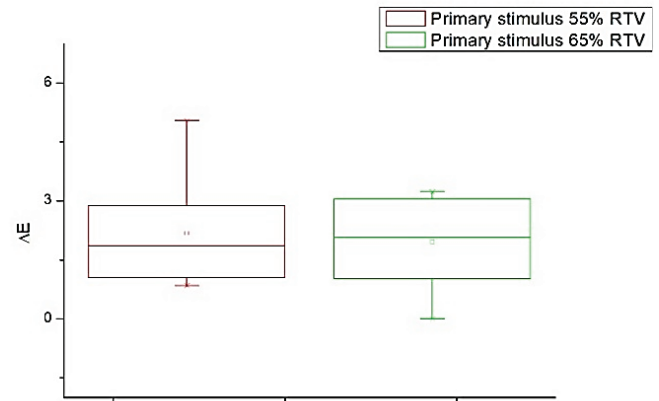


Figure 15 Presentation of the values obtained for all subjects for both primary stimuli on the secondary stimuli of 25% RTV

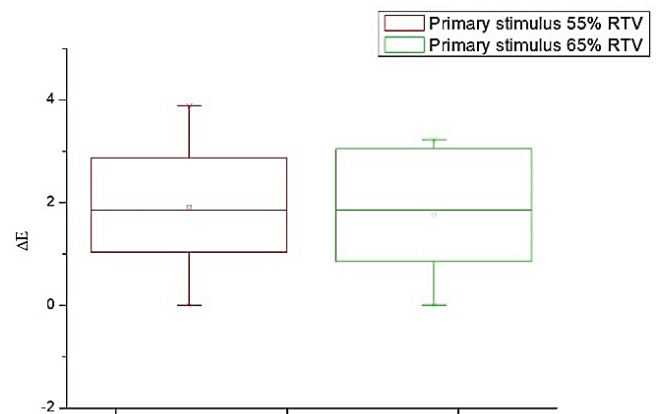


Figure 16 Presentation of the values obtained for all subjects for both primary stimuli on the secondary stimuli of 50% RTV

In Fig. 16, a comparison of both primary stimuli on the background of 50% RTV for all subjects can be seen. From Fig. 16 it can be concluded that the subjects had nearly identical results in the harmonization of both primary stimuli, as it was the case with the preceding primary stimuli of 25% RTV (Fig. 15). In fact, the overall sum of the ΔE_{00} value for the primary stimuli of 55% RTV is 19,13, while the overall sum of the ΔE_{00} value for the primary stimuli of 65% RTV is 17,62.

Fig. 17 shows the comparison of both test primary stimuli with the secondary stimuli of 75% RTV for all subjects. From Fig. 17 it can be seen that the subjects had considerably enhanced results in the harmonization of the primary stimuli of 55% RTV with regard to the primary stimuli of 65% RTV, where the difference has lower oscillations, but they are significantly more pronounced with regard to the referential primary stimuli. The overall sum of the ΔE_{00} value for the test primary stimuli of 55% RTV is 16,94, and the overall sum of the values ΔE_{00} for the test primary stimuli of 65% RTV is 23,89.

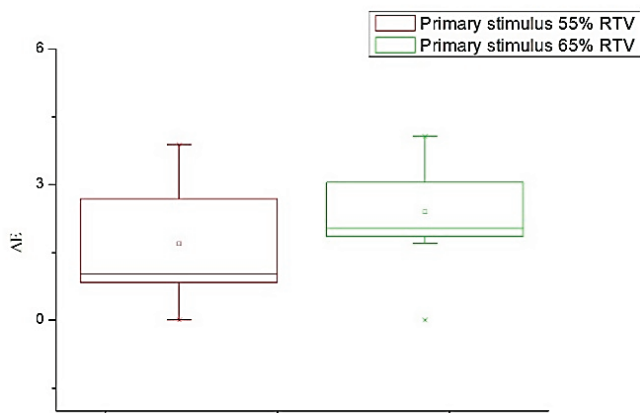


Figure 17 Presentation of the values obtained for all subjects for both primary stimuli on the secondary stimuli of 75% RTV

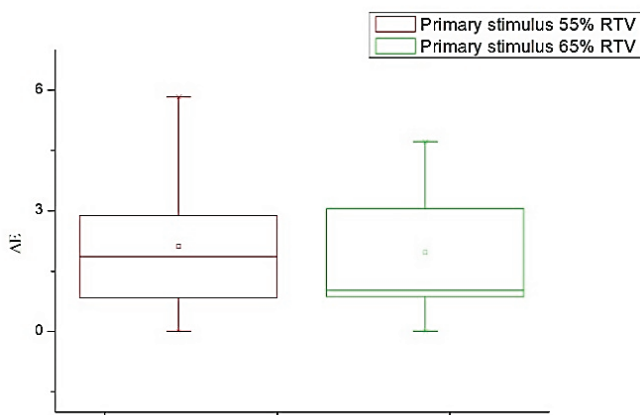


Figure 18 Presentation of the values obtained for all subjects for both primary stimuli on the secondary stimuli of 100% RTV

In Fig. 18 a comparison of both test primary stimuli for all subjects on the background of 100% RTV can be seen. Namely, Fig. 18 shows that subjects had fewer difficulties in the harmonization of the primary stimuli of 65% RTV with regard to the primary stimuli of 55% RTV. Moreover, the conclusion is that when harmonizing the test primary stimuli of 65% RTV, the subjects had less problems in coming close to the values of the referential primary stimuli. The overall sum of the ΔE_{00} value for the test primary stimuli of 55% RTV is 21,11, and the overall sum of the value ΔE_{00} for the test primary stimuli of 65% RTV is 19,69.

4 CONCLUSION

Designers, while working on their conceptual solution, unintentionally resort to the use of certain color pairs and geometric shapes that lead to the unwanted manifestation of background effects. This research created a design solution with a combination of complementary color pairs, a combination in which the primary stimuli was made in the purple color, while the background was made in the green-blue color, which led to the manifestation of the effect of crispening. With the manifestation of the effect of crispening, most subjects found it difficult to harmonize the colors of the test primary stimuli with the colors of the

referential primary stimuli. That problem appeared precisely due to the variation in the background color.

Taking into account the results of every subject, there is a small difference between the original and reproduction stimuli on the samples when we compare both primary stimuli on all variations of the secondary stimuli. Namely, the overall sum of the ΔE_{00} values of the test primary stimuli of 55% RTV is 78.92, and the overall sum of the ΔE_{00} values of the test primary stimuli of 65% RTV is 80.75. Observing the value of the test primary stimuli for each variation of the background individually, the smallest difference was recorded with the primary stimuli of 55% RTV on the secondary stimuli of 75% RTV, and the biggest difference was recorded with the primary stimuli of 65% RTV on the background with the same value as that of the test primary stimuli of 55% RTV. The best way to avoid the problem that occurs in this research is not to use geometrical shape and color combination like this one. If it necessary to use a color combination and geometrical shape that was used in this paper, the designers should consider using the color ratio that showed the smallest deviations in perception during the appearance of crispening effect like it was the case in this research paper.

5 REFERENCES

- [1] Chevreul, M. E. (1967). *The principles of harmony and contrast of colors and their applications to the arts*. New York / Reinhold Publishing Corporation, (Original work published 1839).
- [2] Helmholtz, v. H. (1962). *Treatise on physiological optics* (Vol. 2) (Southall, J. P. L. Trans.). New York / Dover, (Original work published 1866).
- [3] Kingdom, F. (1997). Simultaneous contrast: The legacies of Hering and Helmholtz. *Perception*, 26(6), 673-677. <https://doi.org/10.1068/p260673>
- [4] Wade, N. J. (1996). Descriptions of visual phenomena from Aristotle to Wheatstone. *Perception*, 25(1), 1137-1175. <https://doi.org/10.1068/p251137>
- [5] Whittle, P. (2003). Contrast colours, In R. Mausfeld, R. & Heyer, D. (Eds.), *Colour Perception: Mind and the physical world*. Oxford University Press, 115-138.
- [6] Hering, E. (1964). *Outline of a theory of light sense* (Hurvich, L. M & Jameson, D. Trans.). Cambridge / Harvard University Press, (Original work published 1905)
- [7] Cornsweet, T. (1970). *Visual perception*, Academic Press Inc., New York.
- [8] Helmholtz, v. H. (1867). *Handbuch der Physiologischen Optik*. Leipzig / Voss.
- [9] Beck, J. (1972). *Surface Color Perception*. Ithaca, Cornell University Press, New York.
- [10] Wyszecki, G. (1986). Color appearance, In Boff, K., Boff, R., Kaufman, L., & Thomas. P. J. (Eds.), *Handbook of Perception and Human Performance* (Vol. 1: Sensory Processes and Perception), John Wiley & Sons, New York.
- [11] Shepherd, A. J. (1999). Remodelling colour contrast: implications for visual processing and colour representation. *Vision Research*, 39(7), 1329-1345. [https://doi.org/10.1016/S0042-6989\(98\)00232-6](https://doi.org/10.1016/S0042-6989(98)00232-6)
- [12] Ichihara, S., Kitagawa, N., & Akutsu, H. (2007). Contrast and depth perception: effects of texture contrast and area contrast. *Perception*, 36(5), 686-695. <https://doi.org/10.1068/p5696>

- [13] Fairchild, M. D. *Color Appearance Models*, Second Edition, John Wiley & Sons Ltd, England, 2005
- [14] Takasaki, H. (1966). Lightness change of gray induced by change in reflectance of gray background. *Journal of the Optical Society of America*, 56(4), 504-509. <https://doi.org/10.1364/JOSA.56.000504>
- [15] Takasaki, H. (1967). Chromatic Changes Induced by Changes in Chromaticity of Background of Constant Lightness. *Journal of the Optical Society of America*, 57(1), 93-96. <https://doi.org/10.1364/JOSA.57.000093>
- [16] Semmelroth, C. C. (1970). Prediction of Lightness and Brightness on Different Backgrounds. *Journal of the Optical Society of America*, 60(12), 1685-1689. <https://doi.org/10.1364/JOSA.60.001685>
- [17] Whittle, P. (1992). Brightness, discriminability and the "Crispening Effect". *Vision Research*, 32(8), 1493-1507. [https://doi.org/10.1016/0042-6989\(92\)90205-W](https://doi.org/10.1016/0042-6989(92)90205-W)
- [18] Hajdek, K., Budimir, I., & Mrvac, N. (2017). The intensity of the background visual effect of crispening depending on background lightness. *Tehnički vjesnik*, 24(5), 1571-1578. <https://doi.org/10.17559/TV-20160504125704>
- [19] Hajdek, K., Budimir, I., & Krizmanić, K. (2016). The appearance of the visual effect simultaneous contrast depending on the printing substrate. *Acta graphica*, 27(3), 7-14.
- [20] Hajdek, K., Budimir, I., & Vusić, D. (2016). The intensity of the simultaneous contrast effect depending on the change of background lightness. *Tehnički vjesnik*, 23(2), 525-531. <https://doi.org/10.17559/TV-20160122205606>
- [21] Xin, J. H., Lam, C. C., & Luo, M. R. (2004). Evaluation of the crispening effect using CRT-displayed colour samples. *Color research and application*, 29(5), 374-380. <https://doi.org/10.1002/col.20045>
- [22] Ho, K. M. R., Cui, G., Luo, M. R., & Rigg, B. (2002). A Lightness Difference Formula for Predicting Crispening Effects. *The 10th Color and Imaging Conference*, Scottsdale, Arizona, USA, 161-165.
- [23] Bradić, P., Hajdek, K., Matijević, M., & Hajdek, M. (2017). The influence of the chromatic effect of crispening on the shift in the manifestation of the color of the observer. *Acta graphica*, 28(3), 85-92.
- [24] Milković, M., Mrvac, N., & Vusić, D. (2009). *Vizualna psihofizika i dizajn*. Veleučilište u Varaždinu, Varaždin, Croatia.
- [25] Lukaček, M., Milković, M., & Hajdek, K. (2013). Analiza manifestacije McCollough efekta u Cross-Media reprodukcijским sustavima. *Tehnički glasnik*, 7(2), 170-176
- [26] Kuehni, R. G. (2003). *Color Space and Its Divisions*, John Wiley & Sons, New Jersey.

Authors' contacts:

Krunoslav HAJDEK, PhD, Assistant Professor
University North
104. brigade 3
42000 Varaždin, Croatia
E-mail: khajdek@unin.hr

Petra BRADIĆ
University North
104. brigade 3
42000 Varaždin, Croatia
E-mail: pbradic@unin.hr

Martina HAJDEK
Faculty of Graphic Arts
Getaldićeva ulica 2
10000 Zagreb, Croatia
E-mail: martina.hajdek@grf.com

Mile MATIJEVIĆ, PhD, Assistant Professor
Faculty of Graphic Arts
Getaldićeva ulica 2
10000 Zagreb, Croatia
E-mail: milematijevich@gmail.com

AUTOMATIC PROCEDURAL 3D MODELLING OF BUILDINGS

Robert ŽUPAN, Katarina ŽUPAN, Stanislav FRANGEŠ, Adam VINKOVIĆ

Abstract: The problem of modelling, especially of large-scale virtual urban environments such as city areas is today very challenging for cartographers. Cities are difficult to model in detail because of their often complex geometries. This paper describes the applied and tested new procedures for the development of a test three-dimensional urban area model using the Esri CityEngine software, which is based on procedural modelling. This process involves three steps. The first step is to collect the available data, as well as the Digital Model Relief data. The second step is to create a Computer Generated Architecture (CGA) file that contains a set of rules used by the software for an automatic generation of the model. The third step is to create and visualize 3D models in the CityEngine software because it can be programmed, for example, according to the rules of cartographic visualization. The Level of Detail (LOD) 2 was reconstructed. Several potential uses of such 3D visualization are also described.

Keywords: CGA; CityEngine; procedural modelling; 3D modelling; 3D visualization

1 INTRODUCTION

3D models facilitate planning in the areas such as urban planning, energy, noise control, telecommunications, risk management, etc. 3D models of the existing state of an area also make it easier to visualize a potential future state which is good for the investment business. In tourism and in the real-estate area, 3D models make it easier to imagine space and orientation. A 3D model designed for professional users (planners) must emphasize the accuracy (geometric and attributive) and the required level of detail, while a 3D model intended for non-professional users (tourists, investors, real estate buyers, etc.) must have an accent on appearance. An exception to this rule is when a 3D model is created as a background for visualizing a future project, for example, when architects design a future building and want to visualize it together with the environment. It is then important that the existing condition around the plot on which it is built is accurate and looks nice, as the architect will "build" his building on that 3D model of an existing state that must be graphically and in detail aligned with the visualization of the building [1].

2 PREVIOUS WORK

3D cadastre refers to a cadastral system that represents the legal status of a property, not just the 2D cadastral parcels, but the 3D legal units with the rights, responsibilities and unique and homogenous constraints [2, 3]. The development of an efficient 3D cadastral system includes the consideration of several legal, institutional and technical aspects [3, 4]. The basic factors of the 3D cadastre are properties, buildings and other constructions, special parts of properties, ores and other underground natural resources, as well as the public utility infrastructure. The amount and complexity of data that are kept on the basis of regulations in public authorities are constantly increasing. This process is conditioned by the development of technology and takes place alongside it. The list of opportunities offered by new technologies is steadily increasing. The adoption of technological achievements,

particularly in the field of information-communication technologies, and their implementation in the enrolment systems facilitated the maintenance, access and exchange of data. This opens the possibility of collecting some new, additional data that had not been previously collected because their maintenance was technically overwhelming [5].

The pressure on the construction of buildings, especially in city centres and on the seashore, has led to a dense construction of complex buildings. These structures are intertwined. As a rule, the enrolment of rights to parts of buildings is enabled, and the spatial display of the extension does not usually exist [6]. An increasing number of tunnels, infrastructure facilities (plumbing, gas pipeline, electric and other grids) located below or above the land, and not owned by the landlord, require a better description and enrolment in the public registers of such facilities.

As far as the technical aspects are concerned, the 3D data collection, 3D data modelling, and 3D database management systems are factors in the development of 3D cadastral applications. However, 3D visualization plays a significant role and is recognized as an issue of extreme importance in several international workshops (1st, 2nd and 3rd International Workshop on 3D Cadastre) by several authors [7, 8].

Visualization systems are necessary not only to display the physical objects but also to visualize their legal parts. Legal parts may be of limited or unlimited volume [9]. For the cadastre, several specific prototypes have been proposed, such as the spatial databases with CAD and GIS access-parts [3, 8, 10-14]. On the other hand, the technological advancement and the ease of use of web application visualization have made them very popular among users. This popularity has led to the construction of several 3D visualization prototypes using web technologies [15-21], although they still require the maturation and confirmation by users, so that they can be used in real life situations. Thus, 3D visualization for the cadastre requires further research [22, 7].

2.1 Procedural Modelling

The best method for creating a large 3D city model in a short time and at a low cost is procedural modelling, which means creating 3D models using rules and algorithms. It is an economical solution for generating 3D urban content [23]. The procedural modelling software from Esri called CityEngine is mainly used to create 3D urban area models. Modelling is based on CGA (Computer Generated Architecture) rules. CGA is a scripting language suitable for creating architectural 3D content [24]. Previous research in this area have shown that CityEngine is suitable for modelling cities. CityEngine is a three-dimensional (3D) modelling software developed by Esri R & D Center Zurich (formerly Procedural Inc.) and specializes in creating 3D urban environments. With procedural approaches to modelling, CityEngine enables you to efficiently create a detailed 3D city model displayed in a large scale in just a few mouse clicks instead of a long-lasting and exhausting way of creating and manually setting objects [25].

2.2 3D Visualization

The focus of this paper is primarily on 3D visualization, not on data management or data delivery. Van Oosterom [22] stated that "visualization and/or interaction with 3D cadastral particles requires more attention and can be quite different from the more familiar visualization, e.g. 3D city models", and added: "Some specific key points are as follows:

- (1) how to visualize dense 3D volumes such as in complex buildings because the first visible outer layer of 3D space unit blocks the look of others;
- (2) how to display open or unlimited particles,
- (3) how to include the Earth's surface and / or other reference objects (e.g. as CityGML) into a 3D cadastre,
- (4) how to display underground infrastructure."

Shojaei [15] proposed a set of conditions that should meet 3D cadastral visualization systems and tested them on several visualization systems to determine to what extent they implemented the necessary preconditions. They also reviewed several common 3D visualization solutions.

3D models created in CityEngine have different applications, for example, in cultural heritage, urban planning and film industry. Procedural modelling can be applied to the creation of 3D video content [23]. Research by Radies describes the principle of 3D modelling of buildings using gradual modelling procedures in the CityEngine software. The basis of procedural modelling is based on form grammar with production rules to generate detailed 3D objects from simple initial geometric features. It begins with the extrusion of the initial shape on a model that is later divided into shapes, for example, facades and roofs. To create a detailed high-level model, the created shapes are divided into elements, for example, windows and doors, and textures or colors, and added to these elements.

In order to create better and more realistic 3D urban content, several suggestions have to be made, as Watson [23] said: "Urban content is a little more than building a shape." Creating a real-time impact on urban content and wear

elements can be applied to materials and models, for example, the accumulation of rust and dirt. The model of the city looks more realistic if there are cars and pedestrians in it.

3 CITYENGINE

CityEngine is a standalone computing application for designing, planning and modelling urban environments in 3D. It was designed to help professional users in GIS, CAD and 3D systems to:

- quickly generate 3D cities from the existing 2D GIS data;
- realize conceptual design in 3D based on the GIS data and procedural rules;
- model virtual 3D urban environments for simulation and entertainment.

Consequently, experts that are using CityEngine come from the following industries: urban planning, design and development (architectural design and local government); entertainment (movies, commercials, video games); simulation of the real world (Fig. 1), emergency services and defence; and, of course, education.



Figure 1 Scene from software supporting procedural modelling [26]

The main concept of CityEngine is the "procedural" approach to modelling. The computer is a code that represents a number of commands - in this context, geometric modelling commands - which will then be executed. Instead of "classical" user intervention, i.e. manual interaction with the model and 3D geometry modelling, the task is described as "abstract" in the "rule" file. Commands available in the CGA shape grammar format of CityEngine such as "extrude", "split" or "texture" are widely-known commands in most 3D applications so that each user can easily adopt and create complex architectural shapes in a relatively short period of time [26].

One "rule" file can be used to generate many 3D models. For example, the rule may use information about attributes stored in the GIS data such as the number of floors, floor height, roof type, wall material type, etc. - to generate a range of alternative 3D models that accurately represent the properties of each feature. The more attributes you have, the more accurate the model can be. The 3D model is nothing more than a 3D object that is the result of an extruded 2D form according to the rules defined in the CGA "rule" file. The origin of these 2D forms is variable:

- it can be imported from Esri Shapefiles or File Geodatabase;
- it can be manually build in CityEngine;
- it can be generated through CGA rules.

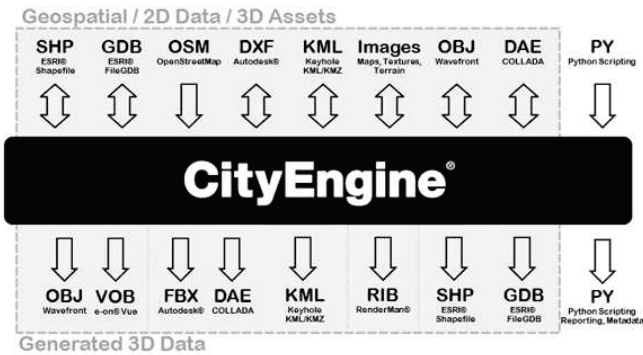


Figure 2 CityEngine Software Input and Output File Formats [26]

Three-dimensional objects represented in CityEngine do not have to be all generated within CityEngine. They can be downloaded through the formats shown above in Fig. 2. However, only the geometry of objects from the multiple Esri Shapefiles or File Geodatabase can be edited and later upgraded to the original files. 3D models are 3D objects generated in CityEngine through procedural modelling. The remaining objects (3D or 2D) are called Shapes. By changing the urban design (i.e. by regenerating the "regenerate") commands, they are automatically applied and updated [26].

The next advantage of CityEngine is the variety of data formats supported for import and export. CityEngine supports geographic data, 2D data, 3D data (polygonal networks) and Python scripting as input data types and offers a wide variety of formats for exporting 3D data. The further advantage of procedural modelling is its ability to dynamically edit. For example, when importing a street network, the software generates plots inside the street and 3D buildings are generated inside the parcel, and if the street is moved, then the buildings are also moved because they are procedurally associated [26].

The lack of procedural modelling compared to manual modelling techniques is less "user-friendliness" [27]. The knowledge of CGA scripting for writing proper files makes the process of procedural modelling more complex at the beginning if the user has no experience with it.

3.1 A tool for Procedural 3D Modelling

The main idea behind CityEngine is to create an urban environment from scratch. At the very beginning of the project, central street lines are usually generated based on pre-programmed chart algorithms whose value can be changed by the user. These street lines close the 2D polygons representing the cadastral particle (2D particle). In both cases, the user can modify the values of the parameters used. In the third stage, the buildings are built in 3D, based on the CGA "rule" file, which contains data on the number of floors, heights, type of roof, color and texture. 3D buildings can be generated directly from the particle, citing, for example, the

offsets or pre-loaded 2D floor planes. At this stage, vegetation, water, vehicles, furniture, etc., can also be generated based on the CGA rules. Infrastructures above and below the Earth's surface are also represented at this stage. If needed, the created urban environment can be loaded into another software specializing in 3D visualization, presentation or analysis (e.g. ArcGIS, Maya, 3ds Max, Google Earth, Unity, Unreal, RenderMan and RealityServer) [28].

For some imported 3D objects, you may only need to change the display mode (color, thickness, transparency, texture, etc.). In the case of 2D objects, it is necessary to further define the CGA rules that are based, for example, on the attributes from the GIS attribute table. Another important feature of CityEngine is the fact that, in the case of features from the Geodatabase file, the existing relationships between the tables are imported. They can be viewed and searched through a code (CGA rules or Python). Let us assume that apartment A, located at level L of building B located on plot P, is owned by O1 and O2. If these relationships are modelled in the File Geodatabase, then the Inspector Window will show information about the physical 3D object "Apartment A". The attribute "Owner" of the object "Apartment A" will appear in the form of a list, as there are two owners - O1 and O2 [28].

Programming in Python can also present great flexibility in the workflow. By programming in Python, it is possible to define which objects must belong to each layer. For example, if there is interest in separate legal objects, by placing them in different layers, they can later be separately controlled for their visibility. Especially in the case of separation of flats per floor, laying a layer for each floor. Moreover, attribute queries can only be made by programming in Python. For example, to select all multi-owner objects, and then create a layer with that information or export them to a text file in the form of a report [28].

According to Watson [23], Esri CityEngine is one of the most prominent procedural modelling tools available. It is a standalone software that transforms 2D GIS data into smart 3D cities models. This improves urban planning, architecture and design. CityEngine combines 3D modelling and grammatical modelling methods to generate 3D content. Shape grammar recognizes certain shapes and its possible substitutes. The forms that are to be replaced and the way in which this will be executed are listed in the rules. Split grammar divides the 3D object into its components, for example, the front facade, edges or peaks.

For a successful use of the form and split grammar in the modelling process, the following two steps should be taken into account and implemented. The first step is gaining a good understanding of basic building elements such as windows, doors, pillars, walls and others. The next step is to create grammatical rules for combining these basic elements [23].

Typical modelling sessions include steps shown in Fig. 3.

Some of the elements needed for city modelling in CityEngine are the terrain, controlled map layers, street networks, building blocks and CGA "rule" files. Street

network and floor plans can be automatically or manually created in CityEngine or imported from DXF and SHP files [27].

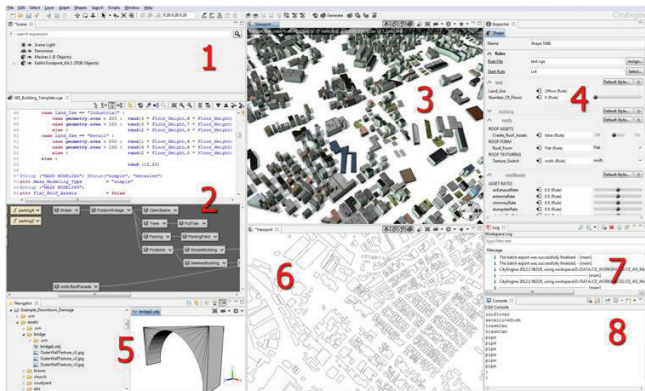


Figure 3 Windows in the CityEngine software

The CGA (Computer Generated Architecture) script that defines the rules or procedures for creating 3D content is the core of this software. CityEngine can be used for the entire developmental cycle of procedural modelling, as it includes scenes with the already existing data, modelling street geometry, writing and analyzing CGA script files, applying CGA files to create 3D models, and exporting created models for further processing.

The two primary properties that link the initial form to the generation process are the "Rule file" that defines that the correct CGA file assigned to the initial form, and the "Start rule" that defines the production rule from which the process of creation begins. Other attributes that describe the initial form (e.g. height of building, number of floors, roof shapes, etc.) can be used as parameters in the CGA rule file [29].

The advantage of CityEngine is the easy option of creating 3D urban scenes based on the existing GIS data. High-quality 3D content can be created with only a combination of 2D data, attributes, and procedurally defined rules. The components of CityEngine are geometry, attributes, and procedurally defined rules.

The complexity and actual accuracy of the generated model depends on the amount of detail envisaged for each component. When 3D city content is generated using the parameter rules, it is possible to create a 3D city design and further analysis (for example, visibility and shadow analysis) of the model. In short, creating a 3D city model in CityEngine can be done in 5 steps:

- First of all, there should be a 2D Geodatabase or 2D GIS data, CAD data or data of other formats that will be imported into CityEngine.
- After import, GIS data can be edited and manipulated. This step involves 3D streets, blocks and parcel creation.
- The next step involves 3D extrusion of buildings, production of roofs, street furniture and other elements in the model.
- After the model is made, the next step includes the in-depth detailing of the model details using procedural rules, the selection of detail levels (LoD) and the addition of vegetation.

- The last step of the process is to export the created city model to another 3D application. It can be displayed in another application, exported to a video game, and shared online using the Esri WebScene. It is also possible to export the created models back to the Geodatabase file for a more accurate 3D analysis in ArcScene [30].

4 APPLICATION OF PROCEDURAL MODELLING IN THE TEST AREA

The test area includes 95 buildings in the Ilica street (Zagreb) from the Ban Jelačić Square to the British Square. For building a 3D model of a building, the Shapefile of the floor plan (Fig. 4) was used with attribute information about the building height. The files have been provided by the GDIGISDATA in Zagreb. Shapes were initially in the old Croatian coordinate system of HDKS. They were transformed using an open source software of QGIS into the official Croatian coordinate system of HTRS96.

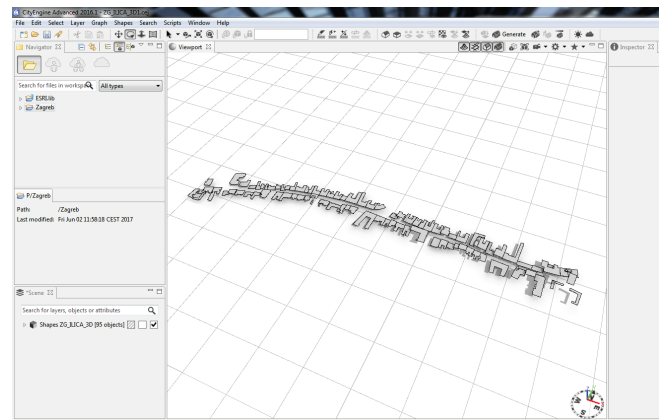


Figure 4 Source data uploaded and visualized to Esri CityEngine

For a more realistic scene, a DRM (Digital Relief Model) was used. It was downloaded with a spatial resolution of 1 arc-second from the free web service: <https://asterweb.jpl.nasa.gov/gdem.asp>. Since CityEngine has no ability to load DMRs in the form of grid points, by using the open source software SAGA GIS, a shaded relief view was created as a geotiff image and loaded into CityEngine.

4.1 Set of CGA Rules

The definition of the CGA set of rules follows once all the required data has been collected. Attributes that are different for each building are defined. These are the height of the building, ground floor height, height of the floor, width of walls on the buildings, facade texture, type of entrance door, window, floor and the type and texture of the roof. In this case, the height of the building and the texture of the facade are given for each shape according to their ID. Entrance doors, sliding doors and windows are the same in all buildings due to the shrinking workload. The roof type is also the same for all buildings, but the texture of the roofs is assigned by the "random" function that randomly assigned

the texture of each building between 6 different textures of red and gray bricks to mimic the appearance of the DOF (digital orthophoto) building (Fig. 5).



Figure 5 Roof textures assigned by the "random" method



Figure 6 Problem of roof modelling



Figure 7 Problem of roof modelling

The height of the floors and the width of the windows defining the number of windows on the facade were changed in the Inspector Window of CityEngine according to the information obtained from the photo of the building. The "extrude" function generated the height of the building, which is then divided into the front facade and all the other facades and the roof. The width of the floors on the ground floor and the ground floor are defined where the ground floor is marked as a fixed floor, and where the floors are "floating", meaning that they are repeated to infinity on the same pattern. The type of the roof (RoofHip), as well as the roof gradient (20°) were also defined. Since a roof with a gradient of 0.5 m above the edge of the facade was defined, the problem with roof modelling was that the facade wall "cut" the roof on the edges (Fig. 6). This problem has been solved by the code line $t(0, 0, 0, 15)$, which projected the roof by 15 cm in the y axis direction, thus avoiding the overlapping with the walls (Fig. 7).

Generating the window and door on the edges with other objects is disabled by using the code:

Window → case touches: Wall

Door → case touches: Wall



Figure 8 Viewing a 3D model of a part of the city of Zagreb



Figure 9 Facade bends

The balcony, different facade tiles (Fig. 9), and the decorative elements on the facade have not been modelled, since for this level of modelling in CityEngine, a polygonal rather than a procedural type of modelling is foreseen.

Finally, the 3D model of buildings was developed to the LOD 2 level of detail (Fig. 8).

The entire set of rules used for modelling buildings can be seen on the web at [31].

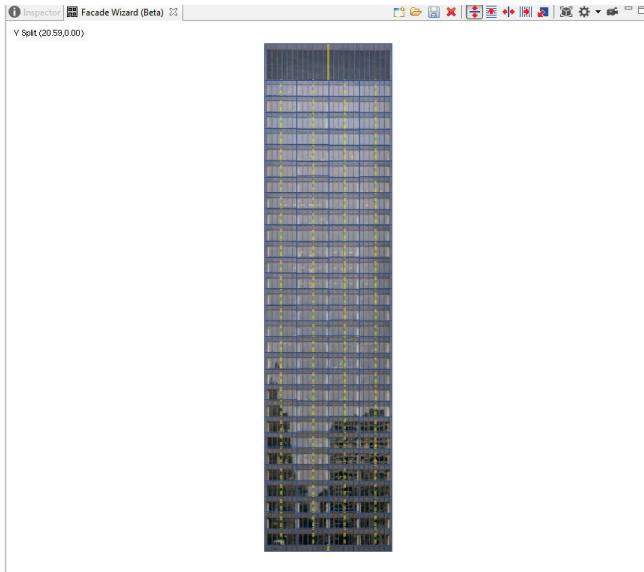


Figure 10 Distribution of the facade on the floors and surfaces in Facade Wizard

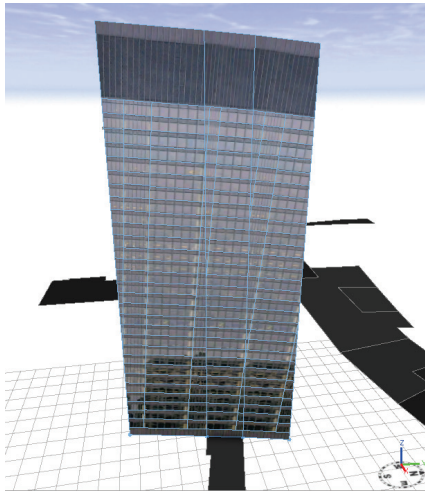


Figure 11 Result obtained with the Facade Wizard

After all the LOD 2 level buildings were built, we decided to manually create the Ilica skyscraper, since it is the only building with its shape and modern architecture to stand out from the rest of the buildings built in the late 19th and early 20th centuries. For creating the skyscrapers, the Facade Wizard was used. This tool creates a 3D model based on a facade photograph. Unfortunately, the Facade Wizard was not able to take a photograph of the skyscraper that covered the whole building which is why the texture, looking as a hyphen skyscraper, was downloaded from the Esri library. The Facade Wizard functions in a way that the facade is divided into functional and aesthetic elements, which are then given a "fixed" or "floating" value, as well as a z-component (i.e. the descent or ascent in the facade) (Fig. 10). As the obtained results were not satisfying (Fig. 11), we had to use a tool for automatic error correction - Shape Cleanup.

Fig. 12 and Fig. 13 show the results of skyscraper modelling in the Ilica street, as well as a comparison of a scene from CityEngine.



Figure 12 Skyscraper in the Ilica street - photo



Figure 13 Skyscraper in the Ilica street - 3D model obtained as result of automatic procedural modelling

When modelling the facade based on an image, the main problem in the process is to generate a credible 3D model with semantic information from one input image. The process consists of four phases:

- 1) Detection of facade structure - an agitation that automatically divides the facade image onto floors and surfaces.
- 2) Definition of the surface - this is the phase in which the planes are divided into smaller regions. The method recursively selects the best splitting line of a given surface. The division of the structure is a common concept in procedural modelling [32, 33] and gives the hierarchy elements.
- 3) Element Identification - the procedure for matching the elements obtained by the previous step with a huge library of 3D objects.
- 4) Editing and extraction of the grammatical set of rules - at this stage of interpretation, the facade is encoded as a tree shape. Due to the lack of depth information, it is necessary to edit the depth of facade elements to improve the visual perception.

This method can be used for urban reconstruction or reconstruction of facades if original images have an appropriate quality. The full resulting programmed code can be found at [31]. The finished 3D model of a single street in the city of Zagreb is shown in Fig. 14. The 3D model consists of 95 buildings in the Ilica street (Zagreb) from the Ban Jelačić Square to the British Square.

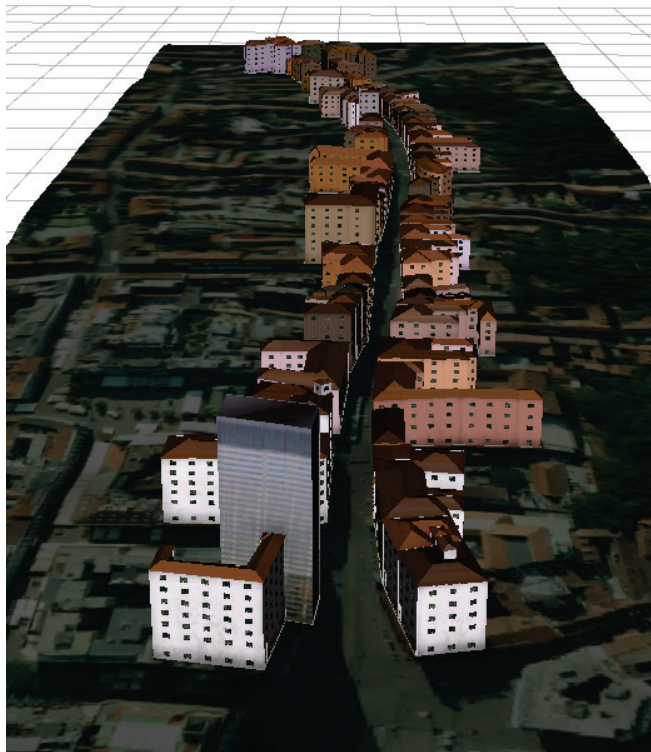


Figure 14 Finished 3D model of a part of the city of Zagreb

5 CONCLUSIONS

In this paper, it is shown that there is no need for expensive solutions and a new software for procedural 3D modelling (because there is no software for automatic 3D modelling so far). The software used in this research is a tool for generating 3D models from 2D GIS data and it was programmed to do that automatically. However, following the fundamental policy of procedural modelling, namely that one rule applies to a large number of buildings or entire cities, one cannot obtain a satisfactory and completely faithful representation of buildings. In case we want a more detailed view of buildings with all ornamental details on the facade, or at least a model that can be used to calculate the volume or the grossly developed surface which contains all balconies, terraces, etc., we need to write a special code for each building and in most cases, further elaborate details on the object using a polygonal modelling tool. For areas and cities where buildings differ in the architectural aspect, procedural modelling only further complicates and extends the modelling process. As shown in this work, procedural modelling is the best choice for creating a LOD1 building model of large areas or LOD2 building model for areas where buildings resemble one another. Furthermore, what CityEngine is missing are spatial analysis tools, including the simpler ones such as length measurements. However, this can be solved by having the 3D model exported and loaded into another software after making it in postprocessing.

Procedural modelling, once adopted, becomes a quick and effective way to generate 3D low to mid-level detail models. These models can be very useful in the field of urban planning, in the design of bases for smart cities, as a subject of visualization for tourist purposes and in many other areas. By building a 3D model of objects that surround us, we are making a step forward in the development of virtual reality.

6 REFERENCES

- [1] Gorički, M. (2015). Modeliranje 3D kartografskog prikaza za potrebe planiranja pametnih gradova, *Diploma thesis*, Sveučilište u Zagrebu, Geodetski fakultet.
- [2] van Oosterom, P. (2012). Summary of the Third International FIG Workshop on 3D Cadastres—Developments and Practices. In *Third International FIG Workshop on 3D Cadastres—Developments and Practices*, Shenzhen, China. http://www.gdmc.nl/3dcadastres/literature/3Dcad_2012_30.pdf (23.06.2017)
- [3] Stoter, J. E. (2004). 3D cadastre. *PhD Thesis*, TU Delft, Delft, Nizozemska.
- [4] Pouliot, J., Vasseur, M., & Boubehrezh, A. (2011, November). Spatial representation of condominium/co-ownership: comparison of Quebec and French cadastral system based on LADM specifications. In *2nd International Workshop on 3D Cadastres*.
- [5] Mađer, M. (2012). Model of linking cadastre with related registers, *Doctoral dissertation*, Geodetski fakultet, Sveučilište u Zagrebu.
- [6] Roić, M. (2012). *Upravljanje zemljišnim informacijama-katastar*. Sveučilište u Zagrebu, Geodetski fakultet. ISBN 978-953-6082-16-2, Zagreb.

- [7] Pouliot, J., Vasseur, M., & Boubehrezh, A. (2011, November). Spatial representation of condominium/co-ownership: comparison of Quebec and French cadastral system based on LADM specifications. In *2nd International Workshop on 3D Cadastres*, 274-289.
- [8] Aditya, T., Iswanto, F., Wirawan, A., & Laksono, D. P. (2011, November). 3D cadastre web map: Prospects and developments. In *2nd International workshop on 3D cadastres*, 16-18.
- [9] Lemmen, C., Van Oosterom, P., Thompson, R., Hespanha, J. P., & Uitermark, H. (2010). The modelling of spatial units (parcels) in the Land Administration Domain Model (LADM).
- [10] Rahman, A. A., Hua, T. C., & Van Oosterom, P. (2011, May). Embedding 3D into multipurpose cadastre. In *FIG working week*.
- [11] Billen, R., & Zlatanova, S. (2003). 3D spatial relationships model: a useful concept for 3D cadastre? *Computers, Environment and Urban Systems*, 27(4), 411-425. [https://doi.org/10.1016/S0198-9715\(02\)00040-6](https://doi.org/10.1016/S0198-9715(02)00040-6)
- [12] Hassan, M. I., Ahmad-Nasruddin, M. H., Yaakop, I. A., & Abdul-Rahman, A. (2008). An integrated 3D cadastre—Malaysia as an example. *The International Archives of the Photogrammetry, Remote Sensing and Spatial Information Sciences*, 37(B4), 121-126.
- [13] Stoter, J. E., & Ploeger, H. D. (2003). Property in 3D—registration of multiple use of space: current practice in Holland and the need for a 3D cadastre. *Computers, Environment and Urban Systems*, 27(6), 553-570. [https://doi.org/10.1016/S0198-9715\(03\)00014-0](https://doi.org/10.1016/S0198-9715(03)00014-0)
- [14] Shen, Y. I. N. G., Renzhong, G. U. O., & Lin, L. I. (2011, November). Design and Development of a 3D Cadastral System Prototype based on the LADM and 3D Topology. In *The 2nd International Workshop on 3D Cadastres*, Delft, The Netherlands.
- [15] Shojaci, D., Kalantari, M., Bishop, I. D., Rajabifard, A., & Aien, A. (2013). Visualization requirements for 3D cadastral systems. *Computers, Environment and Urban Systems*, 41, 39-54. <https://doi.org/10.1016/j.compenvurbsys.2013.04.003>
- [16] Dimovski, V., Bundaleska-Pecalevska, M., Cubrinovski, A., & Lazoroska, T. (2011, November). WEB portal for dissemination of spatial data and services for the needs of the agency for real estate cadastre of the Republic of Macedonia (AREC). In *2011 International Workshop on 3D Cadastres*, 6-18.
- [17] Vandysheva, N., Tikhonov, V., Van Oosterom, P. J. M., Stoter, J. E., Ploeger, H. D., Wouters, R., & Penkov, V. (2011). 3D Cadastre modelling in Russia. In *Proceedings of the FIG Working Week 2011 " Bridging the Gap between Cultures" & 6th National Congress of ONIGT*, Marrakech, Morocco, 18-22 May 2011. International Federation of Surveyors (FIG); Ordre National des Ingénieurs Géomètres Topographes (ONIGT).
- [18] Ying, S., Guo, R., Li, L., & He, B. (2012). Application of 3D GIS to 3D Cadastre in Urban Environment. *3rd International Workshop on 3D Cadastres: Developments and Practices*, 25-26.
- [19] Guo, R., Li, L., He, B., Luo, P., Ying, S., Zhao, Z., & Jiang, R. (2011, November). 3D cadastre in China—a case study in Shenzhen City. In *Proceedings of 2nd international workshop on 3D cadastres*, Delft, The Netherlands, 16-18.
- [20] Coors, V. (2003). 3D-GIS in networking environments. *Computers, Environment and Urban Systems*, 27(4), 345-357. [https://doi.org/10.1016/S0198-9715\(02\)00035-2](https://doi.org/10.1016/S0198-9715(02)00035-2)
- [21] Stoter, J., & Salzmann, M. (2003). Towards a 3D cadastre: where do cadastral needs and technical possibilities meet? *Computers, environment and urban systems*, 27(4), 395-410. [https://doi.org/10.1016/S0198-9715\(02\)00039-X](https://doi.org/10.1016/S0198-9715(02)00039-X)
- [22] van Oosterom, P. (2013). Research and development in 3D cadastres. *Computers, Environment and Urban Systems*, 40, 1-6. <https://doi.org/10.1016/j.compenvurbsys.2013.01.002>
- [23] Watson, B., Müller, P., Veryovka, O., Fuller, A., Wonka, P., & Sexton, C. (2008). Procedural urban modelling in practice. *IEEE Computer Graphics and Applications*, 28(3), 18-26. <https://doi.org/10.1109/MCG.2008.58>
- [24] Parish, Y. I. & Müller, P. (2001, August). Procedural modelling of cities. In *Proceedings of the 28th annual conference on Computer graphics and interactive techniques*, ACM, 301-308.
- [25] See <http://en.wikipedia.org/wiki/CityEngine> (23.06.2017)
- [26] See <http://www.esri.com/software/cityengine> (23.06.2017)
- [27] Piccoli, C. (2013). CityEngine for Archaeology. In Amsterdam: 3D GIS for mapping the Via Appia.
- [28] Ribeiro, A., Duarte De Almeida, J., Ellul, C. (2014): Exploring CityEngine as a Visualisation Tool for 3D Cadastre, Dubai, United Arab Emirates.
- [29] Viinikka, J. (2014). Adopting Procedural Information Modelling in Urban Planning. Aalto University.
- [30] <http://www.youtube.com/watch?v=zScyrwQLf0k> (23.06.2017)
- [31] <http://mojoblak.srce.hr/public.php?service=files&t=9601bd0acec842acddb1479b996ac15> (15.06.2018)
- [32] Müller, P. et al. (2006). Procedural Modelling of Buildings. *ACM Transactions on Graphics - Proceedings of ACM SIGGRAPH*, 25(3), 614-623. <https://doi.org/10.1145/1141911.1141931>
- [33] Wonka, P., Wimmer, M., Sillion, F., & Ribarsky, W. (2003). Instant architecture. In *ACM SIGGRAPH*, New York, NY, USA.

Authors' contacts:

Robert ŽUPAN, Assoc. Prof.
Faculty of Geodesy
Kačićeva 26, 10000 Zagreb, Croatia
01/4639-184, rzupan@geof.hr

Katarina ŽUPAN, mag. Ing. geod & geoinf.
Faculty of Geodesy
Kačićeva 26, 10000 Zagreb, Croatia
kzupan@geof.hr

Stanislav FRANGEŠ, Full Time Prof.
Faculty of Geodesy
Kačićeva 26, 10000 Zagreb, Croatia
01/4639-231, sfranges@geof.hr

Adam VINKOVIĆ, mag. ing. geod. et geoinf.
Faculty of Geodesy
Kačićeva 26, 10000 Zagreb, Croatia
01/4639-381, avinkovic@geof.hr

LOW POWER STEAM TURBINE ENERGY EFFICIENCY AND LOSSES DURING THE DEVELOPED POWER VARIATION

Vedran MRZLJAK

Abstract: This paper investigates low power marine steam turbine during the variation in its developed power. The turbine is used for the Main Feedwater Pump (MFP) drive. Energy analysis of the Main Feedwater Pump Turbine (MFPT) is based on the measurements performed in nine different operating regimes. The measured operating parameters were steam pressure and temperature at the turbine inlet, steam pressure at the turbine outlet, and a water volume flow through MFP. Turbine energy power losses are most influenced by steam mass flow through the turbine and by steam specific enthalpy at the turbine outlet. An increase in turbine developed power causes a continuous increase in turbine energy efficiency. Analyzed turbine is balanced as most of the other steam system components – maximum energy efficiency will be obtained at the highest load, on which the majority of turbine and system operation can be expected during exploitation.

Keywords: energy efficiency; energy power losses; power variation; low power steam turbine

1 INTRODUCTION

Unlike the majority of marine transport in which diesel engine propulsion is dominant, steam propulsion systems are still used in the most of LNG carriers due to several important facts [1]. One of the most important reasons for steam propulsion system usage on LNG carriers is that the steam generators are capable of burning the entire amount of BOG (Boil-Off Gas) which occurs in LNG tanks. Each steam propulsion system consists of a large amount of components necessary for safe and reliable operation [2, 3].

In such a steam propulsion system, the main high pressure feed water pump is an important element – it returns water from the deaerator to steam generator and increases its pressure (usually through one or more high-pressure feed water heaters [4]). In most of the steam propulsion systems, the main high pressure feed water pump is traditionally driven by the low power steam turbine. In this paper, the Main Feedwater Pump Turbine (MFPT) is analyzed from the aspect of energy efficiency and energy power losses during the variation in turbine developed power. The measurements of MFPT steam operating parameters along with water volume flow through the Main Feedwater Pump (MFP), which are necessary for turbine numerical analysis, were made on a conventional LNG carrier during exploitation for a number of MFPT loads. The main characteristics and specifications of the LNG carrier in which the steam propulsion system is mounted and MFPT analyzed are presented in Table 1.

MFPT is a low power steam turbine, which consists of a single Curtis stage. Steam turbines with Curtis and other stages along with their complete analysis can be found in [5] and [6]. Many details of the classic and specific designs of marine steam turbines and their auxiliary systems are presented in [7] and [8].

The main goal of the MFPT analysis was to present change in the steam turbine energy efficiency and energy power losses during the change in turbine developed power.

In each presented turbine operating point the turbine developed power was varied from the lowest value of 50 kW up to the maximum power of 570 kW in steps of 20 kW. During the power variation, turbine energy efficiency and energy power losses were calculated. The results of the analysis were presented for three randomly selected turbine operating points, but the presented conclusions are valid also for all the other operating points. In each operating point steam turbine developed power variation allows detecting optimal turbine loads with the highest energy efficiency. Turbine energy efficiency and energy power losses were compared from the real exploitation with achieved optimal ones. MFPT load depends on current water mass flow through the high pressure feedwater pump; from the aspect of energy efficiency, it is optimal for this turbine to constantly operate at the highest load (at 570 kW) in each observed operating point. Turbine energy power losses are not the lowest at the highest turbine load; the lowest energy power losses were obtained at 37% of maximal turbine power (at 210 kW) in each observed operating point.

Table 1 Main characteristics and specifications of the LNG carrier

Dead weight tonnage	84.812 DWT
Overall length	288 m
Max breadth	44 m
Design draft	9.3 m
Steam generators	2 × Mitsubishi MB-4E-KS
Propulsion turbine	Mitsubishi MS40-2 (max. power 29.420 kW)
Turbo-generators	Shinko RGA 92-2 (max. power 3.850 kW each)

2 EQUATIONS FOR THE MFPT ENERGY ANALYSIS

2.1 General Equations for the Turbine Energy Analysis

Energy analysis of any steam system component is defined by the first law of thermodynamics, which is related to the conservation of energy [9]. Mass and energy balance, Eq. (1) and Eq. (2), for a standard volume in steady state disregarding potential and kinetic energy can be expressed according to [10] and [11] as

$$\sum \dot{m}_{IN} = \sum \dot{m}_{OUT} \quad (1)$$

$$\dot{Q} - P = \sum \dot{m}_{OUT} \cdot h_{OUT} - \sum \dot{m}_{IN} \cdot h_{IN} \quad (2)$$

Flow energy power for any fluid stream (in this analysis, steam stream through the turbine) can be calculated according to the [12] using Eq. (3)

$$\dot{E}_{en} = \dot{m} \cdot h \quad (3)$$

Energy efficiency, Eq. (4), can usually be written as [13]

$$\eta_{en} = \frac{\text{Energy output}}{\text{Energy input}} \quad (4)$$

with the remark that energy efficiency can take different forms depending on the type of the system (or the system component if the energy analysis is performed just for one component).

2.2 MFPT Energy Efficiency and Energy Power Losses

Main Feedwater Pump steam Turbine (MFPT) is directly connected to the Main Feedwater Pump (MFP) which is used for increasing the water pressure and returning it to the steam generators, as shown in Fig. 1. MFPT consists of a single Curtis stage, while the whole unit has the following specifications [14]:

- pump delivery height: 818 m
- pump maximum capacity: 175 m³/h
- steam turbine maximum power: 570 kW.

In Fig. 1, steam mass flow through MFPT (\dot{m}_{MFP}) is presented together with steam specific enthalpy and steam specific entropy at the turbine inlet and outlet. An important and measured operating parameter of the main feedwater pump, which will be used in the calculation of MFPT developed power, is pump water volume flow (\dot{V}_{MFP}).

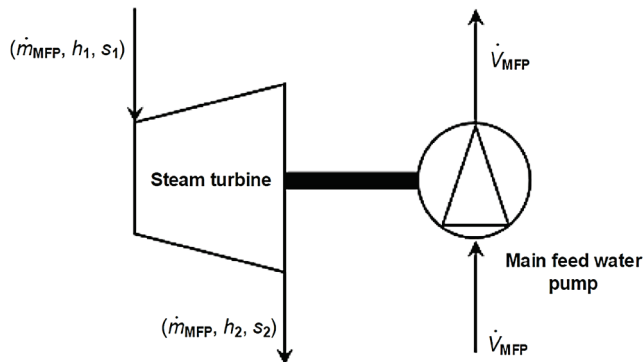


Figure 1 Change of main operating parameters through the analyzed turbine, which drives the high pressure pump

MFPT developed power was approximated from the pump water volume flow (\dot{V}_{MFP}) by using third degree

polynomial, Eq. (5), according to the producer specifications [14]. Main feed water pump water volume flow in relation to the MFPT developed power was calculated for medium water density $\rho_{fw} = 937.48 \text{ kg/m}^3$ at a water temperature of $T_{fw} = 127 \text{ }^\circ\text{C}$, according to the producer recommendations. MFPT developed power was calculated as follows:

$$P_{MFPT} = 1.786 \times 10^{-5} \cdot \dot{V}_{MFP}^3 - 3.089 \times 10^{-3} \cdot \dot{V}_{MFP}^2 + 2.002 \cdot \dot{V}_{MFP} + 189.48 \quad (5)$$

where P_{MFPT} was obtained in kW when \dot{V}_{MFP} in m³/h was placed in the Eq. (5).

Steam mass flow through MFPT was approximated with the turbine produced power P_{MFPT} . Approximation was made according to the producer specifications [14], by using third degree polynomial, Eq. (6):

$$\dot{m}_{MFP} = -3 \times 10^{-5} \cdot P_{MFPT}^3 + 3.133 \times 10^{-2} \cdot P_{MFPT}^2 - 4.397 \cdot P_{MFPT} + 2386.6 \quad (6)$$

where \dot{m}_{MFP} was obtained in kg/h when P_{MFPT} in kW was placed in the Eq. (6).

During the measurements steam leakage on the MFPT was not observed, so the mass balance for the MFPT inlet and outlet, Eq. (7), is as follows:

$$\dot{m}_{MFP,1} = \dot{m}_{MFP,2} = \dot{m}_{MFP} \quad (7)$$

According to Fig. 1 and Fig. 2, h_1 is steam specific enthalpy at the turbine inlet and h_2 is steam specific enthalpy at the turbine outlet after real (polytropic) expansion. Steam specific enthalpy at the turbine inlet (h_1) as well as steam specific entropy at the turbine inlet (s_1) were calculated from the measured steam pressure and temperature at the turbine inlet. Steam specific enthalpy at the turbine outlet (h_2) was calculated from the MFPT developed power P_{MFPT} in kW and from steam mass flow through the turbine \dot{m}_{MFP} in kg/s according to [15], using an Eq. (8):

$$h_2 = h_1 - \frac{P_{MFPT}}{\dot{m}_{MFP}} \quad (8)$$

The steam specific entropy at the turbine outlet (s_2) was calculated from steam specific enthalpy at the turbine outlet (h_2) and measured pressure at the turbine outlet (p_2).

Specific enthalpy after isentropic steam expansion (h_{2s}) was calculated from the measured steam pressure at the turbine outlet (p_2) and from the known steam specific entropy at the turbine inlet (s_1). Ideal isentropic expansion assumes no change in steam specific entropy ($s_1 = s_{2s}$), as presented in Fig. 2. The complete turbine energy analysis presented in this

paper is based on comparison of real (polytropic) steam expansion and ideal (isentropic) steam expansion.

Steam specific enthalpy at the turbine inlet (h_1), steam specific enthalpy at the end of turbine isentropic expansion (h_{2s}), and both steam specific entropies (at the turbine inlet s_1 and outlet s_2) were calculated by using NIST REFPROP 8.0 software [16].

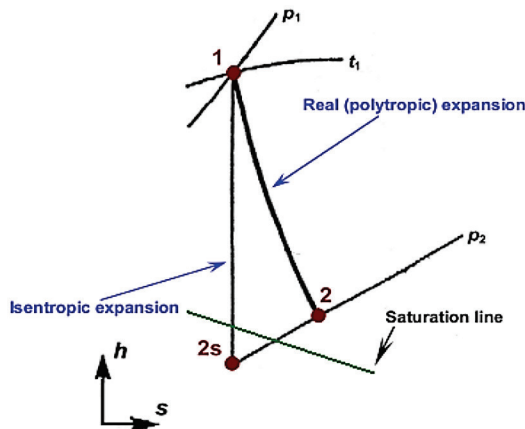


Figure 2 Turbine real (polytropic) and ideal (isentropic) expansion

MFPT energy power losses, Eq. (9), in each turbine operating point can be calculated according to Fig. 2 as:

$$\dot{E}_{MFPT,en,PL} = \dot{m}_{MFP} \cdot h_2 - \dot{m}_{MFP} \cdot h_{2s} = \dot{m}_{MFP} \cdot (h_2 - h_{2s}) \quad (9)$$

Energy efficiency of MFPT can be calculated according to [17] by using the Eq. (10):

$$\eta_{MFPT,en} = \frac{(h_1 - h_2)}{(h_1 - h_{2s})} \quad (10)$$

2.3 The Principle of the MFPT Developed Power Variation

MFPT developed power can be calculated according to Fig. 2 using an Eq. (11):

$$P_{MFPT} = \dot{m}_{MFP} \cdot (h_1 - h_2) \quad (11)$$

Three different methods can be used for the MFPT power change (if the same steam inlet pressure and temperature and the same steam outlet pressure are assumed in every turbine operating point):

- 1) Change in steam mass flow through the MFPT;
- 2) Change in the value of steam specific enthalpy at the steam turbine outlet (h_2);
- 3) Combination of methods 1 and 2.

In this paper, the combined method (method 3) was selected for each operating point to present the change of MFPT energy efficiency and energy power losses.

Turbine developed power was varied from 50 kW up to a maximum of 570 kW in steps of 20 kW. Power change requires a change in steam mass flow through the turbine, so

the corresponding steam mass flow for any turbine power was calculated by using the Eq. (6). At each operating point, steam pressure and temperature at the turbine inlet and steam pressure at the turbine outlet remain identical to the measured data. Steam enthalpy at the turbine outlet (h_2) was calculated for each turbine power and mass flow by using Eq. (8). Change in steam enthalpy at the turbine outlet (h_2) along with the change of steam mass flow cause the change of MFPT energy efficiency and energy power losses according to Eq. (9) and Eq. (10).

3 MEASURING EQUIPMENT AND MEASUREMENT RESULTS OF THE ANALYZED MFPT

Measurement results were obtained from the existing measuring equipment mounted on the MFPT inlet and outlet and on the main feedwater pump inlet. The list of the measuring equipment used is presented in Tab. 2.

Table 2 Measuring equipment for the analyzed turbine and main feedwater pump

Steam temperature (MFPT inlet)	Greisinger GTF 601-Pt100 - Immersion probe [18]
Steam pressure (MFPT inlet)	Yamatake JTG980A - Pressure Transmitter [19]
Steam pressure (MFPT outlet)	Yamatake JTG940A - Pressure Transmitter [19]
Feedwater volume flow (pump inlet)	Promass 80F - Coriolis Mass Flow Measuring System [20]

Measurement results of the required operating parameters at MFPT inlet and outlet along with water volume flow at the main feed water pump inlet are presented in Table 3. Operating points in Tab. 3 present an LNG carrier steam system load (1 is the lowest observed system load, 9 is the highest observed system load). MFPT load is directly proportional to the steam system load; higher steam system load denotes a higher MFPT load and vice versa.

Table 3 Turbine and main feedwater pump measurement results in various operation regimes

O.P.*	MFP water volume flow (m ³ /h)	Steam temperature at the MFPT inlet (°C)	Steam pressure at the MFPT inlet (MPa)	Steam pressure at the MFPT outlet (MPa)
1	69.71	497	5.980	0.272
2	76.64	502	6.074	0.266
3	82.90	510	6.067	0.251
4	87.29	511	6.078	0.237
5	94.22	513	6.020	0.239
6	100.52	512	6.010	0.256
7	106.01	510	5.874	0.235
8	117.04	500	5.795	0.250
9	118.26	500	5.900	0.246

* O.P. = Operating Point

4 ENERGY EFFICIENCY AND ENERGY POWER LOSSES DURING MFPT DEVELOPED POWER VARIATION

The change in MFPT energy efficiency and energy power losses during the turbine developed power variation was performed in each operating point from Tab. 3. Complete analysis gives a conclusion that increase or decrease in turbine developed power resulted with the same

trends in each operating point. The only differences which occurred between any two operating points in Tab. 3 are the values of turbine energy efficiencies and losses.

Therefore, it is not necessary to present the change in MFPT energy efficiency and losses for each observed operating point, but it is important to show the change for at least several turbine loads. Loads from Tab. 3 selected for deeper discussion in this paper are the lowest turbine load (Operating point 1), one of the middle turbine loads (Operating point 5), and the highest observed turbine load (Operating point 9).

4.1 MFPT Developed Power Variation for Operating Point 1

Change in energy efficiency for MFPT in operating point 1 (Tab. 3), during the developed power variation is shown in Fig. 3. Increase in turbine developed power causes an increase in energy efficiency from the lowest to the highest observed turbine load. Continuous increase in MFPT energy efficiency, according to Eq. (10), is caused by a continuous decrease in steam specific enthalpy at the turbine outlet (h_2) during power variation from 50 kW to 570 kW. At the lowest observed turbine power of 50 kW at this operating point, energy efficiency amounts to only 10.63 %, while maximum turbine energy efficiency is obtained at the highest turbine developed power of 570 kW and amounts to 60.30%.

Turbine energy efficiency in each operating point, as well as in operating point 1, is calculated by using Eq. (10). For each operating point, energy efficiency change is affected only by the change in steam specific enthalpy after real polytropic expansion (h_2) which is calculated according to Eq. (8). Change of turbine developed power causes changes in steam mass flow through the turbine which is calculated by using Eq. (6), where the turbine power is a known and steam mass flow is an unknown variable. Values of steam specific enthalpy after real polytropic expansion (h_2) decrease through entire observed turbine power range because the intensity of increase in turbine power is higher in comparison with an increase in steam mass flow through the turbine.

MFPT load is directly proportional to the ship steam system load. In operating point 1, MFPT energy efficiency during LNG carrier exploitation amounts to only 47.74%, which is 12.56% lower energy efficiency than the possible maximum one for this operating point.

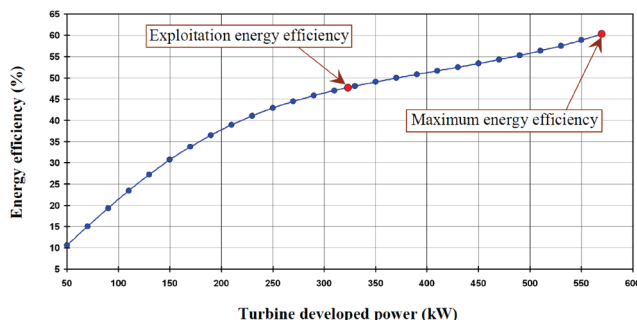


Figure 3 Energy efficiency change during MFPT developed power variation for operating point 1

Change in MFPT energy efficiency also shows that this turbine is balanced as most of the other steam system components – maximum energy efficiency will be obtained at the highest turbine (steam system) load on which the majority of LNG carrier operation can be expected.

MFPT energy power loss is calculated by using Eq. (9) for each observed operating point. Turbine energy power loss is most influenced by steam mass flow through the turbine and by steam specific enthalpy after real polytropic expansion (h_2). For any developed turbine power in each operating point, steam specific enthalpy after isentropic steam expansion (h_{2s}) remains the same because of constant steam pressure and temperature at the turbine inlet and steam pressure at the turbine outlet.

During MFPT power variation from 50 kW up to 570 kW, steam mass flow through the turbine continuously increases from 2241.33 kg/h (at 50 kW) to 4502.45 kg/h (at 570 kW), while in the same turbine load range steam specific enthalpy after real polytropic expansion (h_2) continuously decreases from 3335.89 kJ/kg (at 50 kW) to 2960.45 kJ/kg (at 570 kW). Intensity of change in these two variables defines the change of MFPT energy power loss during the power variation for each observed turbine operating point, as well as for operating point 1.

Fig. 4 presents the change in MFPT energy power loss during the turbine power variation. At the lowest turbine power of 50 kW, energy power loss is the highest and amounts to 420.55 kW. Between turbine power of 50 kW and 210 kW, energy power loss decreases, so in this turbine operating range a decrease in steam specific enthalpy after polytropic expansion (h_2) has a stronger influence on energy power loss than an increase in steam mass flow through the turbine.

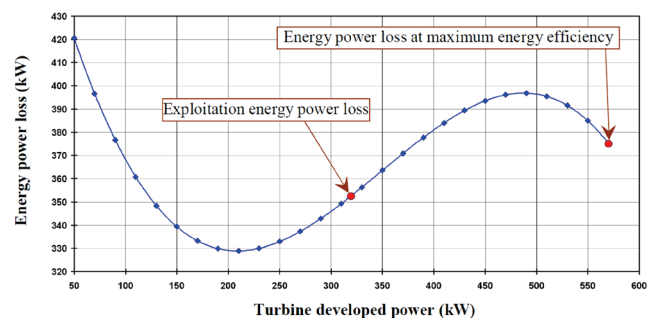


Figure 4 Energy power loss change during MFPT developed power variation for operating point 1

In the MFPT power range from 210 kW to 490 kW energy power loss increases, so in this turbine operating range an increase in steam mass flow through the turbine has a stronger influence on energy power loss than a decrease in steam specific enthalpy after polytropic expansion (h_2).

From turbine power of 490 kW up to the maximum turbine power of 570 kW, the influence of steam mass flow through the turbine and steam specific enthalpy after polytropic expansion (h_2) on energy power loss is the same as in turbine power range from 50 kW to 210 kW. As a result, in this power range turbine energy power loss decreases.

During the LNG carrier exploitation in operating point 1, the MFPT energy power loss amounts to 350.35 kW, while at turbine maximum energy efficiency in this operating point (at the highest turbine developed power of 570 kW) turbine energy power loss amounts to 375.27 kW.

The MFPT energy power loss is not proportional to turbine energy efficiency, or to the LNG carrier steam system load. From the viewpoint of MFPT energy power loss only, it will be optimal that the turbine operates at partial load, lower than in exploitation (the lowest energy power loss in this operating point is obtained at turbine developed power of 210 kW and amounts to 328.91 kW). On the other side, at turbine energy power loss minimum in this operating point turbine energy efficiency achieved will be lower than in exploitation and will amount to only 38.97 %, Fig. 3.

Conclusion valid for all MFPT operating points is that it should be decided which element should have priority during turbine operation – minimum energy power loss or maximum energy efficiency, because both goals cannot be obtained at the same time for this low power turbine. The majority of LNG carrier operation will be at the maximum steam system load, so the MFPT producer's goal surely was to achieve maximum energy efficiency.

4.2 MFPT Developed Power Variation for Operating Point 5

MFPT energy efficiency change in operating point 5 (Tab. 3), during the developed power variation is presented in Fig. 5. As in previously observed operating point 1, an increase in turbine developed power causes a continuous increase in energy efficiency until the maximum value at maximum turbine power of 570 kW.

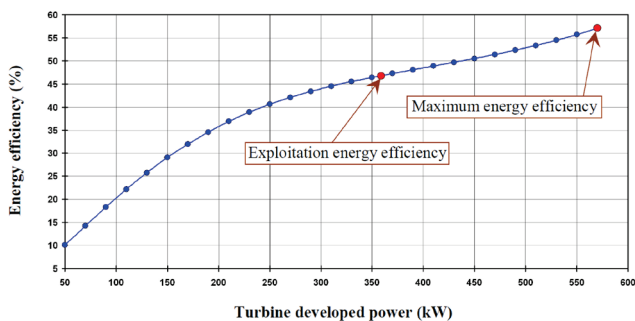


Figure 5 Energy efficiency change during MFPT developed power variation for operating point 5

In operating point 5, maximum energy efficiency is obtained as before at the highest turbine developed power and amounts to 57.12%. During the LNG carrier exploitation turbine energy efficiency amounts to only 47.41%, which is 9.71% lower energy efficiency than the maximum obtained one at this operating point. At the lowest observed turbine load of 50 kW, the lowest energy efficiency, which amounts to 10.07%, can be seen in Fig. 5.

The reasons for such MFPT energy efficiency change in operating point 5 are identical as in operating point 1 described before.

Turbine energy power loss, in operating point 5 as in operating point 1, is most influenced by steam mass flow through the turbine and by steam specific enthalpy after real polytropic expansion (h_2). Intensity of change in these two variables, described for turbine operating point 1, is identical for operating point 5 and for all the other MFPT operating points. Additionally, for a turbine operating point 5, the change in energy power loss trend of increase or decrease occurred at turbine developed power of 210 kW and 490 kW.

Fig. 6 presents the change in MFPT energy power loss during the turbine power variation for operating point 5. At the lowest turbine power of 50 kW, energy power loss is the highest and amounts to 446.76 kW. During the LNG carrier exploitation in operating point 5, the MFPT energy power loss amounts to 405.97 kW, while at turbine maximum energy efficiency in this operating point (at the highest turbine developed power of 570 kW) turbine energy power loss amounts to 427.92 kW.

The lowest energy power loss in operating point 5 is obtained at turbine developed power of 210 kW and amounts to 358.85 kW, Fig. 6, but at the lowest energy power loss turbine energy efficiency amounts to only 36.91%, which is lower energy efficiency than in exploitation, Fig. 5.

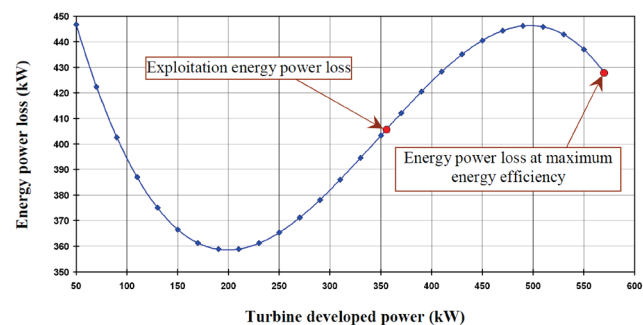


Figure 6 Energy power loss change during MFPT developed power variation for operating point 5

4.3 MFPT Developed Power Variation for Operating Point 9

The same trends and conclusions obtained from MFPT operating points 1 and 5 are also valid for operating point 9 (Tab. 3). In operating point 9, maximum turbine energy efficiency amounts to 58.78% and as before, is obtained at the highest turbine developed power of 570 kW. At the lowest turbine load (50 kW) in this operating point, energy efficiency amounts to 10.36%, while during the LNG carrier exploitation MFPT energy efficiency amounts to 50.83%. During exploitation, MFPT energy efficiency is lower for 7.95% than the maximum obtained one in operating point 9, Fig. 7.

MFPT operating point 9 also confirmed the conclusion that energy power losses are most influenced by steam mass flow through the turbine and by steam specific enthalpy after polytropic expansion (h_2), Fig. 8. Intensity of change in these two variables is the same as in two operating points described before. Again, also in this turbine operating point, the change in energy power loss trend of increase or decrease occurred at turbine developed power of 210 kW and 490 kW.

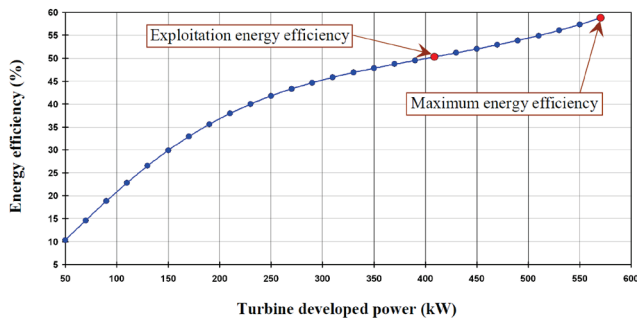


Figure 7 Energy efficiency change during MFPT developed power variation for operating point 9

At the lowest turbine power of 50 kW, energy power loss is the highest and amounts to 432.69 kW. During the LNG carrier exploitation in operating point 9, the MFPT energy power loss amounts to 402.56 kW, while at turbine maximum energy efficiency in this operating point (at the highest turbine developed power of 570 kW) turbine energy power loss amounts to 399.65 kW.

The lowest energy power loss in operating point 9 is obtained at turbine developed power of 210 kW and amounts to 342.81 kW, Fig. 8, but at the lowest energy power loss turbine energy efficiency amounts to only 37.99%, which is lower energy efficiency than in exploitation, Fig. 7.

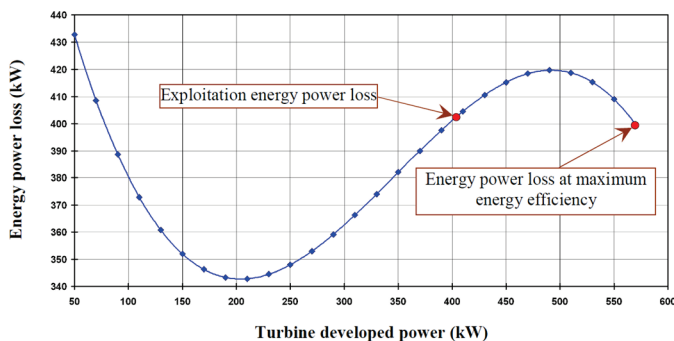


Figure 8 Energy power loss change during MFPT developed power variation for operating point 9

5 CONCLUSION

The paper presents numerical analysis of MFPT energy efficiency and energy power losses change during the variation in turbine developed power. The measurements were performed in nine different steam turbine operating points and numerical analysis has been presented in three randomly selected operating points. Nevertheless, the major conclusions are valid for the entire turbine operating range.

Increase in turbine developed power from 50 kW up to 570 kW in steps of 20 kW causes a continuous increase in turbine energy efficiency from the lowest to the highest obtained values. The continuous increase in MFPT energy efficiency is caused by a continuous decrease in steam specific enthalpy at the turbine outlet (h_2) during power variation. The fact that the highest energy efficiencies will be obtained at the highest (maximum) turbine load is valid for all the observed turbine operating points. During turbine

exploitation, energy efficiencies obtained are significantly lower than maximal ones in each operating point.

MFPT energy power losses are most influenced by steam mass flow through the turbine and by steam specific enthalpy after polytropic expansion (h_2). Intensity of change in these two variables defines areas of turbine energy power loss increase and decrease. The change in energy power loss trend occurs at turbine developed power of 210 kW and 490 kW. Minimum turbine energy power loss is detected at developed power of 210 kW, while maximum turbine energy power loss is obtained at the lowest turbine load (50 kW), which is valid for the entire steam turbine operating range.

Analysis of MFPT resulted with the conclusion that this low power steam turbine is not designed to operate at the lowest energy power loss, but is designed to operate at maximum energy efficiency (obtained at turbine maximal loads), as the most of the other steam system components. The design goal of all the LNG carrier steam system components is to obtain highest efficiencies at the highest loads since the majority of LNG carrier operation can be expected on highest loads.

Further investigation of this turbine will be based on performing exergy and exergo-economic analysis. The goal will be to find operating regimes in which the MFPT operation is the most cost-effective while retaining acceptable efficiencies.

6 ACKNOWLEDGMENT

The author would like to extend his appreciation to the main ship-owner office for conceding measuring equipment and for all help during the exploitation measurements. This work was supported by the University of Rijeka (contract no. 13.09.1.1.05).

NOMENCLATURE

fw	feedwater
h	specific enthalpy, kJ/kg
\dot{m}	mass flow, kg/s or kg/h
p	pressure, MPa
s	specific entropy, kJ/kg·K
BOG	Boil-Off Gas
\dot{E}	stream flow power, kJ/s
IN	inlet
LNG	Liquefied Natural Gas
MFP	Main Feedwater Pump
MFPT	Main Feedwater Pump Turbine
OUT	outlet
P	power, kJ/s
PL	power loss
\dot{Q}	heat transfer, kJ/s
RE	real
S	isentropic
T	temperature, °C
\dot{V}	volume flow, m ³ /h
ρ	density, kg/m ³
η	efficiency, -

7 REFERENCES

- [1] Schinas, O. & Butler, M. (2016). Feasibility and commercial considerations of LNG-fueled ships. *Ocean Engineering*, 122, 84-96. <https://doi.org/10.1016/j.oceaneng.2016.04.031>
- [2] Fernández, I. A., Gómez, M. R., Gómez, J. R., & Insua, A. A. B. (2017). Review of propulsion systems on LNG carriers. *Renewable and Sustainable Energy Reviews*, 67, 1395-1411. <https://doi.org/10.1016/j.rser.2016.09.095>
- [3] Koroglu, T. & Sogut, O. S. (2018). Conventional and Advanced Exergy Analyses of a Marine Steam Power Plant. *Energy*, 163, 392-403. <https://doi.org/10.1016/j.energy.2018.08.119>
- [4] Mrzljak, V., Poljak, I., & Medica-Viola, V. (2017). Thermodynamical analysis of high-pressure feed water heater in steam propulsion system during exploitation. *Shipbuilding*, 68(2), 45-61. <https://doi.org/10.21278/brod68204>
- [5] Bloch, H. P. & Singh, M. P. (2009). *Steam turbines-Design, Applications and Re-rating, 2nd edition*. The McGraw-Hill Companies, Inc.
- [6] Sarkar, D. K. (2015). *Thermal Power Plant - Design and Operation*. Elsevier Inc.
- [7] Baldi, F., Ahlgren, F., Melino, F., Gabrielli, C., & Andersson, K. (2016). Optimal load allocation of complex ship power plants. *Energy Conversion and Management*, 124, 344-356. <https://doi.org/10.1016/j.enconman.2016.07.009>
- [8] Haglind, F. (2011). Variable geometry gas turbines for improving the part-load performance of marine combined cycles - Combined cycle performance. *Applied Thermal Engineering*, 31, 467-476. <https://doi.org/10.1016/j.applthermaleng.2010.09.029>
- [9] Kaushik, S. C., Siva Reddy, V., & Tyagi, S. K. (2011). Energy and exergy analyses of thermal power plants: A review. *Renewable and Sustainable Energy Reviews*, 15, 1857-1872. <https://doi.org/10.1016/j.rser.2010.12.007>
- [10] Hafidhi, F., Khir, T., Ben Yahya, A., & Ben Brahim, A. (2015). Energetic and exergetic analysis of a steam turbine power plant in an existing phosphoric acid factory. *Energy Conversion and Management*, 106, 1230-1241. <https://doi.org/10.1016/j.enconman.2015.10.044>
- [11] Tan, H., Zhao, Q., Sun, N., & Li, Y. (2016). Enhancement of energy performance in a boil-off gas re-liquefaction system of LNG carriers using ejectors. *Energy Conversion and Management*, 126, 875-888. <https://doi.org/10.1016/j.enconman.2016.08.031>
- [12] Mrzljak, V., Poljak, I., & Mrakovčić, T. (2017). Energy and exergy analysis of the turbo-generators and steam turbine for the main feed water pump drive on LNG carrier. *Energy Conversion and Management*, 140, 307-323. <https://doi.org/10.1016/j.enconman.2017.03.007>
- [13] Mrzljak, V., Poljak, I., & Medica-Viola, V. (2017). Dual fuel consumption and efficiency of marine steam generators for the propulsion of LNG carrier. *Applied Thermal Engineering*, 119, 331-346. <https://doi.org/10.1016/j.applthermaleng.2017.03.078>
- [14] *Final drawing for Main Feed Pump & Turbine* (2006). Shinko Ind. Ltd., Hiroshima, Japan, ship documentation.
- [15] Ahmadi, G., Toghraie, D., Azimian, A., & Akbari, O. A. (2017). Evaluation of synchronous execution of full repowering and solar assisting in a 200 MW steam power plant, a case study. *Applied Thermal Engineering*, 112, 111-123. <https://doi.org/10.1016/j.applthermaleng.2016.10.083>
- [16] Lemmon, E. W., Huber, M. L., & McLinden, M. O. (2007). *NIST reference fluid thermodynamic and transport properties-REFPROP version 8.0*. User's guide, Colorado.
- [17] Kanoglu, M., Çengel, Y. A., & Dincer, I. (2012). *Efficiency Evaluation of Energy Systems*. Springer Briefs in Energy, Springer. <https://10.1007/978-1-4614-2242-6>
- [18] <https://www.greisinger.de> (Accessed: 10.12.2017)
- [19] <http://www.industriascontrolpro.com> (Accessed: 12.12.2017)
- [20] <https://portal.endress.com> (Accessed: 15.12.2017)

Author's contacts:

Vedran MRZLJAK, PhD, Assistant Professor
Faculty of Engineering, University of Rijeka
Vukovarska 58, 51000 Rijeka, Croatia
Tel. +385 51 651 551
E-mail: vedran.mrzljak@riteh.hr

HYBRID SEVEN-BAR PRESS MECHANISM: LINK OPTIMIZATION AND KINETOSTATIC ANALYSIS

M. Erkan KÜTÜK, Murat ARTAN, L. Canan DÜLGER

Abstract: An optimization study with kinetostatic analysis is performed on hybrid seven-bar press mechanism. This study is based on previous studies performed on planar hybrid seven-bar linkage. Dimensional synthesis is performed, and optimum link lengths for the mechanism are found. Optimization study is performed by using genetic algorithm (GA). Genetic Algorithm Toolbox is used with Optimization Toolbox in MATLAB®. The design variables and the constraints are used during design optimization. The objective function is determined and eight precision points are used. A seven-bar linkage system with two degrees of freedom is chosen as an example. Metal stamping operation with a dwell is taken as the case study. Having completed optimization, the kinetostatic analysis is performed. All forces on the links and the crank torques are calculated on the hybrid system with the optimized link lengths.

Keywords: hybrid mechanism; genetic algorithm; kinetostatic analysis; linkage optimization; mechanism synthesis; seven link press mechanism

1 INTRODUCTION

Many industrial applications are potentially used as hybrid mechanisms. Some of them can be used for cutting, printing, and stamping. Hybrid mechanism configurations are seen in literature: five-bar slider crank, and seven-bar, also nine-bar. Two different actuators are combined with a mechanism to give it a programmable motion. A constant velocity (CV) motor and servo motor (SM) are the actuators. However, while introducing different configurations, there is a need for synthesis to get the links lengths as its optimum [1].

Some studies have given kinematics and dynamics of hybrid configurations. Here some of them are taken as the optimization methods for synthesis of a seven-bar press mechanism. Simulated annealing (SA), genetic algorithms (GA), neural networks (NN), particle swarm optimization (PSO), and the others are applied in studies [2]. M. A. Laribi et al. [3] have used a hybrid method GA-FL for solving the problem of path generation in synthesis of a four-bar mechanism. Blackett [4] has performed synthesis of a five-bar mechanism. The Hooke and Rees pattern search technique has been applied. R. McDougall [5] has used Optimization based mechanism synthesis (OBMS) using four-bar and five-bar mechanisms using PSO algorithm. C. Meng et al. [6] have presented a research on a press introducing hybrid input. Inverse kinematics is studied for hybrid driven mechanism. Z. Yuan et al. [7] have studied two different hybrid mechanisms to get an output motion by minimizing torque and power from the servo motor. Their arrangement is called the slider hybrid mechanism. K. Zang [8] has studied hybrid mechanism with a five-bar. A hybrid five-bar configuration is presented with related kinematics and its mathematical model. Li and Zhang [9] have used a seven-bar mechanism press with hybrid driven case for deep drawing. M. E. Kütük [10] has performed a study on inverse kinematics issues on hybrid driven seven-bar mechanism with motion design for press application. The dimensions of

a seven-bar hybrid press mechanism are found by using experimental optimization. S. Ebrahimi and P. Payvandy [11] have presented a study on the dimensional synthesis using different heuristic optimization techniques: GA, PSO and DE.

This study is based on an industrial project for a press mechanism designed with a seven-bar mechanism. Motion with a dwell segment is given for a deep drawing study. MATLAB® GA solver is used in Global Optimization Toolbox. Synthesis of a seven-bar mechanism is presented by using eight precision points. Having performed optimization, the mechanism is drawn. Then kinetostatic analysis is achieved by applying a representative force on the ram. The results are presented and discussed.

2 SEVEN-BAR PRESS MECHANISM

A seven-bar mechanism is used for producing different ram motion scenarios. A hybrid press mechanism is given a detailed motion design procedure in Kütük's study [1]. Forward and inverse kinematics issues are explicitly given. One axis is driven by a CV motor and the other axis is driven by an SM. The seven-bar press mechanism referred is shown below in Fig. 1.

Loops 1 and 2:

$$\vec{r}_5 + \vec{r}_6 = \vec{FG} + \vec{GC} + \vec{r}_4 \quad (1)$$

$$\vec{r}_5 + \vec{r}_6 = \vec{r}_1 + \vec{r}_2 + \vec{r}_3 \quad (2)$$

Here $r_1, r_2, r_3, r_4, r_5, r_6, \theta$ and e are described as the dimensional parameters of the seven-bar press mechanism. The slider motion (s) is expressed as $s = f(\theta_2, \theta_5)$. The angular displacement, angular velocity and angular acceleration of link r_5 are driven by a CV motor. The angular displacement, angular velocity and angular acceleration of link r_2 are driven by an SM.

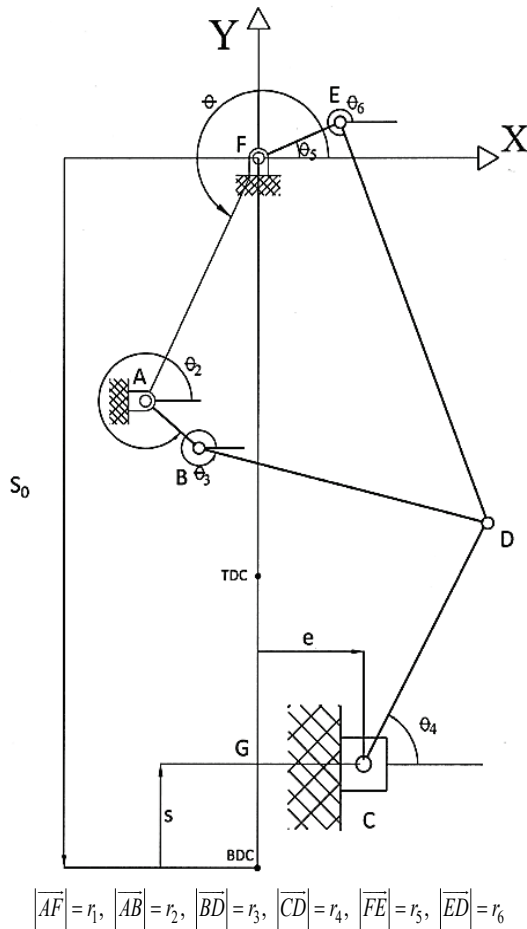


Figure 1 Seven-bar mechanism [1]

2.1 Synthesis of a Seven-Bar Mechanism

Li et al. [12] have given the classifications of hybrid five-bar linkages by using the unrestraint double-crank type. Kütük et al. have then performed an experimental optimization [10, 13]. A traditional trial and error approach is used to design a seven-bar press mechanism. The input link r_2 and r_5 are given as unrestraint cranks.

$$r_1 + r_2 + r_5 < r_3 + r_6 \quad (3)$$

$$r_2 + r_5 + r_6 < r_1 + r_3 \quad (4)$$

$$r_2 + r_3 + r_5 < r_1 + r_6 \quad (5)$$

The inequality constraints should be satisfied to provide slider mobility condition. X_D gives the coordinate of point D in x direction in Eq. (6). The link lengths inequality constraints are given in Eq. (7). S_0 is the point where r_5 , r_6 and r_4 are lined up in a straight line. By using Eq. (8);

$$r_4 > X_D - e \quad (6)$$

$$r_i \min \leq r_i \leq r_i \max \quad (7)$$

$$r_i \min \leq r_i \leq r_i \max \quad (8)$$

This study was started by using the values found previously when deciding intervals during optimization. M.E. Kütük found them while performing conceptual design during his M.Sc. thesis [1] as: $r_1 = 530$ mm, $r_2 = 200$ mm, $r_3 = 650$ mm, $r_4 = 900$ mm, $r_5 = 170$ mm, $r_6 = 800$ mm, $e = 6.73$ mm.

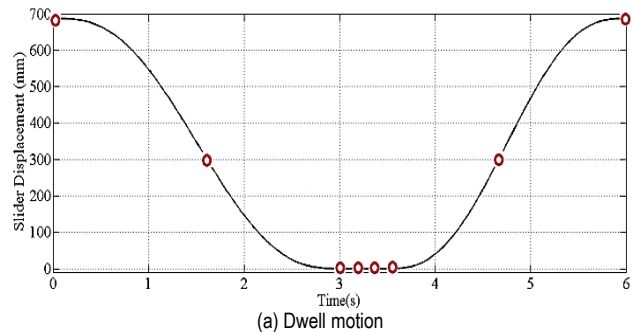
3 MOTION EXAMPLE

The displacement of the slider link is given in Fig. 2(a). Stroke of the slider is 687 mm with 10 stroke/minute and the motion has got 3 segments. The motion kinematics is illustrated in Tab. 1. The segment number, time interval and initial and final values of position, velocity and acceleration of each segment are given.

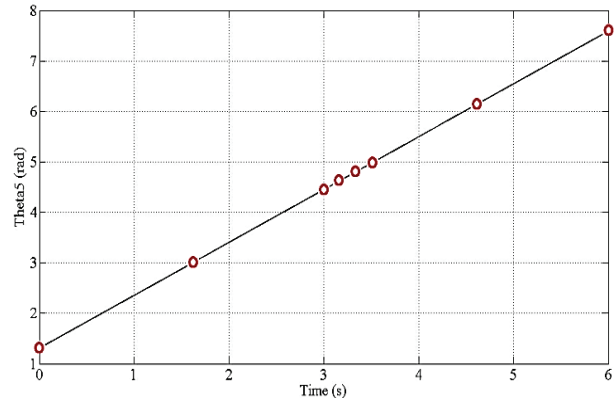
Table 1 Kinematics of the dwell type motion

Segment number	Motion time (s)	Position (mm)	Velocity (mm/s)	Acceleration (mm/s ²)
1	$0 \leq t \leq 3$	687.0	0.0	0.0
2	$3 \leq t \leq 3.5$	0.0	0.0	0.0
3	$3.5 \leq t \leq 6$	0.687	0.0	0.0

The 5th link is driven by CV motor. It rotates 2π radians in counterclockwise (CCW) direction. Its angular velocity is a constant value, 1.0472 rad/s in Fig. 2(b). The red circles in Fig. 2(a) and (b) show eight precision points taken during dimensional synthesis.



(a) Dwell motion



(b) Crank motion (the 5th link)

Figure 2 Slider and crank motion

4 OPTIMIZATION PROBLEM WITH GENETIC ALGORITHM

The mechanism optimization problem is separated into four parts: the conceptual design; the model development with

design variables; building of an objective function; and finding the best values satisfying the design constraints for the mechanism [14]. Optimization is very important in engineering design and can solve many synthesis problems. The link lengths and initial angles describe the design variables of the mechanism. The constrained nonlinear optimization is performed for a seven-bar hybrid mechanism. The optimization objective function and the constraints are determined by considering the press motion characteristics. The following optimization problem represents the constrained nonlinear optimization. Objective function is described first. Forward kinematics equations are used to get the objective function. The objective function is given in Eq. (9) by minimizing f_{obj} as:

$$f_{obj} = \sum_{i=1}^k (s_d^i - s_g^i)^2 \quad (9)$$

where s_d^i represents the design precision points required, and s_g^i is the given point for the ram. Here eight precision points are taken. The results are obtained having run the optimization program many times. The design variables are:

$$X = [r_1, r_2, r_3, r_4, r_5, r_6, e, \theta, \theta_{2i}] \quad (10)$$

where θ_{2i} is given as eight points from $i = 1, \dots, 8$. Lower and upper limits of a seven-bar mechanism are defined as: [500, 150, 600, 850, 150, 750, 0, π , 0, 0, 0, 0, 0, 0, 0] and [600, 250, 700, 950, 250, 850, 10, $3\pi/2$, 2π , 2π , 2π , 2π , 2π , 2π , 2π , 2π].

They are set while performing the optimization algorithm in Matlab [15]. GA Toolbox is applied for getting optimum values for the links. GA is set as follows: number of generation $NP = 100$, Crossover probability $CP = 0.6$, Adaptive feasible, Mutation probability $MP = 0.1$, roulette wheel is chosen referring to previous studies performed. The synthesis study is being started by using Return-TDC as the first precision point, Return-intermediate as the second precision point, four points during dwell at BDC, one point for Rise-intermediate, and one point for Rise-TDC. Optimum solution performing eight precision points are determined. The objective function values are found between 1.23×10^{-5} and -6.99×10^{-8} . The seven link lengths and the offset are taken as: $r_1 = 571.77$ mm, $r_2 = 177.99$ mm, $r_3 = 656.53$ mm, $r_4 = 853.96$ mm, $r_5 = 198.94$ mm, $r_6 = 756.89$ mm, $e = 7.38$ mm.

5 HYBRID SEVEN-BAR MECHANISM IN MATLAB®

A program based on forward kinematics equations is written in Matlab® in order to see the simultaneous positions of the hybrid seven-bar mechanism. The angular positions of the second and the fifth links must be given as the input values. The hybrid system with eight different values of θ_2 and θ_5 are illustrated in Figs. 3-5. The hybrid mechanism tracing precision points are given in Fig. 2(a). Here $s = 0$ and $s = 687$ mm are taken by referring to study [1]. Industrial applications will refer

to dwell period for the second segment of the motion, which is very important for metal forming operations.

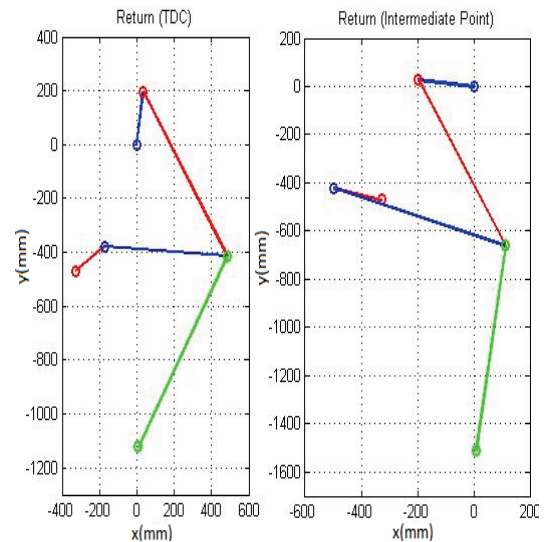


Figure 3 TDC and intermediate point in return period

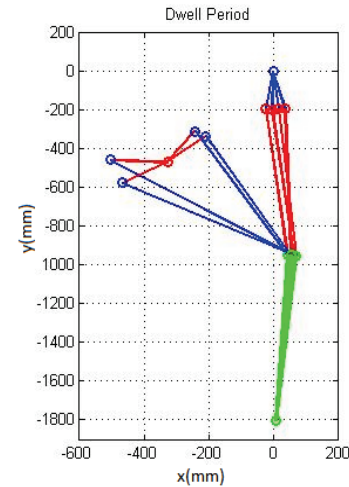


Figure 4 Dwell period (BDC-4 precision points)

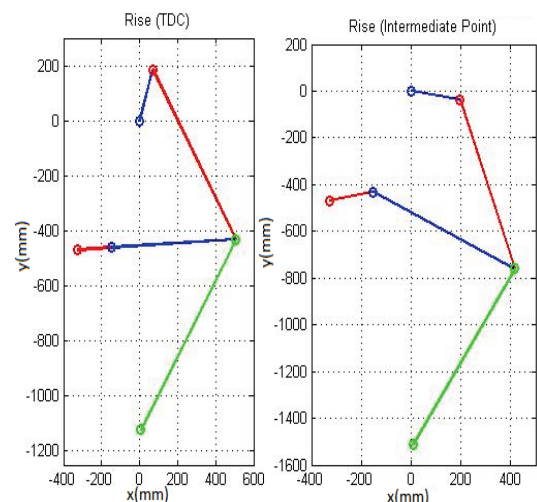


Figure 5 TDC and intermediate point in rise period

6 THE DYNAMIC MODEL FROM KINETO-STATIC METHOD

The kinetostatic method is also known as D'Alembert technique. This method rearranges the Newton's second law. A dynamic problem is transformed into a static one by adding fictitious inertial forces and inertial torques onto the system. One fictitious force on each moving body which is equal to the mass of that body times the acceleration of its mass center. The direction is opposite to its acceleration. It is directly applied onto the center of gravity, apart from the already existing real forces. One fictitious torque on each moving body which is equal to the centroidal inertia of that body times its angular acceleration. The direction is opposite to that of acceleration. The already existing torque is also applied. The model is then analyzed with the rules of statics [16]. The free body diagrams of the links are given in Fig. 6.

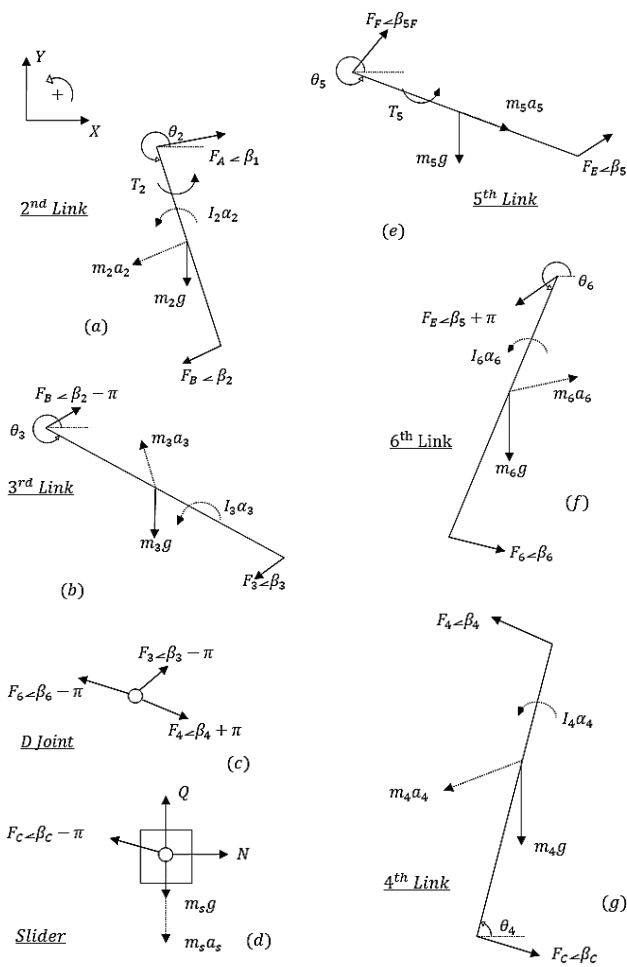


Figure 6 Free body diagram of the links

In the dynamic model, the velocity fluctuation of the constant velocity motor, the elastic deformation and friction force of the links are assumed as zero to make the system simple. Kinetostatic diagram of each link in hybrid mechanism is shown in Fig. 6 (a, b, c, d, e, f, g). Inertia forces and inertia torques are acted on every link of the hybrid driven mechanism. They are shown by dashed vectors. Thus, the static equilibrium equations of each link can be constructed [17]. The links used

in the mechanism are taken as solid cylinders. The parameters of the links are given in Tab. 2.

Table 2 The parameters of the links

Parameters	Link 2	Link 3	Link 4	Link 5	Link 6	Slider
Radius (m)	0.025	0.025	0.025	0.025	0.025	-
Mass (kg)	3	9.95	13.78	2.6	12.25	20
Moment of inertia (kg·m ²)	0.0105	0.3519	0.9323	0.0067	0.6552	-

Link AB

$$F_{Ax} - F_{Bx} = m_2 \ddot{X}_{cg2} \quad (11)$$

$$F_{Ay} - F_{By} - m_2 g = m_2 \ddot{Y}_{cg2} \quad (12)$$

$$r_2' = [r_{Acg2} \cos(\theta_2 - \pi), r_{Acg2} \sin(\theta_2 - \pi), 0] \quad (13)$$

$$F_A = [F_{Ax}, F_{Ay}, 0] \quad (14)$$

where r_{Acg2} is the distance between the mass center of the second link and A point.

$$r_2'' = [r_{Bcg2} \cos \theta_2, r_{Bcg2} \sin \theta_2, 0] \quad (15)$$

$$F_B = [-F_{Bx}, -F_{By}, 0] \quad (16)$$

where r_{Bcg2} is the distance between the mass center of the second link and B point.

$$\sum M_{cg2} = (r_2' \times F_A) + (r_2'' \times F_B) + T_2 = I_2 \ddot{\theta}_{cg2} \quad (17)$$

Link BD

$$F_{Bx} - F_{3x} = m_3 \ddot{X}_{cg3} \quad (18)$$

$$F_{By} - F_{3y} - m_3 g = m_3 \ddot{Y}_{cg3} \quad (19)$$

$$r_3' = [r_{Bcg3} \cos(\theta_3 - \pi), r_{Bcg3} \sin(\theta_3 - \pi), 0] \quad (20)$$

$$F_B = [F_{Bx}, F_{By}, 0] \quad (21)$$

where r_{Bcg3} is the distance between the mass center of the third link and B point.

$$r_3'' = [r_{Dcg3} \cos \theta_3, r_{Dcg3} \sin \theta_3, 0] \quad (22)$$

$$F_D = [-F_{3x}, -F_{3y}, 0] \quad (23)$$

where r_{Dcg3} is the distance between the mass center of the third link and D point.

Results of the Kinetostatic Analysis
of
Hybrid Driven Mechanism

```

*** System inputs ***

s      = 0.0024 (m)
sdot= 0 (m/s)
sddot= 0 (m/s^2)
theta5 = 4.86 (rad)
w5= 1.0472 (rad/s)
alpha5 =0 (rad/s^2)
Q      = 100000 (Newton) (Forming force of the slider)

***Results ***

Fax = -6240.21 (N)
Fay = 3308.17 (N)
Fa = 7062.88 (N)
Angle of Fa = 152.07 (degrees)

Fbx = -6107.53 (N)
Fby = 2972.84 (N)
Fb = 6792.62 (N)
Angle of Fb = 154.046 (degrees)
F3x = -4422.43 (N)
F3y = 5899.67 (N)
F3 = 7373.2 (N)
Angle of F3 = 126.855 (degrees)

F4x = 3566.28 (N)
F4y = -99645.3 (N)
F4 = 99709.1 (N)
Angle of F4 = -87.9503 (degrees)

Fcx = 1841.99 (N)
Fcy = -99803.8 (N)
Fc = 99820.8 (N)
Angle of Fc = -88.9427 (degrees)

Ffx = -676.921 (N)
Ffy = -105374 (N)
Ff = 105376 (N)
Angle of Ff = 269.632 (degrees)

Fex = 676.88 (N)
Fey = 105400 (N)
Fe = 105402 (N)
Angle of Fe = 89.6321 (degrees)

F6x = -856.154 (N)
F6y = -105545 (N)
F6 = 105548 (N)
Angle of F6 = 269.535 (degrees)

T2 = -988.72 (Nm)
T5 = -3216.83 (Nm)
N = 1841.99 (N)

```

Figure 7 Results of analysis

D is a known matrix. Some components of the D matrix are given in a symbolic form. E is an unknown matrix including the reaction forces in all joints and torques in the cranks of the mechanism. F is a known matrix formed by inertia torques, inertia forces and an external force. Equations in [1] are used to obtain F matrix. E matrix can easily be found by an inverse operation. It is illustrated in Eq. (51).

$$E = D^{-1} \times F \quad (51)$$

The elements given in D matrix are;

$$D_{3,1} = r_{Acg2} \sin \theta_2, D_{3,2} = -r_{Acg2} \cos \theta_2, D_{3,3} = r_{Bcg2} \sin \theta_2 \quad (52)$$

$$D_{3,4} = -r_{Bcg2} \cos \theta_2$$

$$D_{6,3} = r_{Bcg3} \sin \theta_3, D_{6,4} = -r_{Bcg3} \cos \theta_3, D_{6,5} = r_{Dcg3} \sin \theta_3 \quad (53)$$

$$D_{6,6} = -r_{Dcg3} \cos \theta_3$$

$$D_{9,7} = r_{Dcg4} \sin \theta_4, D_{9,8} = r_{Dcg4} \cos \theta_4, D_{9,9} = r_{Ccg4} \sin \theta_4 \quad (54)$$

$$D_{9,10} = r_{Ccg4} \cos \theta_4$$

$$D_{12,11} = r_{Fcg5} \sin \theta_5, D_{12,12} = -r_{Fcg5} \cos \theta_5, D_{12,13} = -r_{Ecg5} \sin \theta_5 \quad (55)$$

$$D_{12,14} = r_{Ecg5} \cos \theta_5$$

$$D_{15,13} = -r_{Ecg6} \sin \theta_6, D_{15,14} = r_{Ecg6} \cos \theta_6, D_{15,15} = -r_{Dcg6} \sin \theta_6 \quad (56)$$

$$D_{15,16} = -r_{Dcg6} \cos \theta_6$$

6.1 An Example Analysis

The reaction forces in each joint and the cranks torques can be obtained as illustrated below by using a Matlab® code written for kinetostatic equations. The data including the slider displacement, velocity and acceleration and the angular displacement, velocity and acceleration of the crank driven by the constant velocity motor and forming force of the slider are given as input parameters. Fig. 7 shows the output of the code written in Matlab®.

7 CONCLUSION

A hybrid seven-bar press mechanism is explained with link optimization. Genetic algorithm is applied for finding optimum link lengths for the mechanism. The variations of the design variables are checked. They all operate in the operating limits of the press mechanism. One mechanism satisfying eight precision point is taken as an example and presented here. Future work will include more precision points for performing the required motion. An example for kinetostatic analysis showing all forces in each link and torques in the cranks of the hybrid system is presented. Studies on this subject are continuing in Mechatronics laboratory.

8 REFERENCES

- [1] Kütük, M. E. (2013). Hybrid machine systems: Analysis and control, *MSc Thesis*.
- [2] Miles, C. A. (1996). The synthesis of hybrid mechanisms using genetic algorithms, *PhD Thesis*.
- [3] Laribi, M. A., Mlika, A., & Romdhane, Z. L. (2004). A combined genetic algorithm-fuzzy logic method (GA-FL) in mechanism synthesis. *Mechanism and Machine Theory*, 39, 717-735. <https://doi.org/10.1016/j.mechmachtheory.2004.02.004>

- [4] Blackett, R. C. (2001). Optimal synthesis of planar five link mechanisms for the production of nonlinear mechanical advantage, *MSc Thesis*.
- [5] McDougall, R. (2001). Optimization-based mechanism synthesis using multi-objective parallel asynchronous particle swarm optimization, *MSc Thesis*.
- [6] Meng, C., Zhang, C., Lu, Y., & Shen, Z. (2004). Research on a new press with hybrid input. *Proceedings of the 11th Congress in Mechanism and Machine Science*, Tianjin/Chin.
- [7] Yuan, Z., Gilmartin, M. J., & Douglas, S. S. (2005). Design of hybrid machines for nonuniform motion production. *IMechE, Part C: J. of Mech. Eng. Science*, 219, 491-499.
<https://doi.org/10.1243/095440605X16992>
- [8] Zhang, K. (2006). Optimization dynamics design of hybrid driving mechanism. *Pr. of the 2006 IEEE, Int. C. on Mechatronics and Automation*, 1914-1919.
<https://doi.org/10.1109/ICMA.2006.257546>
- [9] Li, H. & Zhang, Y. (2010). Seven bar mechanism press with hybrid driven mechanism for deep drawing: Part I -Kinematics analysis and optimum design. *J. of Mech. Science and Tech.*, 24(11), 2153-2160.
<https://doi.org/10.1007/s12206-010-0819-0>
- [10] Kütük, M. E. & Dülger, L. C. (2016). A hybrid press system: motion design and inverse kinematics issues. *Eng. Science and Tech., Int. Journal*, 19, 846-856.
<https://doi.org/10.1016/j.jestch.2015.11.012>
- [11] Ebrahimi, S. & Payvandy, P. (2015). Efficient constrained synthesis of path generating fourbar mechanisms based on the heuristic optimization algorithms. *Mechanism and Machine Theory*, 85, 189-204.
<https://doi.org/10.1016/j.mechmachtheory.2014.11.021>
- [12] Li, H., Lihui, F., & Zhang, Y. (2010). Optimum design of a hybrid driven mechanical press based on inverse kinematics. *Strojniski Vestnik*, 56, 301-306.
Kütük, M. E., Halicioglu, R., & Dulger, L. C. (2015). Kinematics and simulation of a hybrid mechanism: MATLAB/SimMechanics. *Journal of Physics Conference Series*. <https://doi.org/10.1088/1742-6596/574/1/012016>.
- [13] Messac, A., Optimization in practice with Matlab for engineering students and professionals, 2015, Cambridge University Press.
- [14] Matlab Optimization Toolbox, Users Guide (V2), 2001.
- [15] Shigley J. E. & Uicker J. J. (1994). *Theory of Machines and Mechanisms*. Second Edition, McGraw-Hill Company.
- [16] Kai, H. (2008). Design and control of a controllable hybrid mechanical metal forming press, *PhD Thesis*.

Authors' contacts:

M. Erkan KÜTÜK, PhD Candidate, Research Assistant
Gaziantep University, Mechanical Engineering Department
+903423172534, mekutuk@gantep.edu.tr

Murat ARTAN, MSc Student
Gaziantep University, Mechanical Engineering Department
+903423172534, muratartan@hotmail.com

L. Canan DÜLGER, PhD, Professor
Corresponding Author
İzmir University of Economics, Mechanical Engineering Department
+902324888557, lalecanandulger@gmail.com (After September 2018)
canan.dulger@ieu.edu.tr

DIFFERENT SENSOR SYSTEMS FOR THE APPLICATION OF VARIABLE RATE TECHNOLOGY IN PERMANENT CROPS

Davor PETROVIĆ, Mladen JURISIĆ, Vjekoslav TADIĆ, Ivan PLAŠČAK, Željko BARAČ

Abstract: The paper presents a review of different sensory systems for trees' characterization and detection in permanent crops and the detection of plant health status in crop conditions for the purpose of applying the variable application rate. The use of new technologies enables the use of variable inputs in production with the aim of increasing the economic profit and reducing the negative impact on the environment. World trends increasingly emphasize the use of various sensor systems to achieve precision agriculture and apply the following: ultrasonic sensors for the detection of permanent crops; LIDAR (optical) sensors for treetop detection and characterization; infrared sensors with similar characteristics of optical sensors, but with very low cost prices and N - sensors for variable nitric fertilization. The daily development of sensor systems applied in agricultural production improves the performance and quality of the machines they are installed on. With a more intensive use of sensors in agricultural mechanization, their price becomes more acceptable for widespread use by achieving high quality work with respect to the ecological principles of sustainable production.

Keywords: agriculture; crop protection; sensors; sprayers; treetop; variable rate technology (VRT)

1 INTRODUCTION

In the current agricultural production, the application of pesticides implies a uniform application throughout the plant or crop area, resulting in an increased risk of environmental contamination and the use of larger norms. Therefore, more modern world trends emphasize the importance of applying sensors and precision agriculture to the rational use of pesticides. That is why it is very important to know the geometric properties of permanent crops and the possibility of applying a variable spreading standard with respect to the optimum dose required to control pests, with the least impact on the environment. Geometric characteristics of a plant or crops are fundamental information on the basis of which the variable rate technology can be applied. Although conventional sprayers are equipped with sensor systems that are more cost-effective in exploitation (reducing pesticide consumption per unit area), they are still not available for a wide range of farmers due to relatively high prices. Due to this problem, research on new technologies and the possibility of reducing spray rates are intensified with the aim of a rational use of pesticides, reduction of production costs and protection of the entire agro-ecosystem.

With regard to the given above, and with the increasement in the automatization of agricultural systems, sensors are becoming the main component for the collection and transmission of information. In this review, is primarily used for the detection and geometrical characterization of a treetop for satisfying pesticide protection of permanent crops. In the advancement of technology, sensors are getting more and more perfect and they are present in many processes in agriculture, such as measuring, controlling and regulation [1, 2, 3, 4, 5, 6...].

In the context of precision agriculture and variable rate technology, sensors are also used in plant scanning to provide information on the plant growth phase and needs for nitrogen. These types of sensors use reflected light to measure the the

normalized difference of vegetation index (NDVI). By gathering this information of plant health, it is possible to determine the norm for nitrogen fertilization. This approach has already been effectively used in crops such as corn and wheat [7, 8, 9]. Similar research is carried out with the aim of determining the N-norm by using special optical sensors [10, 11].

2 VARIABLE RATE TECHNOLOGY (VRT)

The crop property variability estimation within one growing plot can be useful in achieving the use of input data. The technological progress over the past decade has enabled the development of technology with variable application standards (VRT) that, according to current needs, enables input optimization.

The sensory approach to using variable input technology does not require mapping and data collection, but real-time sensors read and accept the current situation in the field or in the permanent plantation. Based on the currently measured data, the variable rate of the application of the pesticide, fertilizer or irrigation is determined. The sensor-specific variable rate does not require the application of a GPS system, but if the mentioned system is available during application, it can be used in future technological operations.

The application of new technologies in agriculture is growing rapidly as the need for a more precise application leads to a reduction in the use of chemical products (pesticides and mineral fertilizers), and remarkable savings are achieved by taking care of the ecological aspect, i.e the sustainability of agricultural production. Sophisticated equipment, which is built in agricultural machines for performing all technological operations (soil treatment, fertilization, plant protection, harvesting the fruits, etc.) has been used. More and more agricultural machinery today is equipped with smart sensors that can detect a large number of properties, ranging from crop health and water needs to

the level of nitrogen in the soil. By applying conventional methods of management in permanent crops, the trees' age and shape, treetop size and volume, soil property variability and other things are neglected.

The best example of the application of variable rate technology (VRT) in agriculture is the use of different sensory systems for crop protection in permanent crops. The use of different sensor types (ultrasonic, infrared and optical) through the application of variable rate technology represents the future of crop protection for permanent crops in mind of ecological, economic and exploitation improvement. With regard to the mentioned above and with the significance of crop protection in modern agriculture, the main goal of this paper is to problematize this part of agricultural technology.

Moreover, the sensory approach for the application of VRT is very often used for mineral fertilizer dosage. Thus, the rest of this chapter is concentrated on this property. Many authors are concerned with the research of variable application of fertilizers, determined by the yields and soil nutrition analysis in permanent crops [12]. Maps for the variable application of nitrogen on treetop structure are produced by using GPS and ultrasonic sensors [13]. Research shows that the nitrogen level can be adjusted according to the trees' size, but not according to the plantation's age, thus leading to 38-40% savings. By using LIDAR sensors, the treetop characteristics have an effect on the irrigation reduction possibility and variable fertilizers' applications have been determined by [14].

The VRT use in field crops is based on the sensory approach to light reflection measuring from plants and the collected data analysis. By varying the luminous flux on the sensor, which depends on individual plant properties, an electronic signal is sent to the regulator which performs the dosing device opening and the particular medium's application.

In practice, the sensory approach is applied to controlling weeds on agricultural areas and is used for nitrogen fertilization. The N - sensor system is based on the ability to recognize the nitrogen fertilizer standard by measuring light reflection from plants. Where reflection is higher, the leaf chlorophyll content is lower, i.e., there is a greater need for nitrogen and vice versa. In this way, it is possible to apply the corresponding, larger doses to the part of the fields showing signs of greater nitrification loss, and in order to achieve a uniform yield on all field parts. By exploitation of N - sensors, many factors may appear that can affect the reading accuracy, such as the following: different sensor distance to the leaf, the appearance of dew on leaf surface and cloudy weather – different intensity of light reflection from the leaf to the sensor, and getting inaccurate results. Asner, G.P. et al. [15] states that the main factor that prevents the accurate reading of leaf colour is the light reflection from the ground. This problem is more expressed at the lower LAI index and in earlier vegetative phases [16]. One of the solutions to avoid these problems is to put sensors to a higher level for a more vertical leaf evaluation where LAI is uniform and the reflection from the ground is minimal. Furthermore, in order to avoid the

mentioned problems, Pena-Yewtukhiw, E. M. et al. [17] states that the use of a larger number of sensors (8) can reduce the error.

The use of sensor systems for achieving variable application norms is more suitable for permanent crops, since by using the said system, it is possible to quantify each individual tree in the plant by measuring its height and width. By using the selective pesticide application, the greatest savings are achieved in younger permanent crops, due to large spaces within the rows that are not filled with treetops, and at vacant sites of old plantations.

3 SENSOR SYSTEMS FOR THE APPLICATION OF PESTICIDES IN PERMANENT CROPS

3.1 Sensors

As it has already been mentioned, the development of sensory systems for detecting the presence and shape of permanent plant breeding has recently been evident. Sensors convert the measured physical size (altitude, width, volume, etc.) to analogue electrical (current, voltage, resistance) or digital information. The operating principle of the sensor is based on the interaction with the surrounding objects, and the reaction is transformed into an output signal and controlled by the technological process. There are a number of physical phenomena that can be applied when making a sensor. The measurement of nonelectric signals (optical, infrared, inductive and the like) begins by conversion to electrical signals, after which processing is performed.

Table 1 An overview of the main characteristics of sensors

Characteristics/Sensors	LIDAR	Ultrasonic	Infrared
Range measurement: < 2 m	o	++	+
Range measurement: 2 - 30 m	++	-	+
Range measurement: 30 - 100 m	+	--	+
Angle measurement: < 10°	++	-	++
Angle measurement: < 30°	++	o	++
Angular Resolution	++	-	++
Direct Velocity Information	--	o	--
Operation in the Rain	o	o	o
Operation in Fog or Snow	-	+	o
Operation if there is Dirt on the Sensor	o	++	--
Night Vision	n.a.	n.a.	++

Source: http://writingaboutcars.com/wpcontent/uploads/2015/11/Different_sensors.png [19]

++ ideally suited; + good performance; o possible, but drawbacks to be expected; - only possible with large additional effort; -- impossible; n.a. not applicable

It is important to know that each sensor has its own limitation; limited measurement accuracy that may vary depending on different field conditions. With the future development of sensory systems in agriculture, it is expected that the efficiency and accuracy of the measurement will be increased [18]. An overview of the main sensor properties is shown in Tab. 1.

3.2 Ultrasonic Sensors

Ultrasonic sensors serve to determine the distance and function according to the principle of the difference in the time interval required for the ultrasonic wave to pass from the sensor to the detected object and back (Fig. 1). They consist of an ultrasonic transceiver, an output signal generator and an amplifier. The transceiver periodically emits an ultrasonic wave frequency of 10 - 400 kHz and then receives a reflected wave from the detected object.

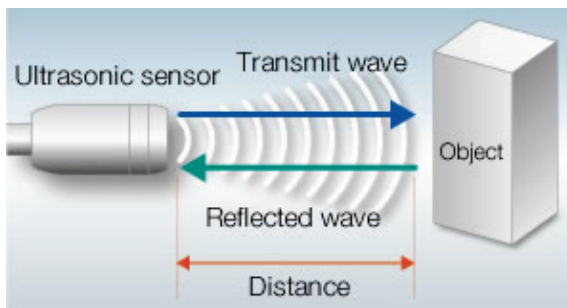


Figure 1 The operation principle of ultrasonic sensors [20]

The detection of the object's distance based on the time required for the ultrasonic wave to pass from the transmitter to receiver is basically simple, but there are several shortcomings: temperature dependence and air pressure, light intensity decrease due to radial expansion and absorption, noise effects, etc.

The most common type of ultrasonic sensor construction is in the form of a prism or a cylinder. The transceiver head may be separated from the electronic part, enabling it to be installed at inaccessible locations. The use of ultrasonic sensors in agriculture is as an idea taken from the industry, where they are used to measure different distances and determine the presence of objects [21]. Fig. 2 shows the complete system of ultrasonic sensors with electromagnetic valves and the control unit used on the sprayers.



Figure 2 Ultrasonic Sensor System

The main advantage of this type of sensor is their robust design. It reduces the negative impact of an adverse working environment (humidity, vibration, dirt, temperature, fog) and has a relatively low cost price with respect to other electronic

circuits used for the same purpose [8]. Their main disadvantage is the large angle of the divergence of ultrasonic waves, which is why the limited resolution, i.e. the accuracy of the measurement [21] is limited.

Authors [22, 23] develop a simple system based on ultrasonic sensors with an intermittent dispersion method, where sensors engage / disengage electromagnetic valves at the pressure regulator. This application method enables the savings on pesticides of 10-17% in peach plantation and in apple plantation of 20 to 27%. By developing the sensor management algorithm, savings of 28-34% and 36-52% are achieved in the same plantations [24].

Balsari, P. and Tamagnone, M. [25] state that during the research, sensors have had the ability to recognize branch diameters of 3 to 4 cm, while the minimum void they could detect was 35 cm. With advanced technology, today's ultrasonic sensors have the ability to recognize gaps between crowns of just a few inches. The precision of ultrasonic sensors is influenced by various factors: treetop distance, temperature, humidity and velocity of motion [26]. The use of a detector capable of detecting the treetop and its shape has been explored by a whole series of authors, with the aim of an accurate plant's treetop detection and a significant reduction in drift protection [2; 27-30]. Llorens, J. et al. [4] use ultrasonic sensors to determine plant geometry for a more precise determination of the spraying rate with the aim of drift reduction.

Ježić, V. et al. [31] develop an automatic spraying system, where computer-controlled spraying is achieved by the use of ultrasonic sensors and an RGB camera. The automatic system is tested at a speed of 3 kmh⁻¹ where, with respect to the control sensor-free spraying, the savings of 20.2% per each nozzle are achieved. The same authors state that the deposit, distribution and surface coverage remained unaltered by the use of sensory spraying.



Figure 3 Ultrasonic and LIDAR sensors equipped air assistance sprayer [40]

Llorens, J. et al. [32] state that by incorporating electronic parts into conventional sprayers, the spraying technique is significantly improved and the risk of spraying outside the targeted space of plant protection is reduced. Sensor system equipped dispersers, used for permanent crops' protection, base their functions on the determination of three basic parameters: tree detection, leaf mass density

and treetop structure, i.e. breeding [33]. The determination of the geometric shape and the treetop presence are relatively complex tasks because of the treetop's geometrical characteristics, which are directly related to tree growth and development.

Real-time treetop recognition by using ultrasonic sensors is investigated by many scientists around the world [1; 5; 34-42]. The treetop shape directly affects the deposition of pesticides, and thus the effectiveness of spraying. The variable application air assistance sprayer prototype, equipped with ultrasonic and LIDAR sensors for treetop shape detection, is shown in Fig. 3.

The usage of ultrasonic sensors in agricultural production has been tested on several factors. One of the key factors is the distance of the sensor from the treetop and the speed of the sprayer's movement. If the distance of the sensor is smaller, the echo ultrasound wave (echo signal) will be of greater intensity, and thus the accuracy of the measurement, while by increasing the distance, the echo signal is weakened and errors occur when reading the results [14]. If the treetop is at a small distance between the treetop and the sensor, the possibility of interference between the two sensors increases and the reading accuracy decreases [43]. According to the above mentioned authors, the average reading error in laboratory conditions is ± 0.53 cm, while in field conditions, the detection error is ± 5.11 cm, taken on the average. By analyzing the obtained results, it can be concluded that it is very important to determine the correct distance between the ultrasonic sensors with respect to the width of the angular ultrasound waves and the distance from the detected treetop. In Fig. 4, a test platform with differently positioned ultrasonic sensors for determining a reasonable distance between sensors and treetops, with the aim of preventing the interference, is shown.



Figure 4 Test platform with ultrasonic sensors [42]

Palleja, T. and Landers, A. [43-44] explore the possibility of using cheap ultrasonic sensors to determine treetop density during vegetation. The results obtained show a high degree of correlation between the leaf mass increase

and the feedback ultrasonic wave towards the sensor, but the system is not able to determine the actual leaf mass density in the crown. The same authors [45-46] develop a sensor system to identify treetop density, on the basis of which it is possible to adjust air velocity and the liquid amount during spraying.

Authors [47] compare two methods of treetop density determination in the plantation: PQA (Point Quadrat Analysis) - biomass contact probe procedure and ultrasonic sensor system. The results obtained show a very high level of the sensory method acceptability for the treetop density determination. However, it should be noted that calibration, according to the tree type, is required for each crop individually, so that the readings could be used to set the sprayer in real time. Due to the above-mentioned echo signal issues, many authors continue with studying the ultrasonic sensor systems' usage.

Li, H. et al. [48] explore the model for treetop density determination that is examined in laboratory conditions, comparing the control model of leaves put in four layers, chosen as optimal, and models with a different number of leaves' layers. The obtained results show a reading error of between 17.68 and 29.92%, in comparison with the control model. According to the above mentioned authors, the ultrasound system tested is sufficiently precise for the variable rate technology usage (VRT).



Figure 5 CIS air assistance sprayer [25]

The CIS (Crop Identification System), equipped with a GPS system, meteorological station, ultrasonic sensor system and a special set of different, electromagnetic valves equipped, nozzles, and used for permanent crops' protection, is at present the most modern system for the VRT usage (Fig. 5). The CIS sprayer works on the principle of a permanent crop current state's recognition, with respect to the position, current weather conditions (temperature, relative humidity, air velocity and wind direction), treetop presence and shape, and based on the above information, the computer determines the nozzle type (standard or anti drift) and the spraying norm.

3.3 LIDAR Sensors

LIDAR (Light Detection and Ranging) is an optical measuring instrument for laser dispersion which is repelled by very small particles in the Earth's atmosphere (aerosols,

clouds, etc.), and then registered in an optical receiver. The principle of operation is based on changing the parameters of the optical signal with a change in physical size, and these sensors do not have galvanic or magnetic connections. The laser beams obtain for each crop slice a variable number of identified points according to the distance to the sensor and the angle from the horizontal. These sensors are often called optical sensors, and they are shown in Fig. 6.

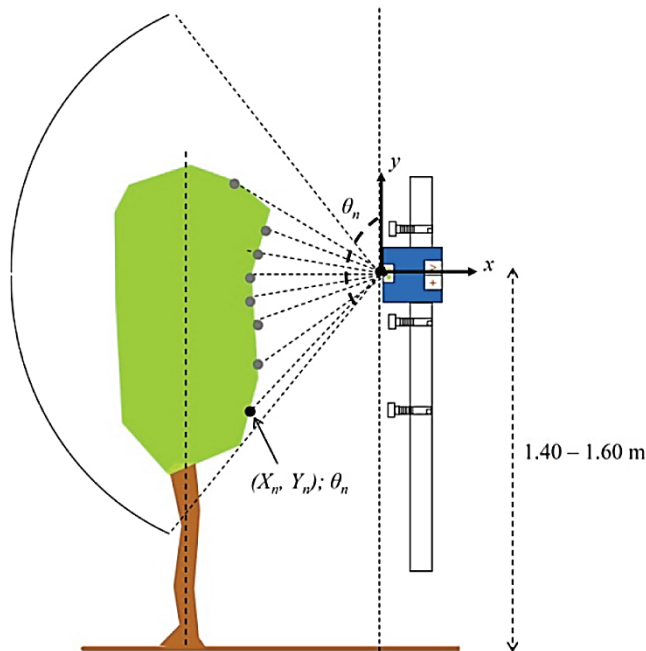


Figure 6 Functioning principle of the LIDAR sensor [4]

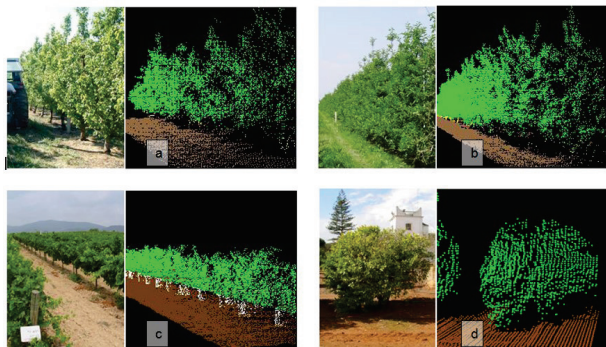


Figure 7 Pictures of different crop training systems and their corresponding 3D images obtained by the LIDAR system: pear trees (a), apple trees (b), vineyards (c) and citrus trees (d) [49]

This type of sensor can be used under all conditions of a strong magnetic field, high temperature, electric noise and chemical corrosion, and are much more flexible and reliable than ultrasonic sensors. The bad sides are: the complexity of signal production and its processing, a demand for the optical visibility between the receiver and the transmitter, and the sensitivity to mechanical vibration.

LIDAR sensors are used for almost all applications without the contact detection of objects at a great distance, and the material of the object for detection is almost inessential. Given the above mentioned characteristics, the

application possibility is multiple. Fig. 7 shows the reading mode using the LIDAR sensor.

Escola, A. et al. [40] research the accuracy of measurements between two types of sensors (ultrasonic and LIDAR sensors) to determine the treetop volume. The results show that LIDAR sensors are more accurate due to the measurement method because they detect in between 180 and 720 dots. When applied, the variable applications of both sensor types have achieved satisfactory results, but when using a LIDAR sensor, it is possible to determine the trees' geometric structure. Their ability to quickly measure the distance between the sensors and the objects allows 3D images of the treetop shape (x, y and z axis) and applying the appropriate algorithms, allowing the digital display of the treetop structure [50, 51, 52]. The mentioned sensors for surface area and leaf mass volume determination have been used as an alternative to manual methods that are expensive, time-consuming and cause treetop damage, when sampling the leaf.

Llorens, J. et al. [4] compare the measurement accuracy between the use of ultrasonic and LIDAR sensors with a manual measurement of plant volume (height, width and leaf mass volume). The obtained results show that ultrasonic sensors can successfully determine average plant characteristics, while LIDAR sensors achieve greater accuracy and more detailed information on the treetop shape. They are very suitable for the usage at longer distances because they have high spatial resolution and detection speeds, and can be used for fluid loss determination in the air drift form. When spraying, drifted liquids' detection outside the targeted object of protection has been possible with LIDAR sensors and has successfully replaced the use of passive collectors [51]. Compared to passive collectors, LIDAR sensors achieve high accuracy of spatial data, require fewer workforce, shorter data collection time, and no additional chemical analysis is required [52].

3.4 Infrared Sensors

Infrared sensors are one more type of active sensors, used to determine the treetop distance and presence and work on the transmitting and receiving light flux principle. This sensor type research has been being carried out in different directions, hence a system consisting of five, sprayer located, infrared sensors that recognize treetop presence, shape and density has been being developed by the scientists at the Cornell University. By using the sensor information obtained, the airflow decreases or increases as needed. In this way, the protective agent saving of 40% at the beginning of vegetation is achieved, while the decrease in the vineyard drift is 71 - 63% [53]. The research carried out in China includes the infrared sensors' usage, mounted on the sprayer with an electrostatic spraying system. The sensors are placed in three levels in order to detect the treetop presence and shape. Using this system, pesticide saving in between 50 and 75% [54] has been achieved.

4 CONCLUSION

Mechanical, chemical, biological and process size measurements are carried out using various measuring transformers - sensors. Their application is based on the development of materials and technologies, the integration of components and the application of micromechanics and microelectronics. As part of the advanced technology systems, sensors have become one of the inevitable parts that enable communication between the machine and the computer. Through the daily development of sensors applied in agriculture, their effect on the production process is improved. The sensors' cost price is getting smaller as well, which is why they become more accessible for use on a wide range of agricultural machines and systems. Previous research conducted over the past two decades show that ultrasound sensors are successfully used for detecting treetop presence, while the LIDAR sensor can achieve greater accuracy and give more detailed information.

Despite their low price, the use of infrared sensors is in the initial stages of research. All types of explored sensors obtain useful information for the specific spraying factors' determination. When it comes to plant protection, they ensure a satisfactory biological efficiency with a reduced liquid drift occurrence during application, unlike the conventional application systems.

5 REFERENCES

- [1] Stajanko, D., Berk, P., Lešnik, M., Jejčič, V., Lakota, M., Štrancar, A., Hočevar, M., & Rakun, J. (2012). Programmable ultrasonic sensing system for targeted spraying in orchards. *Sensors*, *12*, 15500-15519. <https://doi.org/10.3390/s121115500>
- [2] Llorens, J., Gil, E., Llop, J., & Escola, A. (2010). Variable rate dosing in precision viticulture: use of electronic devices to improve application efficiency. *Crop Prot.*, *29*, 239-248. <https://doi.org/10.1016/j.cropro.2009.12.022>
- [3] Doruchowski, G., Swiechowski, W., Godyn, A., & Holownicki, R. (2011). Automatically controlled sprayer to implement spray drift reducing application strategies in orchards. *J. fruit Ornam. Plant Res.*, *19*, 175-182.
- [4] Llorens, J., Gil, E., & Llop, J. (2011). Ultrasonic and Lidar sensors for electronic canopy characterization in vineyards: Advances to improve pesticide application methods. *Sensors*, *11*(2), 2177-2194. <https://doi.org/10.3390/s110202177>
- [5] Perry, R. & Cordero, R. (1995). Sensor controlled orchard sprayers. *Proceedings of the National Conference on Pesticide Application Technology, Guelph*, 164-171.
- [6] Koch, H., Weisser, P., Cross, J., Gilbert, A., Glass, C., Taylor, W., Walklate, P., & Western, N. (2000). Sensor equipped orchard spraying-efficacy, savings and drift reduction. *Pesticide application*, University of Surrey, Guildford, UK, 17-18, 357-362.
- [7] Raun, W., Solie, J., Stone, M., Martin, K., Freeman, K., Mullen, R., Zhang, H., Schepers, J., & Johnson, G. (2005). Optical Sensor-Based Algorithm for Crop Nitrogen Fertilization. *Communications in Soil Science and Plant Analysis*, *36*, 2759-2781. <https://doi.org/10.1080/00103620500303988>
- [8] Berntsen, J., Thomsen, A., Schelde, K., Hansen, O. H., Knudsen, L., Broge, N., Hougaard, H., & Hørfarter, R. (2006). Algorithms for sensor-based redistribution of nitrogen fertilizer in winter wheat. *Precision Agriculture*, *7*, 65-83. <https://doi.org/10.1007/s11119-006-9000-2>
- [9] Kitchen, N. R., Sudduth, K. A., Drummond, S. T., Scharf, P. C., Palm, H. L., Roberts, D. F., & Vories, E. D. (2010). Ground-Based Canopy Reflectance Sensing for Variable-Rate Nitrogen Corn Fertilization. *Agronomy Journal*, *102*, 71-84. <https://doi.org/10.2134/agronj2009.0114>
- [10] Barker, D. W. & Sawyer, J. E. (2010). Using active canopy sensors to quantify corn nitrogen stress and nitrogen application rate. *Agronomy Journal*, *102*(3), 964-971. <https://doi.org/10.2134/agronj2010.0004>
- [11] Ma, B. L., Wu, T. Y., & Shang, J. L. (2014). On-farm comparison of variable rates of nitrogen with uniform application to maize on canopy reflectance, soil nitrate and grain yield. *J Plant Nutr Soil Sci.*, *177*, 216-226. <https://doi.org/10.1002/jpln.201200338>
- [12] López, F., Jurado, M., Álamo, S., & García, L. (2004). Leaf nutrient spatial variability and site-specific fertilization maps within olive (*Olea europaea* L.) orchards. *European Journal of Agronomy*, *21*(2), 209-222. <https://doi.org/10.1016/j.eja.2003.08.005>
- [13] Zaman, Q. U., Schumann, A. W., & Miller, W. M. (2005). Variable Rate Nitrogen Application in Florida Citrus Based on Ultrasonically-Sense Tree Size. *Applied Engineering in Agriculture*, *21*(3), 331-335. <https://doi.org/10.13031/2013.18448>
- [14] Pascual, M., Villar, J. M., Rufat, J., Rosel, J. R., Sanz, R., & Arnó, J. (2011). Evaluation of peach tree growth characteristics under different irrigation strategies by LIDAR system: preliminary results. *Acta Horticulturae*, *889*, 227-232. <https://doi.org/10.17660/ActaHortic.2011.889.26>
- [15] Asner, G. P. (2004). Biophysical remote sensing signatures of arid and semiarid ecosystems: Remote sensing for natural resource management and environmental monitoring. *Manual of remote sensing*, *4*, 53-109.
- [16] Abendroth, L. J., Elmore, R. W., Boyer, M. J., & Marlay, K. S. (2011). Corn growth and development. *Iowa State University Extension, Ames, Iowa, USA*, PMR 1009.
- [17] Pena-Yewtukhiw, E. M., Schwab, G. J., Grove, J. H., Murdock, L. W., & Johnson, J. T. (2008). Spatial analysis of early wheat canopy normalized difference vegetative index: determining appropriate observation scale. *Agronomy Journal*, *100*, 454-462. <https://doi.org/10.2134/agronj2007.0063>
- [18] Pierce, F. J. & Nowak, P. (1999). Aspects of precision agriculture. *Adv. Agronomy*, *67*, 1-85. [https://doi.org/10.1016/S0065-2113\(08\)60513-1](https://doi.org/10.1016/S0065-2113(08)60513-1)
- [19] http://writingaboutcars.com/wpcontent/uploads/2015/11/Different_sensors.png
- [20] <http://www.ndk.com/en/sensor/ultrasonic/index.html>
- [21] Rovira-Más, F., Reid, J. F., Zhang, Q., & Will, J. D. (2005). Hough transform based vision algorithm for crop row detection of an automated agricultural vehicle. *Proceedings of the Institution of Mechanical Engineers, Part D. Journal of Automobile Engineering*, *219*(8), 999-1010. <https://doi.org/10.1243/095440705X34667>
- [22] Giles, D. K., Delwiche, M. J., & Dodd, R. B. (1987). Control of Orchard Spraying Based on Electronic Sensing of Target Characteristics. *Trans. ASAE*, *30*, 1624-1630. <https://doi.org/10.13031/2013.30614>
- [23] Giles, D. K., Delwiche, M. J., & Dodd, R. B. (1988). Electronic Measurement of Tree Canopy Volume. *Trans. ASAE*, *31*, 264-272. <https://doi.org/10.13031/2013.30698>

- [24] Giles, D. K., Delwiche, M. J., & Dodd, R. B. (1989). Sprayer control by sensing orchard crop characteristics: orchard architecture and spray liquid savings. *Journal of Agricultural Engineering Research*, 43, 271-289. [https://doi.org/10.1016/S0021-8634\(89\)80024-1](https://doi.org/10.1016/S0021-8634(89)80024-1)
- [25] Balsari, P. & Tamagnone, M. (1998). An ultrasonic airblast sprayer. *Proceedings of the International Conference on Agricultural Engineering*, 585-586.
- [26] Jeon, H. Y., Zhu, H., Derksen, R. C., Ozkan, H. E., Krause, C. R., & Fox, R. D. (2011). Performance evaluation of a newly developed variable-rate sprayer for nursery liner applications. *Trans. ASABE*, 54(6), 1997-2007. <https://doi.org/10.13031/2013.40648>
- [27] Doruchowski, G., Swiechowski, W., Godyn, A., & Holownicki, R. (2011). Automatically controlled sprayer to implement spray drift reducing application strategies in orchards. *J. fruit Ornament. Plant Res.*, 19,175-182.
- [28] Chen, Y., Ozkan, H. E., Zhu, H., Derksen, R. C., & Krause, C. R. (2013). Spray deposition inside tree canopies from a newly developed variable-rate air-assisted sprayer. *Trans. ASABE*, 56, 1263-1272.
- [29] Escola, A., Rosell-Polo, J. R., Planas, S., Gil, E., Pomar, J., Camp, F., Llorens, J., & Solanelles, F. (2013). Variable rate sprayer. Part I orchard prototype: design, implementation and validation. *Comput. Electron. Agric.*, 95, 122-135. <https://doi.org/10.1016/j.compag.2013.02.004>
- [30] Sedlar, A. D., Bugarin, R. M., Nuyttens, D., Turan, J. J., & Zoranovic, M. S. (2013). Quality and efficiency of apple orchard protection affected by sprayer type and application rate. *Span. J. Agric. Res.*, 11, 935-944. <https://doi.org/10.5424/sjar/2013114-3746>
- [31] Ježičič, V., Godeša, T., Hočevar, M., Širok, B., Malneršič, A., Štancar, A., Lešnik, M., & Stajniko, D. (2011). Design and Testing of an Ultrasound System for Targeted Spraying in Orchards. *Strojniški vestnik - Journal of Mechanical Engineering*, 57(7-8), 587-598. <https://doi.org/10.5545/sv-jme.2011.015>
- [32] Llorens Calveras, J., Landers, A. J., & Larzelere, W. (2013). Precision application of pesticides in orchards – adjusting liquid flow. *NY Fruit Quarterly*, 21(4), 7-10.
- [33] Fox, R. D., Derksen, R. C., Zhu, H., Brazee, R. D., & Svensson, S. (2008). A history of air-blast sprayer development and future prospects. *Trans. ASAB*, 51(2), 405-410. <https://doi.org/10.13031/2013.24375>
- [34] Perry, R. & Cordero, R. (1995). Sensor controlled orchard sprayers. *Proceedings of the National Conference on Pesticide Application Technology*, Guelph, 164-171.
- [35] Koch, H., Weisser, P., Cross, J., Gilbert, A., Glass, C., Taylor, W., Walklate, P., & Western, N. (2000). Sensor equipped orchard spraying-efficacy, savings and drift reduction. *Pesticide application, University of Surrey, Guildford, UK*, 17-18, 357-362.
- [36] Moltó, E., Martín, B., & Gutiérrez, A. (2000). PM–Power and Machinery: Design and testing of an automatic machine for spraying at a constant distance from the tree canopy. *Journal of Agricultural Engineering Research*, 77, 379-384. <https://doi.org/10.1006/jaer.2000.0621>
- [37] Schumann, A. & Zaman, Q. (2005). Software development for real-time ultrasonic mapping of tree canopy size. *Computers and Electronics in Agriculture*, 47, 25-40. <https://doi.org/10.1016/j.compag.2004.10.002>
- [38] Solanelles, F., Escola, A., Planas, S., Rosell, J. R., Camp, F., & Gracia, F. (2006). An electronic control system for pesticide application proportional to the canopy width of tree crops. *Biosystems Eng.*, 95(4), 473-481. <https://doi.org/10.1016/j.biosystemseng.2006.08.004>
- [39] Chueca, P., Garcera, C., Molto, E., & Gutierrez, A. (2008). Development of a sensor-controlled sprayer for applying lowvolume bait treatments. *Crop Protection*, 27, 1373-1379. <https://doi.org/10.1016/j.cropro.2008.05.004>
- [40] Escola, A., Planas, S., Rosell, J. R., Gràcia, F., Gil, E., & Val, L. (2007). Variable dose rate sprayer prototype for dose adjustment in tree crops according to canopy characteristics measured with ultrasonic and laser lidar sensors. *6th European Conference on Precision Agriculture – ECPA*, Skiathos, Greece.
- [41] Shirley, P. A. (1989). An introduction to ultrasonic sensing. *Sensors*, 6(11), 6.
- [42] Escola, A., Rosell-Polo, J. R., Planas, S., Gil, E., Pomar, J., Camp, F., Llorens, J., & Solanelles, F. (2013). Variable rate sprayer. Part I orchard prototype: design, implementation and validation. *Comput. Electron. Agric.*, 95, 122-135. <https://doi.org/10.1016/j.compag.2013.02.004>
- [43] Palleja, T. & Landers, A. (2014). Precision Spraying in the Orchard and Vineyard: Measuring Canopy Density. *New York Fruit*, 22, 4.
- [44] Palleja, T. & Landers, A. (2015). Precision fruit spraying: measuring canopy density and volume for air and liquid control. *SuproFruit – 13th Workshop on Spray Application in Fruit Growing, Lindau, Germany*, 448, 76-77.
- [45] Palleja, T. & Landers, A. J. (2016). Orchard and vineyard real time spraying adjustments using ultrasonic echoes. *Aspects of Applied Biology*, 132, 405-410.
- [46] Palleja, T., Llorens, J., & Landers, A. J. (2017). Measuring crop canopy – the development of a dynamic system for precision fruit crop spraying. *Advances in Animal Biosciences: Precision Agriculture*, 8(2), 250-254. <https://doi.org/10.1017/S2040470017000905>
- [47] Landers, A., Palleja, T., & Llorens, J. (2017). Technologies for the precise application of pesticides into vineyards. *www.infowine-internet journal of enology and viticulture*, 2/1.
- [48] Li, H., Zhai C., Weckler, P., Wang, N., Yang, S., & Zhang, B. A (2017). Canopy Density Model for Planar Orchard Target Detection Based on Ultrasonic Sensors. *Sensors*, 17, 31. <https://doi.org/10.3390/s17010031>
- [49] Rosell, J. R., Llorens, J., Sanz, R., Arnó, J., Ribes-Dasi, M., Masip, J., Escolà, A., Camp, F., Solanelles, F., Gràcia, F., Gil, E., Val, L., Planas, S., & Palacín, J. (2009). Obtaining the three-dimensional structure of tree orchards from remote 2D terrestrial LIDAR scanning. *Agricultural and Forest Meteorology*, 149, 1505-1515. <https://doi.org/10.1016/j.agrformet.2009.04.008>
- [50] Pfeifer, N., Gorte, B., & Winterhalder, D. (2004). Automatic reconstruction of single trees from terrestrial laser scanner data. *20th ISPRS Congress. Proceedings of Geo - Imagery Bridging Continents*, 1682-1750.
- [51] Rosell, J. R., Sanz, R., Llorens, J., Arnó, J., Escolà, A., Ribes-Dasi, M., Masip, J., Camp, F., Gràcia, F., Solanelles, F., Pallejà, T., Val, L., Planas, S., Gil, E., & Palacín, J. (2009). A tractor-mounted scanning LIDAR for the non-destructive measurement of vegetative volume and surface area of tree-row plantations: A comparison with conventional destructive measurements. *Biosystems Engineering*, 102(2), 128-134. <https://doi.org/10.1016/j.biosystemseng.2008.10.009>
- [52] Llorens, J. & Landers A. J. (2014). Variable rate spraying: digital canopy measurement for air and liquid electronic control. *International advances in pesticide application. Aspects of Applied Biology*, 114, 1-8.
- [53] Gregorio, E., Torrent, X., Planes de Marti, S., Solanelles, F., Sanz, R., Rocadenbosch, F., Masip, J., Ribes-Dasi, M., &

Rosell-Polo, J. (2016). Measurement of spray drift with a specifically designed lidar system. *Sensors*, 16(4), 499.
<https://doi.org/10.3390/s16040499>

- [54] Xiongkui, H., Aijun, Z., Yajia, L., & Jianli, S. (2011). Precision orchard sprayer based on automatically infrared target detecting and electrostatic spraying techniques. *International Journal of Agricultural and Biological Engineering*, 4, 35-40.

Authors' contacts:

Davor PETROVIĆ, MSc, Assistant
Faculty of Agriculture
Vladimira Preloga 1, 31000 Osijek, Croatia
pdavor@pfos.hr

Mladen JURISIĆ, PhD, Full Professor
Faculty of Agriculture
Vladimira Preloga 1, 31000 Osijek, Croatia
mjurisic@pfos.hr

Vjekoslav TADIĆ, PhD, Assistant Professor
(corresponding author)
Faculty of Agriculture
Vladimira Preloga 1, 31000 Osijek, Croatia
vtadic@pfos.hr

Ivan PLAŠČAK, PhD, Assistant Professor
Faculty of Agriculture
Vladimira Preloga 1, 31000 Osijek, Croatia
iplascak@pfos.hr

Željko BARAČ, MSc, Assistant
Faculty of Agriculture
Vladimira Preloga 1, 31000 Osijek, Croatia
zbarac@pfos.hr

14pt
14pt
ARTICLE TITLE ONLY IN ENGLISH (Style: Arial Narrow, Bold, 14pt)

14pt
Ivan HORVAT, Thomas JOHNSON (Style: Arial Narrow, Bold, 11pt)

14pt
Abstract: Article abstract contains maximum of 150 words and is written in the language of the article. The abstract should reflect the content of the article as precisely as possible. TECHNICAL JOURNAL is a trade journal that publishes scientific and professional papers from the domain(s) of mechanical engineering, electrical engineering, civil engineering, multimedia, logistics, etc., and their boundary areas. This document must be used as the template for writing articles so that all the articles have the same layout. (Style: Arial Narrow, 8pt)

8pt
Keywords: keywords in alphabetical order (5-6 key words). Keywords are generally taken from the article title and/or from the abstract. (Style: Arial Narrow, 8pt)

10pt

10pt

1 ARTICLE DESIGN

(Style: Arial Narrow, Bold, 10pt)

10pt

(Tab 6 mm) The article is written in Latin script and Greek symbols can be used for labelling. The length of the article is limited to eight pages of international paper size of Letter (in accordance with the template with all the tables and figures included). When formatting the text the syllabification option is not to be used.

10pt

1.1 General guidelines

(Style: Arial Narrow, 10pt, Bold, Align Left)

10pt

The document format is Letter with margins in accordance with the template. A two column layout is used with the column spacing of 10 mm. The running text is written in Times New Roman with single line spacing, font size 10 pt, alignment justified.

Article title must clearly reflect the issues covered by the article (it should not contain more than 15 words).

Body of the text is divided into chapters and the chapters are divided into subchapters, if needed. Chapters are numbered with Arabic numerals (followed by a period). Subchapters, as a part of a chapter, are marked with two Arabic numerals i.e. 1.1, 1.2, 1.3, etc. Subchapters can be divided into even smaller units that are marked with three Arabic numerals i.e. 1.1.1, 1.1.2, etc. Further divisions are not to be made.

Titles of chapters are written in capital letters (uppercase) and are aligned in the centre. The titles of subchapters (and smaller units) are written in small letters (lowercase) and are aligned left. If the text in the title of the subchapter is longer than one line, no hanging indents.

10pt

Typographical symbols (bullets), which are being used for marking an item in a list or for enumeration, are placed at a beginning of a line. There is a spacing of 10pt following the last item:

- Item 1
- Item 2
- Item 3

10pt

The same rule is valid when items are numbered in a list:

1. Item 1
2. Item 2
3. Item 3

10pt

1.2 Formatting of pictures, tables and equations

(Style: Arial Narrow, 10pt, Bold, Align Left)

10pt

Figures (drawings, diagrams, photographs) that are part of the content are embedded into the article and aligned in the centre. In order for the figure to always be in the same position in relation to the text, the following settings should be defined when importing it: text wrapping / in line with text.

Pictures must be formatted for graphic reproduction with minimal resolution of 300 dpi. Pictures downloaded from the internet in ratio 1:1 are not suitable for print reproduction because of unsatisfying quality.

10pt

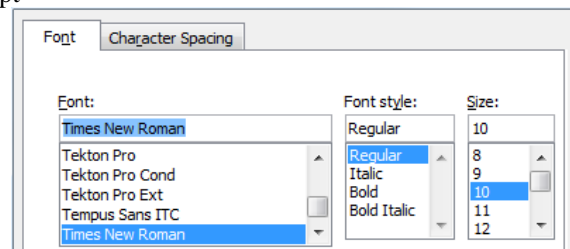


Figure 1 Text under the figure [1]
(Style: Arial Narrow, 8pt, Align Centre)

10pt

The journal is printed in black ink and the figures have to be prepared accordingly so that bright tones are printed in a satisfactory manner and are readable. Figures are to be in colour for the purpose of digital format publishing. Figures in the article are numbered with Arabic numerals (followed by a period).

Text and other data in tables are formatted - Times New Roman, 8pt, Normal, Align Center.

When describing figures and tables, physical units and their factors are written in italics with Latin or Greek letters,

while the measuring values and numbers are written upright.

10pt

Table 1 Table title aligned centre
(Style: Arial Narrow, 8pt, Align Centre)

	1	2	3	4	5	6
ABC	ab	ab	ab	ab	ab	ab
DEF	cd	cd	cd	cd	cd	cd
GHI	ef	ef	ef	ef	ef	ef

10 pt

Equations in the text are numbered with Arabic numerals inside the round brackets on the right side of the text. Inside the text they are referred to with equation number inside the round brackets i.e. “... from Eq. (5) follows ...” (Create equations with MathType Equation Editor - some examples are given below).

10pt

$$F_{\text{avg}}(t, t_0) = \frac{1}{t} \int_{t_0}^{t_0+t} F(q(\tau), p(\tau)) d\tau, \quad (1)$$

10pt

$$\cos \alpha + \cos \beta = 2 \cos \frac{\alpha + \beta}{2} \cdot \cos \frac{\alpha - \beta}{2}. \quad (2)$$

10pt

Variables that are used in equations and also in the text or tables of the article are formatted as *italics* in the same font size as the text.

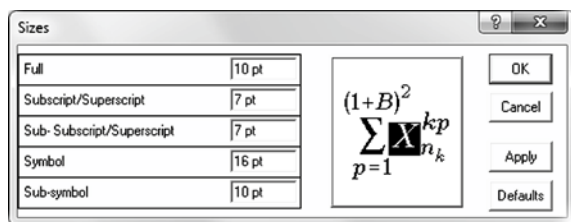


Figure 2 The texts under figures
(Style: Arial Narrow, 8pt, Align Centre)

Figures and tables that are a part of the article have to be mentioned inside the text and thus connected to the content i.e. „... as shown in Fig. 1...” or „data from Tab. 1...” and similar.

10pt

2 PRELIMINARY ANNOTATION

10pt

Article that is offered for publication cannot be published beforehand, be it in the same or similar form, and it cannot be offered at the same time to a different journal. Author or authors are solely responsible for the content of the article and the authenticity of information and statements written in the article.

Articles that are accepted for publishing are classified into four categories: original scientific papers, preliminary communications, subject reviews and professional papers.

Original scientific papers are articles that according to the reviewer and the editorial board contain original theoretical or practical results of research. These articles need to be written in such a way that based on the information given, the experiment can be repeated and the

results described can be achieved together with the author's observations, theoretical statements or measurements.

Preliminary communication contains one or more pieces of new scientific information, but without details that allow recollection as in original scientific papers. Preliminary communication can give results of an experimental research, results of a shorter research or research in progress that is deemed useful for publishing.

Subject review contains a complete depiction of conditions and tendencies of a specific domain of theory, technology or application. Articles in this category have an overview character with a critical review and evaluation. Cited literature must be complete enough to allow a good insight and comprehension of the depicted domain.

Professional paper can contain a description of an original solution to a device, assembly or instrument, depiction of important practical solutions, and similar. The article need not be related to the original research, but it should contain a contribution to an application of known scientific results and their adaptation to practical needs, so it presents a contribution to spreading knowledge, etc.

Outside the mentioned categorization, the Editorial board of the journal will publish articles of interesting content in a special column. These articles provide descriptions of practical implementation and solutions from the area of production, experiences from device application, and similar.

10pt

3 WRITING AN ARTICLE

10pt

Article is written in the English language and the terminology and the measurement system should be adjusted to legal regulations, standards (ISO 80 000 series) and the SI international system of units. The article should be written in third person.

Introduction contains the depiction of the problem and an account of important results that come from the articles that are listed in the cited literature.

Main section of the article can be divided into several parts or chapters. Mathematical statements that obstruct the reading of the article should be avoided. Mathematical statements that cannot be avoided can be written as one or more addendums, when needed. It is recommended to use an example when an experiment procedure, the use of the work in a concrete situation or an algorithm of the suggested method must be illustrated. In general, an analysis should be experimentally confirmed.

Conclusion is a part of the article where the results are being given and efficiency of the procedure used is emphasized. Possible procedure and domain constraints where the obtained results can be applied should be emphasized.

10pt

4 RECAPITULATION ANNOTATION

10pt

In order for the articles to be formatted in the same manner as in this template, this document is recommended for use when writing the article. Finished articles written in MS Word for Windows and formatted according to this

template must be submitted using our The Paper Submission Tool (PST) (<https://tehnickiglasnik.unin.hr/authors.php>) or eventually sent to the Editorial board of the Technical Journal to the following e-mail address: tehnickiglasnik@unin.hr

The editorial board reserves the right to minor redaction corrections of the article within the framework of prepress procedures. Articles that in any way do not follow these authors' instructions will be returned to the author by the editorial board. Should any questions arise, the editorial board contacts only the first author and accepts only the reflections given by the first author.

10pt

5 REFERENCES (According to APA)

10pt

The literature is cited in the order it is used in the article. Individual references from the listed literature inside the text are addressed with the corresponding number inside square brackets i.e. "... in [7] is shown ...". If the literature references are web links, the hyperlink is to be removed as shown with the reference number 8. Also, the hyperlinks from the e-mail addresses of the authors are to be removed. In the literature list, each unit is marked with a number and listed according to the following examples (omit the subtitles over the references – they are here only to show possible types of references):

9pt

- [1] See <http://www.bibme.org/citation-guide/apa/>
- [2] See http://sites.umuc.edu/library/libhow/apa_examples.cfm
- [3] (Style: Times New Roman, 9pt, according to APA)
- [4] Amidzic, O., Riehle, H. J., & Elbert, T. (2006). Toward a psychophysiology of expertise: Focal magnetic gamma bursts as a signature of memory chunks and the aptitude of chess players. *Journal of Psychophysiology*, 20(4), 253-258. <https://doi.org/10.1027/0269-8803.20.4.253>
- [5] Reitzes, D. C., & Mutran, E. J. (2004). The transition to retirement: Stages and factors that influence retirement adjustment. *International Journal of Aging and Human Development*, 59(1), 63-84. Retrieved from <http://www.baywood.com/journals/PreviewJournals.asp?Id=0091-4150>
- [6] Jans, N. (1993). *The last light breaking: Life among Alaska's Inupiat Eskimos*. Anchorage, AK: Alaska Northwest Books.
- [7] Miller, J., & Smith, T. (Eds.). (1996). *Cape Cod stories: Tales from Cape Cod, Nantucket, and Martha's Vineyard*. San Francisco, CA: Chronicle Books.
- [8] Chaffe-Stengel, P., & Stengel, D. (2012). *Working with sample data: Exploration and inference*. <https://doi.org/10.4128/9781606492147>
- [9] Freitas, N. (2015, January 6). People around the world are voluntarily submitting to China's Great Firewall. Why? Retrieved from http://www.slate.com/blogs/future_tense/2015/01/06/tencent_s_wechat_worldwide_internet_users_are_voluntarily_submitting_to.html

10pt

10pt

Authors' contacts:

8pt

Full Name, title
Institution, company
Address
Tel./Fax, e-mail

8pt

Full Name, title
Institution, company
Address
Tel./Fax, e-mail

TEHNIČKI GLASNIK / TECHNICAL JOURNAL – GODIŠTE / VOLUME 12 – BROJ / NUMBER 3

RUJAN 2018 / SEPTEMBER 2018 – STRANICA / PAGES 124-195



**Sveučilište
Sjever**

SVEUČILIŠTE SJEVER / UNIVERSITY NORTH – CROATIA – EUROPE

ISSN 1846-6168 (PRINT) / ISSN 1848-5588 (ONLINE)

TEHNICKIGLASNIK@UNIN.HR – [HTTP://TEHNICKIGLASNIK.UNIN.HR](http://tehnickiglasnik.unin.hr)